UNIVERSIDAD TÉCNICA FEDERICO SANTA MARÍA DEPARTAMENTO DE INGENIERÍA QUÍMICA Y AMBIENTALVALPARAISO-CHILE

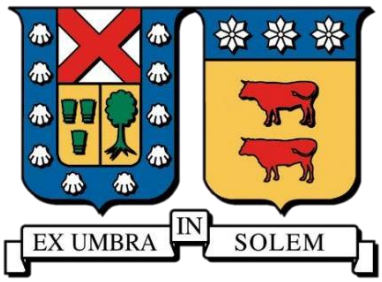

"MEASUREMENT AND MODELING OF SOLID BIOCHANIN A SOLUBILITY IN PURE AND ETHANOL-MODIFIED SUPERCRITICAL CO_2"

EDUARDA ANDREA VILLAR WOLF

Thesis to qualify for the degree of

MASTER IN CHEMICAL ENGINEERING SCIENCES

Tutor Professor	Juan C. de la Fuente, PhD
Co-referent professor (internal):	Gonzalo Nuñez, PhD
Co-referent professor (internal):	Adolfo Cabrera, MSc.
Co-referent professor (external)	Roberto Canales, PhD (PUC)

July, 2026

CONSTANCIA DE VALIDACIÓN Y CONFIDENCIALIDAD DE MONOGRAFÍA A REPOSITORIO ACADÉMICO

1.- IDENTIFICACIÓN DEL TRABAJO ACADÉMICO

Tipo de monografía (marcar una opción): ☐ Memoria o trabajo de título ☒ Tesis de Postgrado

Título del trabajo: "Measurement and Modeling of Solid Biochanin A Solubility in pure and ethanol-modified supercritical CO_2"

Nombre del candidato(a): Eduarda Andrea Villar Wolf

Carrera / Grado: Magister en Ciencias de la Ingeniería Química

Campus: Casa Central **Departamento:** Departamento de Ingeniería Química y Ambiental

2.- VALIDACIÓN DEL PROFESOR GUÍA/DIRECTOR DE TESIS

Yo, Juan C. de la Fuente, en mi calidad de profesor(a) guía/director(a) del trabajo académico mencionado anteriormente **DEJO CONSTANCIA** que:

- He revisado esta versión del documento y corresponde a la versión final aprobada del trabajo.
- El trabajo cumple con los requisitos académicos y de formato establecidos por la institución.

3.- EVALUACIÓN DE CONFIDENCIALIDAD POR PROPIEDAD INDUSTRIAL (marcar una opción)

☒ El trabajo **NO contiene** información que amerite confidencialidad y puede ser publicado de inmediato en repositorio con acceso abierto.

☐ El trabajo **CONTIENE** información con potenciales implicancias de propiedad industrial o intelectual y requiere un periodo de confidencialidad (**embargo**) por **(marcar una opción)**:

☐ 6 meses ☐ 12 meses ☐ 2 años ☐ 3 años ☐ 5 años ☐ 10 años

Fundamentación de la necesidad de confidencialidad (obligatorio si se solicita embargo):

4.- FIRMAS

Profesor(a) guía o director(a) de memoria o tesis:

Fecha: 23 de Julio de 2026 **Firma:** Juan C. de la Fuente

Estudiante o Candidato(a):

Fecha: 23 de Julio de 2026 **Firma:** Eduarda Villar

Este formulario debe ser insertado como página 2 de la memoria o tesis, completado y firmado por estudiante y profesor(a) antes de la entrega en portal PRISMA de Biblioteca USM.

Acknowledgements

I would like to express my sincere gratitude to Dr. Juan C. de la Fuente and Professor Adolfo Cabrera for their guidance throughout this journey. Their support and the knowledge they shared with me were essential to the development of this work. The perspective, expertise, and wisdom they provided made a significant difference in the outcome of this thesis.

I would especially like to thank Professor Juan for believing in me. I cannot imagine what my university experience would have been like without the opportunity to serve as his teaching assistant for Process Thermodynamics. Thank you for your encouragement during moments of uncertainty and for your support whenever doubts arose.

I am also grateful to Professor Juan Yianatos for giving me the opportunity to work as a teaching assistant in the Process Laboratory course, where I not only deepened my theoretical knowledge but also learned to trust myself more. My thanks also go to my fellow Process Laboratory teaching assistants for making our days working in laboratory more enjoyable. Finally, I would like to thank the *Materia* team for creating such a welcoming and inspiring work environment, where I was able not only to learn, but also to share memorable moments and many laughs.

A special thank you goes to Juanín and Mayra, who stood by me throughout this past year of work and uncertainty. Their companionship helped me navigate this process and find moments of relief amidst the challenges. I would also like to thank Pedro, who has been by my side since the very beginning. Pedro, thank you for helping me keep things in perspective, and for all the advice and laughter we shared along the way.

Finally, my deepest and most heartfelt gratitude goes to my mother, Ximena Wolf Valdés. Even when we were far apart, I never stopped feeling her presence and support throughout this journey. Thank you for always listening to me, for offering your wisdom and love, and for being there during every moment of uncertainty. Thank you for believing in me, for supporting me unconditionally, and for understanding me every step of the way. I love you, Mom, and I will always be grateful for everything you have given me.

Abstract in Spanish

La extracción de compuestos bioactivos de alto valor, como la biochanina A, requiere métodos sostenibles y eficientes, entre los que destaca la extracción con fluidos supercríticos (SCFE) utilizando dióxido de carbono (CO_2). Sin embargo, el diseño de estos procesos demanda datos confiables de equilibrio de fases, los cuales actualmente no están disponibles para el sistema biochanina A + CO_2 supercrítico. Esta tesis tiene como objetivo medir experimentalmente, validar y modelar termodinámicamente el equilibrio sólido-fluido de la biochanina A en CO_2 supercrítico a temperaturas cercanas a la ambiente.

Las mediciones de solubilidad se realizaron mediante un método isotérmico dinámico-analítico con una celda de visualización de alta presión y cuantificación por cromatografía líquida de alta resolución (HPLC). Los datos se obtuvieron en tres isotermas (313,15; 323,15 y 333,15 K) y en un rango de presión de aproximadamente 10 a 32 MPa. La confiabilidad de las mediciones se evaluó mediante estimaciones de incertidumbre expandida combinada, el modelo de autoconsistencia de Méndez-Santiago y Teja (MS-T) y la prueba de consistencia termodinámica de Valderrama y Zavaleta.

Las fracciones molares experimentales de biochanina A variaron entre $0{,}43 \cdot 10^{-6}$ y $7{,}89 \cdot 10^{-6}$ mol·mol^{-1}. Las isotermas revelaron un comportamiento anómalo, caracterizado por un máximo de solubilidad entre 14,0 y 16,0 MPa, seguido de una disminución abrupta. El análisis por resonancia magnética nuclear confirmó la ausencia de degradación estructural, indicando que este fenómeno se debe a la autoasociación del soluto. A altas presiones, la reducción del volumen libre favorece la formación de dímeros mediante enlaces de hidrógeno, lo que disminuye la volatilidad de la biochanina A y reduce su presencia en la fase supercrítica.

La ecuación de estado SAFT-VR Mie se empleó para correlacionar el equilibrio de fases. Aunque el modelo monomérico reprodujo adecuadamente datos de equilibrio sólido-líquido (AARD = 4,53 %), no logró describir el comportamiento en CO_2 supercrítico (AARD = 160,37 %), evidenciando la necesidad de considerar explícitamente el equilibrio monómero-dímero. Finalmente, el modelado termodinámico mostró que la adición de etanol como cosolvente incrementa significativamente la solubilidad al reducir la autoasociación.

Este trabajo proporciona nuevos datos de solubilidad a alta presión para la biochanina A en CO_2 supercrítico y establece una base para el diseño futuro de procesos de extracción con fluidos supercríticos.

Abstract

The extraction of high-value bioactive compounds like biochanin A demands green, efficient methods such as Supercritical Fluid Extraction (SCFE) using carbon dioxide (CO_2). Designing these processes requires reliable phase equilibrium data, which is currently unavailable for the biochanin A + SC-CO_2 system. This thesis aims to experimentally measure, validate, and thermodynamically model the solid-fluid phase equilibrium of biochanin A in supercritical CO_2 at near-ambient temperatures.

Solubility measurements were performed using a dynamic-analytical isothermal method with a high-pressure view-cell and HPLC quantification. Data were collected along three isotherms (313.15, 323.15, and 333.15 K) in a pressure range of roughly 10 to 32 MPa. The reliability of these measurements was verified through combined expanded uncertainty estimations, the Méndez-Santiago and Teja (MS-T) self-consistency model, and the Valderrama and Zavaleta thermodynamic consistency test.

Experimental molar fractions of Biochanin A ranged from $0.43 \cdot 10^{-6}$ to $7.89 \cdot 10^{-6}$ mol·mol^{-1}. Notably, the isotherms revealed anomalous phase behavior: instead of increasing monotonically with pressure, solubility reached a distinct maximum between 14.0 and 16.0 MPa, followed by a sharp decline. NMR analysis confirmed that no structural degradation occurred, indicating this phenomenon is exclusively driven by solute self-association. At higher pressures, reduced free volume promotes hydrogen bonding at the C7 hydroxyl group, forming dimers with doubled molecular mass and reduced volatility, shifting them out of the supercritical phase.

The SAFT-VR Mie Equation of State was applied to correlate the phase equilibrium. While molecular parameters for the pure monomer were successfully fitted using solid-liquid equilibrium data in ethanol and 2-propanol (yielding an AARD of 4.53%), applying this purely monomeric model to the SC-CO_2 system resulted in an AARD of 160.37%. The model erroneously predicted a continuous solubility increase, proving that explicitly accounting for the monomer-dimer equilibrium is necessary to capture the real phase behavior. Finally, thermodynamic modeling demonstrated that adding a polar cosolvent like ethanol significantly enhances Biochanin A solubility across all conditions by disrupting self-association.

This work provides high-pressure solubility data for Biochanin A in SC-CO_2, demonstrating the critical impact of solute dimerization on phase equilibria and offering a fundamental basis for future SCFE process design.

Table of Contents

List of Figures

List of Tables

Introduction

The growing concern for food safety and pharmaceutical quality has driven an increasing demand for production processes that are safe, energy-efficient, and environmentally sustainable [1], [2]. Motivated by these facts, this thesis aims to provide relevant data for the design of processes that enable the recovery of biologically significant substances using an unconventional solvent and an environmentally friendly method.

Bioactive compounds are both essential and non-essential compounds found in nature [3], which can also be demonstrated to have potential health benefits for humans. Their study has led to the identification of new compounds and the development of applications in cosmetics, food, and healthcare [4]. Today, natural ingredients such as aloe vera derivatives and olive oil are preferred in cosmetics due to their sustainability [5]. They are also used as colorants and additives to improve food quality [6].

Around 50% of anti-infective and anticancer drugs are derived from bioactive compounds [7]. Research on these compounds remains crucial for treating diseases such as cancer, infections, diabetes, and cardiovascular conditions, which still lack effective and accessible treatments. Oxidative stress has been linked to cardiovascular and neurodegenerative diseases, driving the study of antioxidant bioactive compounds [8]. Bioactive compounds have gained interest in chemotherapy due to their low toxicity in healthy cells [9].

4′-methoxy-5,7-dihydroxy isoflavone, or biochanin A, is a bioactive compound (isoflavone) with pharmaceutical properties of interest, including anticancer, anti-inflammatory, hepatoprotective, antioxidant, neuroprotective, and antidiabetic activities [10]. The anticancer effect of biochanin A extends to various types of cancer, such as bladder, breast, pancreatic, prostate, osteosarcoma, and liver cancer [10]. This isoflavonoid is isolated from numerous plants, with red clover (Trifolium pretense L.), peanuts, and chickpeas standing out [11], all of which are widely consumed foods, making it accessible and cost-effective.

The extraction of bioactive compounds from plant material can be conducted using a variety of extraction techniques. These techniques are classified into traditional and modern methods. Traditional methods include Soxhlet extraction, maceration, percolation, turbo-extraction, and sonication [12]. However, these approaches are often slow and require large volumes of organic solvents, such as n-hexane and chloroform, which pose health risks. Additionally, methods such as distillation involve high thermal loads that can degrade thermolabile compounds present in plant material, limiting their applicability in the extraction of isoflavonoids like biochanin A.

This work proposes the use of an unconventional solvent for the extraction of biochanin A, specifically carbon dioxide (CO_2) under supercritical conditions (SC), meaning at a temperature (T) and pressure (p) above the critical values of the substance (for CO_2: T_c = 304.1 K, p_c = 7.38 MPa). Carbon dioxide under supercritical conditions (SC-CO_2) can dissolve phytochemical compounds from plant substrates without leaving contaminant residues in the final product through a process known as supercritical fluid extraction (SCFE). This method enables the recovery of highly pure bioactive compounds and prevents unwanted chemical reactions. Although the initial investment in SCFE equipment is higher than that required for atmospheric pressure extraction techniques, the process itself is relatively simple and easily scalable to an industrial level [13].

For the economic feasibility study and scale-up of processes using SC-CO_2, it is necessary to have information on phase equilibrium, that is, the thermodynamic solubility (y_i) of solute i in the CO_2-rich phase of the system at temperature T and pressure p. Additionally, for the design, simulation, and optimization of extraction processes, a thermodynamic model is required to represent solubility as a function of temperature, pressure, and other parameters fitted from experimentally validated data from binary systems. Along with thermodynamic information, kinetic studies are also necessary, but they will not be covered in this work. It is important to note that there is no solubility information available for the studied system in this work.

The objective of this thesis is to contribute validated experimental data and models to represent the thermodynamic solubility (mole fraction) of the system biochanin A + CO_2 at temperatures close to atmospheric. The specific objectives are: (1) to verify the functionality and incorporate improvements (if necessary) to the experimental equipment for measuring fluid (F) + solid (S) phase equilibria (FSE) available in the Process Thermodynamics Laboratory (LTP) at the Department of Chemical and Environmental Engineering (DIQA) at the Universidad Técnica Federico Santa María (UTFSM); (2) to provide experimental solubility data for the biochanin A + CO_2 system concerning pressure (p < 32 MPa) and operating temperature (313 K, 323 K, and 333 K); (3) to establish the validity of the experimental data from objective (2) using a procedure that considers: (3.1) uncertainty estimation, (3.2) thermodynamic consistency evaluation, and (3.3) self-consistency evaluation; and (4) to apply an advanced thermodynamic model (specifically, the SAFT-VR Mie equation of state) to correlate solute solubility in SC-CO_2 at high pressure, and fit the required model parameters to the validated experimental data from objective (3).

1. Studied Solute: Biochanin A

This section provides information on isoflavones, and biochanin A. Section 1.1 presents the structure, classification, and general biological functions of polyphenols, with a special focus on isoflavones, particularly biochanin A.

Section 1.2 introduces some of the most important biological activities and the recommended dietary intake of isoflavones to understand their relevance to human health. Finally, Section 1.3 presents different methods for obtaining isoflavones from natural sources to understand the advantages of extraction processes for isolating these substances.

1.1. Structure and Biological Functions

Biochanin A is a type of polyphenol. Polyphenols are phenolic compounds of plant origin. These compounds are produced as a result of the secondary metabolism of plants [14] and are mostly found conjugated with sugars (glycosides) [15]. In some cases, they can also be found as aglycones. Due to this structure, polyphenols tend to be water-soluble.

Polyphenols are mainly synthesized through two metabolic pathways: the shikimic acid pathway and the acetate pathway [16]. More than 8,000 polyphenolic structures are currently known [17], with their common characteristic being an aromatic ring with at least one hydroxyl substituent [18]. Polyphenols can be classified into different classes according to their chemical structure.

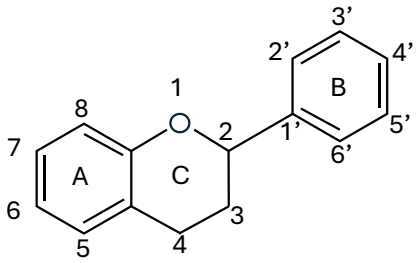

Figure 1.1. Basic structure of flavonoids.

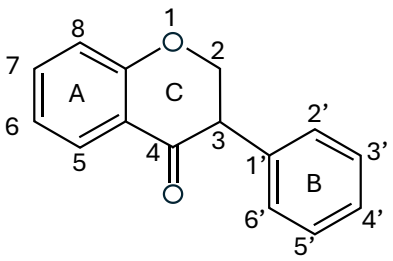

Figure 1.2. Basic structure of an isoflavone.

Flavonoids are the most extensive class of polyphenols. Their basic structure (Figure 1.1) consists of two aromatic rings linked by three carbon atoms. Flavonoids are further subdivided based on the position of the carbon in ring C to which ring B is attached, as well as the degree of unsaturation and oxidation of ring C. Their subclasses include flavonols, flavones, flavanones, flavanols, anthocyanins and isoflavones.

Isoflavonoids are compounds that differ from other flavonoids by the position of ring B at position 3 of ring C, instead of position 2 [14]. This structural modification influences their biological properties and chemical behavior. In plants, isoflavonoids function as antioxidants to neutralize reactive oxygen species under abiotic stress conditions. Additionally, they participate in pathogen defense as phytoalexins, inhibiting microbial growth [19]. They also influence cell signaling, regulating essential metabolic pathways for plant development. Isoflavonoids are known for their phytoestrogenic activity, as they can interact with estrogen receptors in mammals, giving them a relevant role in human health [10].

"Isoflavone" is a general term for isoflavonoids that have a carbonyl group at position C4 of their basic benzopyran skeleton (15 carbons, C6-C3-C6), with ring B attached at position C3 (Figure 1.2). These are present in various plant species, especially legumes, and have antioxidant [20], [21], anti-inflammatory [20], [22], [23], and potentially anticancer properties [24], [25].

Isoflavones are predominantly found in legumes and are one of the main bioactive components present in species such as red clover, soybeans, and chickpeas [26] (Figure 1.3 shows some isoflavones present in legumes). Global legume production continues to grow, with soybeans, chickpeas, and red clovers being prominent crops. For example, global soybean production is estimated to reach 418 million tons in the 2024/25 season, 5% more than the previous season, with Brazil being one of the main producers [27].

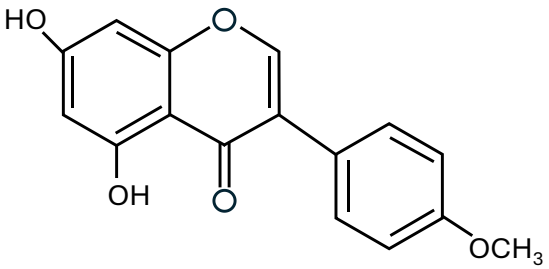

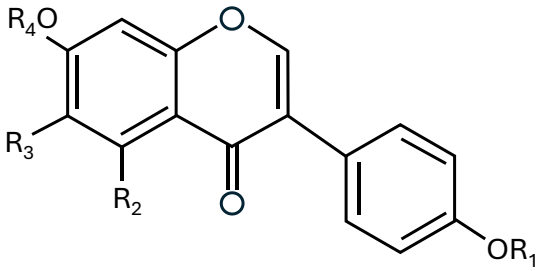

Compound	R_1	R_2	R_3	R_4
Daidzein	H	H	H	H
Genistein	H	OH	H	H
Biochanin A	CH_3	OH	H	H
Irilone	H	OH	-	OCH_2-
Prunetin	H	OH	H	CH_3
Ononin	CH_3	H	H	glc

Figure 1.3. Biochanin A (left) and other isoflavones from legumes.

The fate of these legumes varies depending on the crop. Approximately 85% of soybeans are processed into meal and oil, a process that generates a large amount of husk as a byproduct. This byproduct accounts for up to 8% of grain yield, equivalent to approximately 34 million tons of husks during the 2024/25 season.

Biochanin A, chemically known as 5,7-Dihydroxy-4′-methoxyisoflavone [CAS: 491-80-5] is a naturally occurring isoflavone predominantly found in red clover (*Trifolium pratense*), chickpeas (*Cicer arietinum*), soybeans (*Glycine max*), and other legumes [28]. Biochanin A has shown many potential health-promoting benefits, considering the cumulative evidence that indicates its biological activity, which gives biochanin A pharmacological properties, including anti-inflammatory [29], antioxidant [30], anticancer [31] and neuroprotective[32].

From a physicochemical perspective, the molecular structure of biochanin A features two hydroxyl (-OH) groups — at positions 5 and 7 — that play a critical role in its thermodynamic behavior. The unhindered hydroxyl at position 7 is particularly susceptible to intermolecular hydrogen bonding, raising the possibility of solute self-association under high-pressure conditions. As will be discussed in detail in Section 5, this structural predisposition has significant implications for the solid-fluid phase equilibrium behavior observed in the present work, and constitutes a central element of the thermodynamic interpretation developed herein.

1.2. Biological Activities and Dietary Intake

Biochanin A is an O-methylated isoflavone with a broad range of pharmacological properties, including anti-inflammatory, antioxidant, neuroprotective, and anticancer activities. Its anti-inflammatory effects have been linked to the inhibition of key pro-inflammatory mediators, reducing oxidative stress and inflammatory responses in various disease models [33]. Notably, biochanin A has demonstrated neuroprotective potential in neurodegenerative conditions such as Alzheimer's disease, Parkinson's disease, and cerebral ischemia. In Alzheimer's disease models, it improved memory and learning deficits, while in Parkinson Disease models, it prevented microglial activation and neuronal loss, mitigating behavioral abnormalities [34]. Moreover, biochanin A exerts anticancer effects, with evidence suggesting that its chemo preventive properties may be mediated through modulation of carcinogen metabolism. Additionally, biochanin A has been shown to induce the expression of drug-metabolizing enzymes and efflux transporters, suggesting a potential role in drug interactions [35]. Given its wide-ranging biological activities, biochanin A holds promise as a therapeutic agent for inflammation, neurodegenerative diseases, cancer, and metabolic dysfunctions.

Due to the complexity of polyphenols, information on the content and composition of polyphenols in foods is often incomplete [36]. Thus, making the daily intake of isoflavonoids difficult to estimate and confounds the ability to infer epidemiologic relationships regarding health and disease. Nevertheless, it is estimated that in western populations the daily dietary intake of isoflavonoids is almost negligible (<1 mg/d) [37]. Table 1.1 provides an estimation of the daily dietary flavonoid intake per polyphenol.

Table 1.1. Estimated daily dietary total and individual flavonoid intakes of U.S. adults aged 19+ [38].

Polyphenol	Daily Intake, mg/d
Flavonols	12,9 ± 0,4
Flavones	1,6 ± 0,2
Flavanones	14,4 ± 0,6
Flavan-3-ols	156,5 ± 11,3
Anthocyanidins	3,1 ± 0,5
Isoflavones	1,2 ± 0,2

1.3. Sources of Biochanin A and other isoflavonoids

The main sources of biochanin A and flavonoids such as genistein, daidzein, and quercetin are primarily plants, especially legumes and certain fruits and vegetables. Biochanin A can be isolated from red clover [39], soybeans and chickpeas [40].

A key consideration prior to selecting any extraction method is the chemical form in which isoflavones occur in plant matrices. They are predominantly found as glycoside conjugates (e.g., genistin, daidzin, ononin) rather than as free aglycones, and because these conjugates are chemically labile, the extraction method must be carefully chosen to preserve their integrity [41]. This is particularly relevant for biochanin A, which exhibits poor thermal stability; extraction temperatures should not exceed 60°C to avoid significant losses, and temperatures above 125°C cause sharp degradation of most glycoside forms [42]. These constraints directly condition the choice of extraction technique.

To extract these flavonoids, conventional solvent-based techniques are often employed due to their operational simplicity and capacity to achieve high yields. However, they need large volumes of potentially toxic organic solvents, extended processing times, and present risks of thermal degradation and residual solvent retention in the final extract [41]. Modern alternatives have been developed to address these shortcomings. Ultrasound-Assisted Extraction (UAE) uses acoustic cavitation to disrupt plant cell walls and enhance mass transfer at low temperatures with reduced solvent consumption — a critical advantage given biochanin A's

thermal sensitivity [42]. Microwave-Assisted Extraction (MAE) irradiates plant material to release intracellular compounds with minimal solvent use and has demonstrated significantly higher total phenolic yields compared to conventional maceration under optimized conditions [43]. Pressurized Liquid Extraction (PLE) applies elevated temperature and pressure to maintain solvents in the liquid state, enhancing solubility and diffusion rates, and has been shown to achieve the highest total isoflavone recoveries among multiple compared techniques [44].

An emerging class of green solvents, Deep Eutectic Solvents (DES) and their natural counterparts (NaDES), have attracted increasing attention due to their biodegradability, low toxicity, and ease of preparation [45]. Choline chloride-based DES systems have demonstrated superior extraction yields for biochanin A, formononetin, ononin, and sissotrin from chickpea sprouts compared to conventional organic solvents, particularly when coupled with UAE to exploit synergistic effects of solvent penetration and cavitation [46].

Supercritical CO_2 fluid extraction (SCFE-CO_2) utilizes GRAS (*Generally regarded as safe*) CO_2 above its critical point as a green solvent [47]. This approach yields highly pure, solvent-free flavonoid extracts at moderate temperatures, preserving bioactivity and complying with stringent pharmaceutical and food-safety regulations. Although SCFE-CO_2 demands higher capital outlay and meticulous optimization of process parameters to balance yield and selectivity, its ecological profile and absence of residual solvents make it the preferred method for high-value applications in both the pharmaceutical and alimentary industries [13]. The solvating power of supercritical CO_2 can be further enhanced by adding co-solvent modifiers such as methanol–water mixtures, broadening its applicability to more polar solutes [48].

It should be noted that, despite extensive optimization at laboratory scale, there is currently no established methodology for commercializing isoflavone extraction from plant feedstocks. Transitioning to industrial processes requires simultaneous evaluation of technical, economic, and environmental metrics across multiple candidate extraction technologies — a challenge that remains an active area of research [49].

2. Supercritical Fluid Extraction

One reason for measuring a solute's solubility in SC-CO_2 is to identify the best conditions for its extraction from a natural substrate via supercritical fluid extraction (SCFE). This section discusses the supercritical state, the supercritical fluid extraction (SCFE) process, and the advantages of using CO_2 over other solvents in SCFE.

2.1. Supercritical Fluid Solvents and Supercritical Fluid Extraction Processes

A pure substance is said to be in a supercritical state when both its pressure and temperature are above their critical values (for CO_2: $T_c = 304.1\ K, p_c = 7.38\ MPa$), as shown in Figure 2.1.

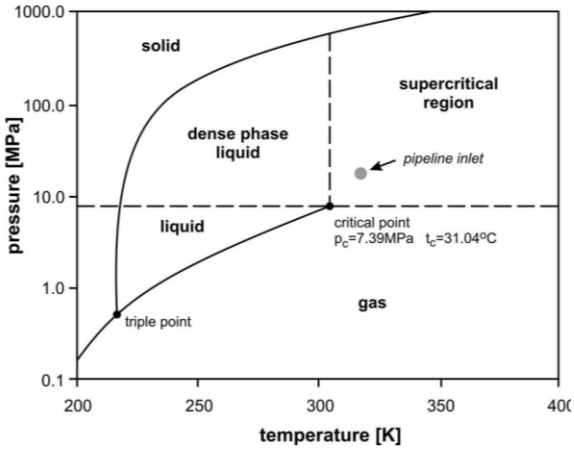

Figure 2.1. Phase diagram for CO_2 [50].

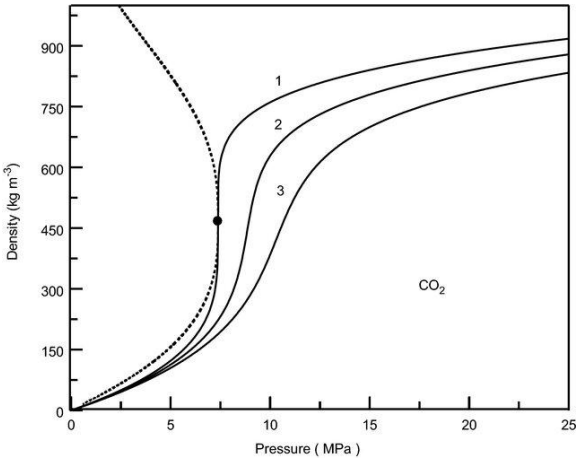

Figure 2.2. Density of carbon dioxide as a function of pressure along the selected near-critical and supercritical isotherms. 1 - T = 304.13 K; 2 - T = 313.15 K; 3 - T = 323.15 K [51].

As a substance approaches its critical point, the densities of the liquid and gas phases become equal, forming a single fluid. Around the critical isotherm, at pressures above the critical value, transport properties such as viscosity and diffusivity, as well as density, can be continuously adjusted from gas-like to liquid-like with relatively small changes in pressure [52]. Supercritical fluids offer two key advantages: their high density, similar to that of liquids, enhances solvency, while their high compressibility, akin to that of gases, allows small changes in temperature and pressure to significantly alter density. Since solubility depends on density, the solvency of a supercritical fluid is easily adjustable, as illustrated in Figure 2.2. Additionally, as shown in Table 2.1, supercritical fluids exhibit highly favorable transport properties that influence mass transfer and solubility.

Table 2.1. Comparison of density, viscosity and diffusivity for typical liquid, gas and SCF [53].

	Density (kg m^{-3})	Viscosity (cP)	Diffusivity (mm^2 s^{-1})
Gas	1	0.01	1 – 10
SCF	100 – 1000	0.05 – 0.1	0.01 – 0.1
Liquid	1000	0.5 – 1.0	0.001

The intermediate properties of supercritical fluids arise from local molecular clustering. Near the critical point, density fluctuations become significant, giving rise to transient, short-range ordered structures. These clusters reflect non-ideal behavior and indicate regions of enhanced local density. Their formation is driven by attractive intermolecular forces and is associated with a growing correlation length. These microstructures influence both thermodynamic and transport properties [54]. They help explain the coexistence of gas-like diffusivity and liquid-like solvating power in SCFs, which is essential for efficient solute solvation and mass transfer.

Supercritical fluid extraction (SCFE) is an efficient separation technique. It is used to obtain natural compounds in food, pharmaceuticals, cosmetics, and chemicals. Its main advantage is selectivity, allowing the extraction of substances that are difficult or expensive with traditional methods. Moreover, SCFE significantly reduces extraction time, minimizes the consumption of organic solvents, and is well-suited for thermo-sensitive compounds [55]. This technique also produces cleaner extracts and is considered environmentally friendly, further reinforcing its value as an alternative to traditional extraction methods [56]. SCFE operates in two stages: extraction and separation, achieved by adjusting the solvent's solvating power under different conditions. This process is usually done in batches; so, the raw material (usually ground) is fed into the extractor before the process begins.

Figure 2.3 illustrates a simplified SCFE process using supercritical carbon dioxide (SC-CO_2). Pressurized CO_2 at 200–400 bar and at a temperature of 40–60 °C [57] is introduced into the extractor, dissolving the target compounds present in the feedstock. The CO_2, laden with the extract, is transferred to a separator, where pressure and temperature changes reduce the solvent power, causing the solute to precipitate. The solute collects at the bottom of the separator. Alternatively, the solvent power can be adjusted by increasing the temperature or adding a third substance, depending on the feed characteristics and the process profitability. Finally, the gaseous CO_2, free from the extract, is recirculated back to the extractor.

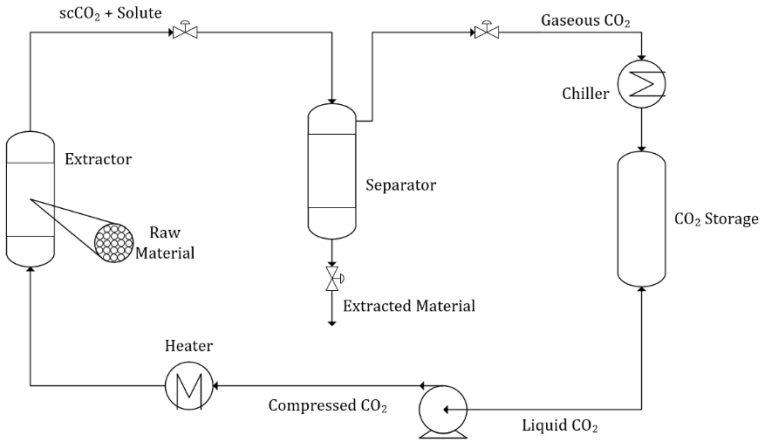

Figure 2.3. Simplified SCFE process.

2.2. Supercritical Fluid Extraction Processes with Carbon Dioxide

SCFE has been explored using various solvents, including propane, n-butane, methylpropane, freon (fluorocarbons), nitrous oxide, dimethyl ether, and even water. However, many of these solvents present significant drawbacks, such as toxicity, environmental concerns, or the need for stringent safety measures. For example, water's critical temperature is nearly 400 °C, making it impractical for most applications Table 2.2 shows the critical pressure and temperature of various solvents.

In contrast, CO_2 in its supercritical state (SC-CO_2) has become the most widely used SCF solvent due to its favorable properties. It is non-toxic, non-flammable, non-explosive [47]. Carbon dioxide is generally regarded as safe by the Food and Drug Administration (FDA) and the European Food Safety Authority (EFSA) [58]. Moreover, because CO_2 is gaseous at ambient conditions, solvent recovery is straightforward and does not require complex separation steps. Its relatively low critical temperature and pressure make it suitable for processing thermally sensitive compounds, while also improving energy efficiency compared to other supercritical fluids.

The selectivity of SC-CO_2 can be tuned by adjusting operating pressure and temperature, allowing for the targeted extraction to certain solutes [59]. Additional advantages—such as minimal waste generation, simple solvent recycling, and unique thermophysical and transport properties—have sparked growing interest in developing sustainable process alternatives based on SC-CO_2 [53].

Table 2.2. Apparent physical properties for various supercritical fluids used as solvents [60].

Solvent	MW / g·mol^{-1}	T_c / °C	p_c / MPa	ρ_c / kg·m^{-3}
Ammonia (NH_3)	17.03	132.2	11.33	225.0
Water (H_2O)	18.02	373.9	22.06	322.0
Carbon Dioxide (CO_2)	44.01	30.9	7.37	467.6
Acetone (C_3H_6O)	58.08	235.1	4.64	278.0
Benzene (C_6H_6)	78.11	289.0	4.90	277.0
Ethane (C_2H_6)	30.07	32.2	4.87	206.2
Ethanol (C_2H_5OH)	46.07	240.9	6.06	276.0
Ethylene (C_2H_4)	28.05	9.2	5.04	214.2
Methane (CH_4)	16.04	-82.6	4.59	162.7
Methanol (CH_3OH)	32.04	239.4	8.10	275.5
n-Propane (C_3H_8)	44.10	96.7	4.25	220.5
Propylene (C_3H_6)	42.08	91.9	4.55	230.1

Thanks to the relatively low operating temperatures, extracts obtained using SC-CO_2 are free of solvent residues and retain sensory properties—such as aroma and flavor—very similar to those of the original natural source. Moreover, although reaching the supercritical state requires a certain energy input, this is largely offset by the minimal energy needed to separate the solvent from the extract. As a result, the overall energy consumption is lower compared to conventional methods like steam distillation [53].

One of the main limitations of supercritical carbon dioxide (SC-CO_2) as a solvent for the extraction of bioactive compounds lies in its low polarity. While SC-CO_2 is highly effective for extracting non-polar and slightly volatile compounds, its capacity to solubilize polar analytes is limited [61]. Consequently, the use of polar co-solvents, such as ethanol or methanol, is often required to enhance solvent polarity and improve extraction efficiency [62].

Since the 1980s, SC-CO_2 has been utilized at the industrial scale for the extraction of a wide variety of compounds, including caffeine from coffee and tea, hops, essential oils, flavor and fragrance compounds, food ingredients, nutraceuticals, as well as active substances used in pharmaceutical and cosmetic formulations [63]. Isoflavones have been successfully extracted from soybean meal using SC-CO_2 under a range of conditions, including temperatures between 40–70 °C and pressures of 30–60 MPa. The addition of aqueous methanol as a co-solvent, at concentrations up to 10.2% w/w, significantly improved extraction efficiency, with 80% aqueous methanol identified as optimal. Under the best conditions (40 °C, 50 MPa, 9.80 kg/h CO_2 flow, 7.8% aqueous methanol), a recovery of 87.3% of the twelve main isoflavones—

including daidzin, genistin, glycitin and their aglycone, acetyl, and malonyl forms—was achieved, as compared to solvent extraction with 70% ethanol [64]. Similarly, SC-CO_2 has been used for the extraction of flavonoids from pomelo peel (Citrus grandis (L.) Osbeck), where optimal conditions (80 °C, 39 MPa, 85% aqueous ethanol, 49 min extraction) yielded 2.37% flavonoids—significantly higher than the 1.51% obtained via conventional solvent extraction (CSE). Moreover, flavonoids extracted with SC-CO_2 exhibited enhanced antioxidant activity in DPPH, ABTS, and hydroxyl radical scavenging assays. These results highlight the potential of SC-CO_2 to efficiently extract high-value compounds with functional benefits in the food, nutraceutical, and pharmaceutical industries [65].

3. High Pressure Equilibrium

Experimental solubility data for a solid solute in a SCF is necessary for determining the operating conditions under which a particular solute exhibits a preferential partitioning into the supercritical phase over other components in a mixture. This information is crucial for the initial stages of design and optimization of SCFE processes at both pilot and industrial scales.

This section begins by examining the solubility behavior of a solid solute in an SCF solvent, providing insight into the phenomenological characteristics of the systems under investigation. Subsequently, a comprehensive overview of the experimental methodologies employed to measure thermodynamic phase equilibrium properties—specifically for high-pressure solid–fluid binary systems—is presented, along with key criteria for selecting an appropriate experimental approach. Two validation strategies for pressure–temperature–composition (p–T–y_i) data in solid–fluid binary systems are then discussed. The section concludes with a presentation of the fundamental thermodynamic equations, methodologies, and selection criteria used in the modeling of multicomponent fluid phase equilibria.

3.1. Solubility Behavior of Solids in a Supercritical Fluid

Solubility refers to the maximum concentration of a compound that can be dissolved in a solvent under specific pressure (p) and temperature (T) conditions. This equilibrium state between solute and solvent is only achieved when enough of the solute is present in the system and equilibrium is established under constant p and T. The solubility of compounds in SC-CO_2 is strongly influenced by several molecular characteristics of the solute, including molecular weight, degree of branching, number and type of rings, nature and position of functional groups, aromaticity, and polarity [66], [67].

3.1.1. Effect of temperature and pressure on solubility in SC-CO_2

The solubility of solid solutes in supercritical fluids is highly sensitive to variations in pressure and temperature. As pressure increases at constant temperature, the density of SC-CO_2 increases, enhancing its solvating power and, consequently, the solubility of the solute. Conversely, the effect of temperature is more complex and depends on the pressure regime. At lower pressures, increasing temperature tends to decrease solubility due to a reduction in solvent density. However, at higher pressures, solubility may increase with temperature because the rise in solute vapor pressure outweighs the decrease in solvent density. This competing behavior leads to what is known as the temperature crossover effect, where

solubility isotherms intersect at a specific pressure. In Figure 3.1 this phenomenon can be observed for the binary system naphthalene and SC-CO_2.

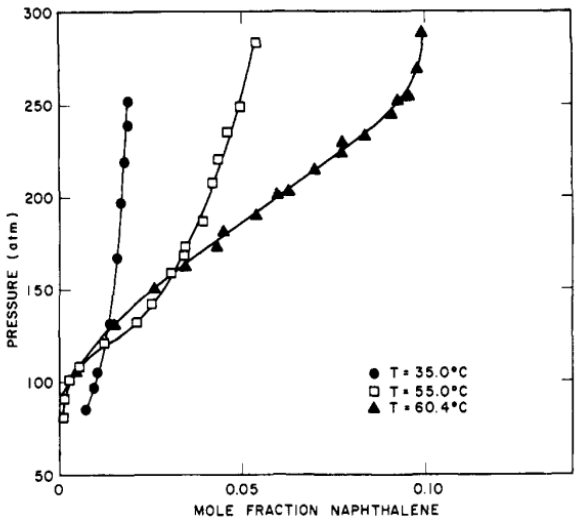

Figure 3.1. Experimental solubilities for solid naphthalene in supercritical carbon dioxide at 35.0, 55.0 and 60.4 °C [68].

3.1.2. Effect of molecular interactions and cosolvents on solubility in SC-CO_2

Solvation of a solid solute in SC-CO_2 occurs through molecular interactions such as van der Waals' forces, dipole interactions, and hydrogen bonding [69]. Non-polar and slightly polar solutes generally exhibit better solubility in SC-CO_2 than polar solutes [70], as CO_2 lacks permanent dipoles and primarily engages in weaker intermolecular forces like van der Waals' force and London dispersion forces. The solubility of a solute in a solvent is influenced by the similarity of their intermolecular forces, with non-polar solutes dissolving more readily in SC-CO_2. In contrast, polar solutes, which require stronger interactions such as hydrogen bonding or dipole-dipole forces, do not dissolve as effectively in SC-CO_2 due to the solvent's limited ability to facilitate these interactions.

Although CO_2 is non-polar overall, it possesses a quadrupole moment due to the electronegativity difference between carbon and oxygen atoms, allowing it to act as a weak Lewis acid or base [71]. This property enables CO_2 to interact with functional groups such as alcohols, ethers, and carbonyl groups on solute molecules, which can enhance the solubility of polar solutes [72]. SC-CO_2 is particularly effective for extracting non-polar and slightly polar compounds, including alkanes, terpenes, aldehydes, esters, alcohols, and fats.

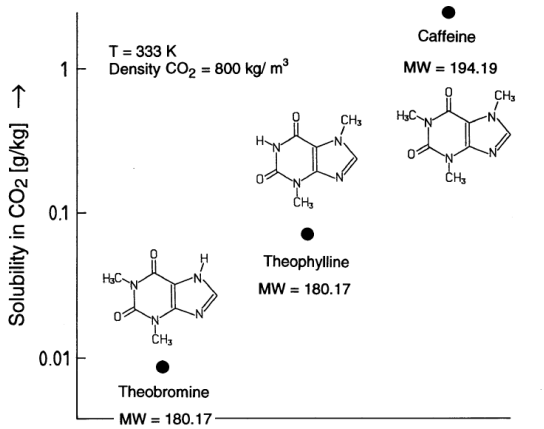

Figure 3.2. Solubility of xanthines in supercritical carbon dioxide at constant density [73].

The influence of solute chemical structure on solubility is clearly demonstrated in Figure 3.2. The solubility of low-volatility substances in non-polar supercritical gases tends to decrease with increasing molecular weight, polarity, and the number of polar functional groups [73]. For larger molecules, the non-polar portion, which correlates with molecular mass, primarily dictates solubility. In contrast, for smaller molecules, functional groups exert a stronger influence.

As previously hypothesized, the molecular structure of biochanin A, specifically the unhindered hydroxyl group at position 7, favors the formation of molecular aggregates via hydrogen bonding. At elevated pressures, the reduction in free volume promotes these solute-solute interactions, leading to the formation of dimers. This dimerization effectively doubles the solute's molecular weight and increases its effective volume, resulting in a macroscopic reduction or stabilization of solubility in the SC-CO_2 phase.

This behavior aligns with the fundamental thermodynamic principles of polymer solubility in supercritical fluids, where solubility typically decreases as chain length and molecular weight increase [74], [75]. At a molecular level, as the molecular weight rises, solute-solute interactions become dominant over solute-solvent interactions. Furthermore, according to Flory's theory, the increase in molecular weight leads to a reduction in the entropy of mixing (ΔS), making the dissolution of heavier associated species thermodynamically less favorable [75].

These trends are corroborated by several examples in SC-CO_2 systems. As illustrated in Figure 3.3, the solubility of Poly(vinylpyrrolidone) consistently decreases as its number-average molecular weight (M_n) increases [75]. For instance, short-chain Poly(vinyl acetate) (MW = 1800 g/mol) exhibits significantly higher solubility (1% wt.) than its longer-chain counterparts (MW

= 5800 g/mol, 0.38% wt.) under identical density conditions [76]. Similarly, the solubility of Poly(ethylene glycol) (PEG) is a direct function of molecular weight, where higher molecular weight chains require substantially higher threshold pressures to initiate dissolution [74].

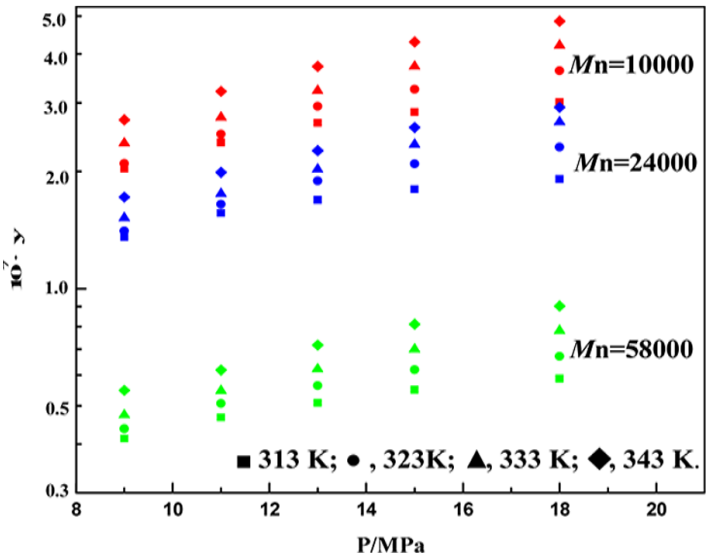

Figure 3.3. Experimental solubility of PVP for (1) Mn = 10000, (2) Mn =24000, and (3) Mn = 58000 in SC-CO_2 as a function of pressure at different temperatures: ■, 313 K; ●, 323 K; ▲, 333 K; and ♦, 343 K [75].

The solubility behavior of solutes in SC-CO_2 can be further enhanced or modified by adding a small amount of another fluid, called entrainer, into the solvent. The entrainer could act in two ways when added to SC-CO_2: as a co-solvent, increasing the solubility of a specific solute or as a modifier, changing the properties of SC-CO_2 such as polarity, density or viscosity. At the molecular level, entrainers enhance solubility through specific interactions. These include hydrogen bonding [77], dispersion forces [78], dipole-dipole interactions, and, in some cases, the formation of charge-transfer complexes [79]. The local concentration of the entrainer around the solute can be significantly higher than its bulk concentration, further amplifying its effect on solubilization [77].

In addition to specific molecular interactions, entrainers modify the physical properties of SC-CO_2. Increase in density caused by entrainers is generally small, changes in the solubility parameter and phase polarity can substantially enhance solubility [80]. The magnitude and nature of the solubility modification depend on the type and concentration of the entrainer, as well as on operating pressure and temperature. Furthermore, some entrainers can act as matrix modifiers by physically altering the structure of the solid substrate, facilitating the release of the solute [78]. This mechanism is distinct from the direct increase of solubility in the supercritical phase.

The choice of an entrainer in SC-CO_2 extraction is influenced by the polarity and functional groups of the solute, as well as the extraction objective. Polar entrainers such as ethanol or methanol are commonly used for polar solutes due to their ability to form hydrogen bonds and dipole–dipole interactions, enhancing solubility by increasing the polarity of the SC-CO_2 phase. In contrast, nonpolar entrainers like alkanes improve the solubility of nonpolar solutes via dispersive interactions and increased polarizability of the solvent [81]. Entrainers can also modify the density and solubility parameter of SC-CO_2, making it more compatible with the target compound [79]. Depending on whether the goal is to maximize solubility or enhance selectivity, entrainers are selected for their affinity toward specific solutes. In many cases, entrainers with GRAS (Generally Recognized as Safe) status are preferred for applications in the food and pharmaceutical industries.

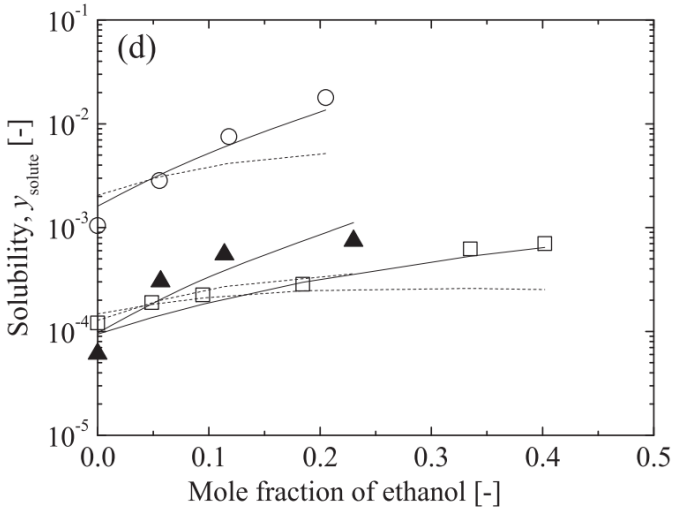

Figure 3.4. Solubility of flavone (○), 6-methoxyflavone (▲) and anthracene (□) as a function of mole fraction of ethanol at 333 K and 22 MPa [82].

As shown in Figure 3.4, the solubility of flavone, 6-methoxyflavone, and anthracene increases with the addition of ethanol to SC-CO_2 at 333 K and 22.0 MPa. This trend reflects the role of ethanol as a polar entrainer that enhances solute–solvent interactions, particularly for polar compounds. Flavone and 6-methoxyflavone benefit from hydrogen bonding and dipole–dipole interactions, resulting in a greater solubility increase compared to the nonpolar anthracene, which is less responsive to polarity changes in the solvent phase.

3.1.3. Solubility of Isoflavones in Supercritical Fluid

Despite the available data for various isoflavones, there are no reports, to the best of our knowledge, concerning the solubility of biochanin A in SC-CO_2. Given its close structural

relationship to isoflavones like genistein and daidzein, it is reasonable to anticipate a similar solubility behavior.

Several studies have investigated the solubility or extraction of isoflavones, either in their aglycone (e.g., genistein, daidzein) or glycosylated forms (e.g., genistin, daidzin), in SC-CO_2 under various conditions [48], [83], [84], [85]. The inclusion of ethanol or methanol as a cosolvent has been shown to significantly enhance solubility and extraction efficiency. Nakada et al. [83] reported the solubility of genistin, daidzin, and their aglycones in SC-CO_2 using ethanol concentrations ranging from 0 to 15% mol/mol at 313 K and pressures of 15 and 25 MPa.

As demonstrated by Nakada et al. [83] the addition of ethanol as a co-solvent dramatically enhances the solubility of isoflavones in supercritical carbon dioxide (SC-CO_2). In a pure SC-CO_2 system without the entrainer, the solubility of isoflavones such as daidzein and genistein is exceptionally low due to the non-polar characteristics of the supercritical fluid. However, the introduction of a polar co-solvent like ethanol significantly increases their solubility, a trend that is consistently observed to rise as the molar fraction of the entrainer increases. As shown in Figure 3.5, this pronounced enhancement effect is predominantly driven by the quantity of ethanol added to the system, proving that the presence of a co-solvent is a highly effective and necessary strategy to overcome the inherent extraction limitations of pure SC-CO_2 when processing these compounds.

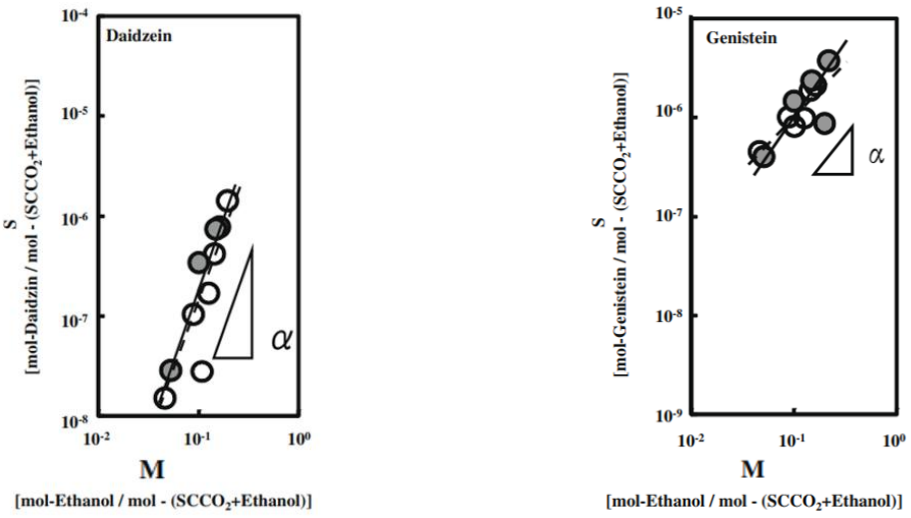

Figure 3.5. Solubility of daidzein and genistein in SC-CO_2 and ethanol binary system at 15 and 25 MPa and at 313 K. 15 MPa (○); 25 MPa (●) [83].

Similarly, Rostagno et al. [48] and Zuo et al. [85] explored methanol as a modifier, observing improved extraction of isoflavones from soybean sources at modifier contents between 5 and 10% mol/mol. Most studies apply moderate temperatures (313–343 K) and pressures ranging from 15 to 60 MPa. These conditions generally enhance solubility by increasing the density and solvent power of SC-CO_2, although the use of cosolvents often reduces the need for very high pressures.

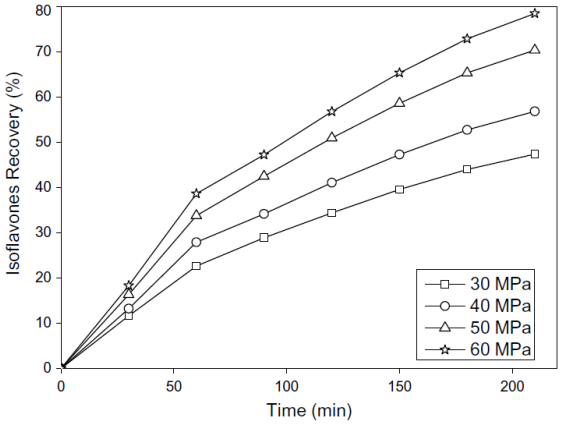

Figure 3.6. Isoflavones recovery curves at different pressure [85].

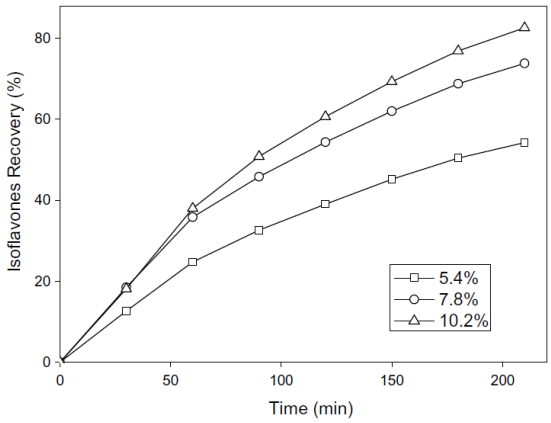

Figure 3.7. Isoflavones recovery curves at different modifier concentration [85].

Regarding extraction processes, the initial linear portion of extraction curves (typically represented as yield or recovery versus cumulative CO_2 consumption or extraction time) has been shown to reflect the solubility-controlled regime. In this region, the mass transfer rate is high enough that the amount of solute extracted is governed primarily by the equilibrium solubility of the compound in SC-CO_2 or the SC-CO_2 + cosolvent mixture, rather than by kinetic limitations. This has been noted in the work of Zuo et al. [85], where trends in the slope of this initial region correlate with changes in modifier concentration, temperature, or pressure, as shown in Figure 3.6 and Figure 3.7.

3.2. Measuring High Pressure Solid + Fluid Phase Equilibrium

Numerous methods are available for experimentally studying high-pressure phase equilibria. Selecting an appropriate method depends on the components' properties and the phenomena under investigation. A comprehensive review of these techniques, categorized by their sources of error and outlining their main advantages and limitations, was published by Dohrn et al. [86]; only a summary is provided below.

There are two main types of methods for measuring fluid phase equilibria at high pressures: analytical and synthetic methods. This classification is based on whether the compositions of the equilibrium phases are determined (analytically), or the mixture is prepared with a known composition (synthetically) [86]. Analytical methods involve direct composition analysis of the coexisting phases. This can be done by sampling and analyzing at ambient pressure or by in-situ analysis under high pressure. These methods provide detailed information, including tie-line data, and are suitable for multicomponent systems. However, they require accurate phase analysis and are prone to errors during sampling, such as pressure drops, adsorption, or incomplete transfer. The main sources of error are related to the precise determination of phase compositions.

Synthetic methods, in contrast, rely on the observation of phase transitions in mixtures of known composition. They do not require sampling and are often simpler to operate. These methods are useful when phase separation is difficult or when densities are similar. Their main limitations include the lack of direct compositional data and the need for precise mixture preparation. Additional challenges include detecting phase transitions and determining properties such as phase volume or density.

In general, analytical methods are preferred when the number and nature of equilibrium phases are known, while synthetic methods are recommended for exploratory studies of phase behavior. Figure 3.8 illustrates the main experimental approaches for measuring fluid phase equilibria under high-pressure conditions.

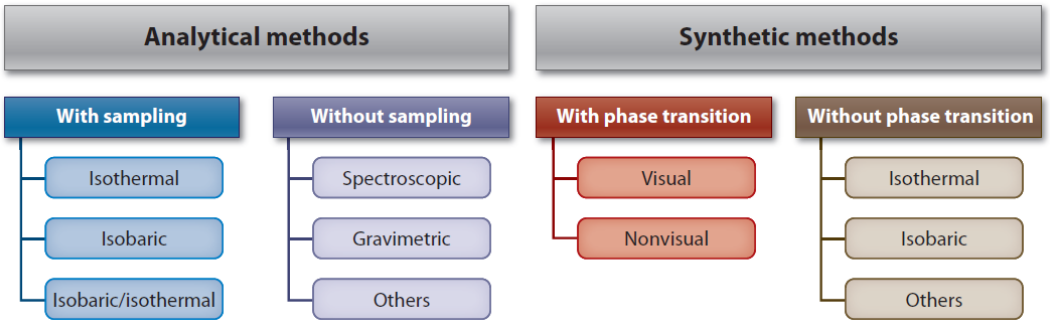

Figure 3.8. Classification of experimental methods for phase equilibria at high pressures [86].

In line with the objectives of this thesis, an analytical-isothermal method will be employed to measure the thermodynamic solubility of the solute at varying pressures and constant temperature. The selection of an analytical method over a synthetic one is justified by the availability of prior information regarding the number and nature of the coexisting phases

(solid and fluid) which is commonly reported for solid solutes in SC-CO_2. This behavior has been particularly observed in compounds belonging to the nobiletin (flavonoid) family [87] and in fat-soluble vitamins [88]at temperatures near ambient conditions.

Analytical-isothermal methods generally comprise three main steps: (a) preparation of the mixture, (b) equilibration of the system, and (c) sampling and analysis of the phase compositions. Among these, the sampling step is the most critical. When sampling from a sealed high-pressure vessel, a pressure drop occurs, altering the total composition of the system. This change triggers a new equilibration process, which may shift both the compositions of the equilibrium phases and the positions of the phase boundaries within the cell. These effects must be carefully considered, particularly when multiple samples are withdrawn.

Several technical strategies are available to minimize the impact of sampling on the equilibrium state of the system [89]. These include the use of large-volume equilibrium cells or small sampling volumes obtained through capillaries or specialized valves, which can reduce the extent of pressure drop. Alternatively, the system pressure may be maintained during sampling by modifying the cell volume (e.g., using a piston or bellows) or by isolating the sample from the equilibrium content prior to withdrawal. Another approach involves compensating for the sample removal by introducing additional fluid into the cell. When advanced valve systems are employed, such as multiport HPLC valves or rapid on-line sample injection (ROLSI™) valves[90], the equilibrium cell can be directly connected to analytical instruments, typically chromatographic techniques such as HPLC, supercritical fluid chromatography (SFC), or gas chromatography (GC). This direct integration prevents exposure of the sample to reactive atmospheric components. Moreover, the extremely low dead volume, minimal sample size, and immediate flushing with a (preheated) inert fluid help to minimize sample loss and contamination. Finally, sampling from a recirculation line has also been shown to reduce errors caused by pressure fluctuations during sampling, including those arising from differential vaporization [91]. Many of these solutions have been implemented in the solubility measurement methodology used in this work as it will be described in Section 4.

3.3. Validation of Experimental Data

The quality and precision of physicochemical property data play a crucial role in the development, simulation, and economic evaluation of chemical processes [92]. For this reason, any study involving the measurement of such data, particularly those related to high-pressure phase equilibrium in the context of chemical thermodynamics, must incorporate a rigorous

assessment of experimental uncertainty to ensure the reliability of the reported values [87]. In the present work, three distinct approaches are employed to validate the experimental results: uncertainty quantification of the measurements, analysis of thermodynamic consistency, and verification of internal data coherence, as detailed in the subsequent sections.

3.3.1 Estimation of Measurement Uncertainties

Measurement uncertainty refers to the parameter associated with the result of a measurement, reflecting the dispersion of values measured from the true value, which is unknown [93]. It represents the degree of doubt about the validity of the result [94]. Uncertainties of properties can be evaluated using two approaches [95]: Type A, based on statistical analysis of repeated observations (repetitions), and Type B, based on external information such as calibration data or instrument specifications. For thermodynamic properties in phase equilibrium studies (e.g., phase compositions, temperature, and pressure) Type A evaluation is generally not suitable. It requires significant time and resources and is typically restricted to assessing repeatability of limited measurements. Instead, Type B evaluation is preferred. For properties like equilibrium temperature and pressure, the standard uncertainty (u) is commonly expressed as one standard deviation, corresponding to a 68.27% confidence level for a normal distribution. This value is often estimated based on the experimental setup, measurement methodology, and supplementary information from the literature or instrument specifications.

Solubility in SC-CO_2 depends on several measured variables. The uncertainty in each variable propagates to the calculated solubility value, y_i. For this reason, it is necessary to report the combined expanded uncertainty, ($U_{Comb}(y_i)$). This value accounts for the contribution of each individual source of uncertainty.

The uncertainty analysis began with the chromatographic areas, $A_{C,i}$ and $A_{S,i}$, obtained from HPLC. The uncertainty (U) was calculated as the standard deviation (σ) of repeated measurements divided by the mean area. This provides a relative measure of data dispersion.

The uncertainty in $C_{S,i}$ was also evaluated. It includes instrumental errors from two key sources. First, the balance used to weigh the solute mass ($m_{S,i}$). Second, the volumetric flask ($V_{S,i}$) used for solution preparation. These errors directly affect the accuracy of solute concentration. Additional uncertainties were introduced by the V_{Loop} and V_{HPLC} devices. The manufacturers provided specifications for these errors. They affect the accuracy of volume handling during experiments.

The density of CO_2 ρ_1 is calculated using the NIST database [96]. Temperature (T) and pressure (p) are used as input variables. The associated uncertainty, $U(\rho_1)$, reflects the influence of both conditions. To estimate this, the isothermal compressibility (κ_1) and the isobaric thermal expansion (α_1) are used. These values are also obtained from NIST [96]. Each coefficient is multiplied by the uncertainty of its respective variable, $U(p)$ or $U(T)$. This allows evaluation of their impact on the calculated density.

$$f = f(x_1, x_2, \dots, x_n) \tag{3.1}$$

$$\mathrm{u_{comb}}(f) = \Delta f = \sum_{i=1}^{n} \left| \frac{\delta f}{\delta x_i} \right| dx_i \tag{3.2}$$

$$\mathrm{U_{comb}}(f) = k \cdot \mathrm{u_{comb}}(f) \tag{3.3}$$

$$f_{\%CI} = f \pm \mathrm{U_{comb}}(f) \tag{3.4}$$

Uncertainty quantification for the solubility of biochanin A in pure CO_2 was carried out by both methods.

- Approach A: For each set of temperature and pressure conditions, three to five back-to-back solubility determinations were made. The observed repeatability exceeded 95%, demonstrating that the experimental setup and protocol provide highly precise measurements.
- Approach B: Both the individual standard uncertainty (u) and the combined expanded uncertainty (U_{comb}) were calculated by propagating the known uncertainties of the apparatus, the methodological steps, and the measured solubility values.

3.3.2 Thermodynamic Consistency Test

Thermodynamic consistency tests are methods used to validate experimental data by ensuring they adhere to the fundamental laws of thermodynamics. They are based on the over determination of experimental properties measured, according to the phase rule, along with the use of the Gibbs–Duhem (G-D) equation to generate values of any one of these properties and to compare them with the laboratory results. Valderrama and Zavaleta [97] described a methodology for assessing thermodynamic consistency that combines the G-D equation with an appropriate calculation of the compressibility factor (Z) and the fugacity coefficients of solute ($\bar{\phi}_2$) and CO_2 ($\bar{\phi}_1$) in the supercritical fluid phase using an equation of state (EoS).For a binary homogenous gas mixture at constant temperature, the Gibbs–Duhem is written as:

$$\frac{Z-1}{P}dP = y_1 d(\ln(\bar{\phi}_1)) + y_2 d(\ln(\bar{\phi}_2)) \tag{3.5}$$

The test proposed by Valderrama and Zavaleta [97] states that the left side of Equation (3.5) should be equal to the right side of it, within acceptable deviations. Equation (3.5) is conveniently expressed in integral form and then arranged to obtain an equation to assess the thermodynamic consistency of each individual data point by using the next data point. This equation is called the area deviation (ΔA_j) and is calculated as:

$$\Delta A_j = \frac{\int_j^{j+1}(y_2 p)dp - \left\{\int_j^{j+1}[(Z-1)\bar{\phi}_2]^{-1}d\bar{\phi}_2 + \int_j^{j+1}(1-y_2)[y_2(Z-1)\bar{\phi}_1]^{-1}d\bar{\phi}_1\right\}}{\int_j^{j+1}(y_2 p)^{-1}dp} \tag{3.6}$$

According to Valderrama and Zavaleta [97], two stages must be completed to validate the model. In the first stage, the selected equation of state (EoS), along with the chosen mixing and combining rules, must adequately describe the solubility (y_i) for each isotherm. The model is considered acceptable if the relative root mean square deviation (RRMSD) between calculated and experimental solubility values is within ±20% [98]. The RRMSD is calculated as the square root of the sum of squared relative differences between calculated (y_i^{calc}) and experimental (y_i) values, divided by the number of data points (N). If this criterion is not met, it is recommended to try a different model.

The second stage involves verifying the thermodynamic consistency of the data. This is done by calculating all (ΔA_j) values using Equation (3.6). If 100% of the values fall within ±20%, the data set is classified as thermodynamically consistent (TC). If only 75% or more of the (ΔA_j) values fall within ±20%, the data is considered not fully consistent. If fewer than 75% of the values meet this condition, the data is classified as thermodynamically inconsistent.

3.3.3 Self-consistency Test

Self-consistency testing is used to evaluate the internal agreement of an experimental solubility data set. One challenge in consistency analysis is the dependence on accurate solid solute properties, such as critical parameters, acentric factor, molar volume, and sublimation pressure. These values are often unavailable, limiting the reliability of equation of state (EoS) models [99], [100].

The semi-empirical model developed by Mendez-Santiago and Teja (MS-T) [101] offers an alternative approach. It correlates solid solubility as a function of temperature, pressure, and the density of pure CO_2. This model eliminates the need for detailed solute property data and

the specific performance of any EoS. The MS-T model includes three temperature-independent adjustable parameters, A, B and C. In this work, the MS-T model is applied according to Equation (3.7) to evaluate the self-consistency of the solubility data. The parameters were fitted from the experimental data by minimizing the RMSD of the y_i values calculated by the model (Equation 3.8), where N is the number of data obtained from sampling. When the model is fitted properly, experimental solubility data for various isotherms may collapse onto a single straight line when plotted against CO_2 density. This behavior, typically observed for densities ranging from half to twice the critical density of CO_2, is considered an indicator of self-consistency [101], [102], [103].

$$T[\ln(p \cdot y_i) - C] = A + B \cdot \rho_i \tag{3.7}$$

$$RMSD = \sqrt{\frac{1}{N} \cdot \sum_{j=1}^{N} \left(\frac{y_i^{model} - y_i}{y_i} \right)_j^2} \tag{3.8}$$

The density of the CO_2-rich phase is approximated using the density of pure CO_2, due to the low solubility of the solid solutes. The accuracy of the correlation decreases for solvent densities less than half the critical density [101] ($\rho_{c,1}$ = 467.6 kg m^{-3} [96]), thus limiting its applicability to data points obtained at low pressure. This limitation emphasizes the need for caution in interpreting results under low solvent density conditions.

It should be noted that, for the application of this self-consistency test, several assumptions had to be made. First, the model considers the system to behave as a dilute solution, assuming that the solute concentration in the solvent is sufficiently low (on the order of 10^{-3} molar fraction) to be treated as infinitely diluted. Under this condition, the activity of the solute can be approximated by its mole fraction, which greatly simplifies thermodynamic calculation [104]. In addition, it is assumed that the adjustable parameters A, B, and C remain constant for a given system over the range of temperatures and pressures studied. Once determined from a set of experimental data, these parameters can therefore be employed to predict solubility at other conditions within the measured T and p ranges without requiring readjustment [101]. Finally, the approach relies on the applicability of a modified Clausius-Clapeyron equation to estimate the sublimation pressure of low-volatility solids. This adaptation is assumed to provide reliable estimates under the conditions of interest, although in practice its validity should always be checked against experimental data whenever available [101].

3.4. Modeling phase equilibria

3.4.1. Procedures and Criterions for Modeling Solid + Fluid Phase Equilibria

For a two-phase system, solid + fluid, of n components, the state of thermodynamic equilibrium is established when temperature, pressure and molar Gibbs free-energy (G_i) of every component *i* of both phases are equal:

$$T^F = T^S \qquad p^F = p^S \qquad G_i^F = G_i^S \qquad (i = 1, \dots, n) \qquad (3.9)$$

The equality of temperature, pressure, and Gibbs free energy between phases implies equal fluxes of heat, momentum, and mass, respectively. In a system at constant temperature and pressure (such as those studied in this work) thermodynamic equilibrium is reached when the total Gibbs free energy of the system is minimized globally.

To evaluate equilibrium using only macroscopic, measurable properties, G. N. Lewis (USA, 1875–1942) introduced the concept of fugacity (f). This concept replaces the direct use of Gibbs free energy by expressing equilibrium in terms of a modified partial pressure. Fugacity ($\bar{f}_i$) is defined as the product of the partial pressure of component *i* in the mixture (p_i) and its fugacity coefficient ($\bar{\phi}_i$), as shown in Equations (3.10) and (3.11). This formulation allows practical application of the equilibrium condition in real systems where direct Gibbs energy measurements are not feasible.

$$d\bar{G}_i = RTd\left(\ln\left(\bar{f}_i\right)\right) \qquad (3.10)$$

$$\bar{f}_i = \bar{\phi}_i \cdot p_i \qquad (3.11)$$

As such, the third equilibrium condition of Equation (3.9) is replaced by the equality of fugacities of each component *i* in both phases, as shown in Equation (3.12).

$$\bar{f}_i^F = \bar{f}_i^S \qquad (3.12)$$

There are two primary strategies for solving Equation (3.12): the isofugacity condition and direct minimization of the Gibbs free energy. One selects the appropriate method according to the system's characteristics. In the case of a two-component, two-phase mixture, as confirmed by visual inspection for the system examined here, there exists only a single Gibbs energy minimum. Thus, the isofugacity approach, being the more straightforward, is employed to solve the fluid-solid equilibria. In this framework, equality of the fugacities for component *i* in the fluid and solid phases is enforced via a $\phi - \phi$ approach, where each fugacity is calculated

directly from Equation (3.11). The fugacity of component i in the fluid phase is then given by Equation (3.13).

$$\bar{f}_i^F = y_i \cdot p \cdot \bar{\phi}_i^F \tag{3.13}$$

Assuming the solid phase is a pure solute, solubility is calculated through the McHugh approach [105], [106]. As such, y_i is calculated according to Equation (3.14).

$$y_i = \frac{p_i^{subl} \cdot \phi_i^{subl} \cdot \exp\left(\frac{V_i^{subl}}{RT} \cdot \left(p - p_i^{subl}\right)\right)}{p \cdot \bar{\phi}_i^F} \tag{3.14}$$

In Equation (3.14), p_i^{subl} is the sublimation pressure of the pure solid solute at the equilibrium temperature, V_i^{subl} is the pure solid solute molar volume, and R is the universal gas constant.

Finally, $\bar{\phi}_i^F$ is calculated with Equation (3.15), adapted for a multicomponent mixture, where V is the molar volume of the mixture and n_i are the moles of component i in the mixture.

$$\ln\left(\bar{\phi}_i^F\right) = \frac{\ln f_i}{y_i \cdot p} = \frac{1}{RT} \cdot \int_{V=\infty}^{V=\frac{Z^F RT}{p}} \left[\frac{RT}{V} - n\left(\frac{\partial p}{\partial n_i}\right)_{T,V,n_{j\neq i}}\right] dV - \ln Z^F \tag{3.15}$$

3.4.2. Procedures and Criterions for Modelling Liquid-Solid Equilibrium

The solubility of a crystalline solid solute in a liquid solvent can be determined from classical thermodynamics by equating the fugacities of the solute in both the pure solid phase and the liquid mixture phase. Under the assumption of pure solid phase, the solid-liquid equilibrium (SLE) is expressed via Equation (3.16).

$$\ln(x_i \cdot \gamma_i) = \frac{\Delta H_{fus,i}}{R} \cdot \left(\frac{1}{T_{m,i}} - \frac{1}{T}\right) + \Delta C_p^{fus} \cdot \left[\frac{T_{m,i}}{T} - 1 - \ln\left(\frac{T_{m,i}}{T}\right)\right] \tag{3.16}$$

The rigorous calculation of solid-liquid equilibrium requires knowledge of the temperature dependence of the heat capacity difference between the subcooled liquid and solid phases, $\Delta C_p^{fus}(T)$. However, experimental data for liquid and solid heat capacities as a function of temperature are scarce for complex organic molecules such as biochanin A. While group-contribution methods or predictive correlations exist to estimate $\Delta C_p^{fus}(T)$, these empirical methods introduce additional parameters and significant cumulative uncertainties into the thermodynamic model. Furthermore, it is well established that within a narrow temperature range far below the critical point, the contribution of the heat capacity term in Equation (3.16)

is secondary compared to the dominant driving force of the melting enthalpy (ΔH_{fus}). As such, Equation (3.16) is simplified to:

$$\ln(x_i \cdot \gamma_i) = \frac{\Delta H_{fus,i}}{R} \cdot \left(\frac{1}{T_{m,i}} - \frac{1}{T}\right) \tag{3.17}$$

The calculation of the activity coefficient γ_1 requires an accurate description of the liquid-phase non-idealities, which in this study is provided by the SAFT-VR Mie equation of state.

3.4.3. SAFT-VR Mie Equation of State

SAFT-VR Mie EoS is an improvement to the original SAFT-VR EoS proposed by Gil-Villegas et al. [107] which in turn originated from SAFT EoS developed by Chapman et al. [108]. SAFT-VR Mie introduced an extra parameter (λ) to adjust the extent of attractive molecular interactions, allowing a more accurate representation of the substance properties [107].

In their research, Gil-Villegas et al. explored several potential energy functions ($u(r)$) using data from molecular simulations. These functions included molecules with different attractive potentials, such as the square well (Equation (3.18)), which is the potential used by SAFT-HR, a model that represents molecular interactions with hard spheres [109], [110]; Sutherland (Equation (3.19)), ideal for modeling polar fluids [107]; and Yukawa (Equation (3.20)), capable of representing electrolytic and colloidal solutions [107]. They also evaluated the Lennard-Jones potential, which is a soft-core potential in which both the repulsive and attractive terms of $u(r)$ have a Sutherland-like shape [107].

$$u_{hs-squared\ well}(r) = \begin{cases} u \to \infty & ; \quad 0 < r/\sigma < 1 \\ -\varepsilon & ; \quad 1 < r/\sigma < \lambda \\ 0 & ; \quad \lambda < r/\sigma \end{cases} \tag{3.18}$$

$$u_{hs-Sutherland}(r) = \begin{cases} u \to \infty & ; \quad 0 < r/\sigma < 1 \\ -\varepsilon \left(\frac{\sigma}{r}\right)^{\lambda} & ; \quad 1 < r/\sigma \end{cases} \tag{3.19}$$

$$u_{hs-Yukawa}(r) = \begin{cases} u \to \infty & ; \quad 0 < r/\sigma < 1 \\ -\varepsilon \dfrac{\exp\left(-\lambda\left(\frac{r}{\sigma} - 1\right)\right)}{r/\sigma} & ; \quad 1 < r/\sigma \end{cases} \tag{3.20}$$

Segment energy (ε) analysis provides information on the intensity of nonspecific intersegment interactions, represented by the potential $u(r)$ [107], [111], indicating their minimum energy. The segment diameter (σ) corresponds to the distance between two segments (r) at which the potential $u(r)$ reaches zero [107], [111], defining the point of tangential contact. When $u(r)$ is

positive, repulsive forces are evident, suggesting a change of sign at $r = \sigma$, the contact initiation point. Interactions between associative sites are modeled by a square-well potential, characterized by its depth ε_{AB} and width κ_{AB}.

Lafitte et al. [111] employed a generalized version of the Lennard-Jones potential, known as the Mie potential (Equation (3.21)), where the exponents for the repulsive and attractive terms of $u(r)$ can have different values. This provides greater flexibility for modeling $u(r)$, allowing its use in compounds with complex behavior.

$$u(r) = \varepsilon \cdot \frac{\lambda_r}{\lambda_r - \lambda_a} \cdot \left(\frac{\lambda_r}{\lambda_a}\right)^{\frac{\lambda_a}{\lambda_r - \lambda_a}} \cdot \left(\left(\frac{\sigma}{r}\right)^{\lambda_r} - \left(\frac{\sigma}{r}\right)^{\lambda_a}\right) \tag{3.21}$$

Parameters λ_r and λ_a describe repulsive and attractive forces respectively [111]. λ_r provides information about the "central hardness" by determining how rapidly $u(r)$ rises as interacting particles approach the segment core. A high value of λ_r reflects extreme solid-core behavior. In contrast, λ_a influences the extent of the attractive forces, with a smaller value implying a more gradual decrease as r approaches infinity. The well-known Lennard-Jones potential arises from Equation (3.21) by setting $\lambda_r = 12$ and $\lambda_a = 6$ [107], [111].

Adequate representation of a molecule requires determining specific parameters along with the number of segments (m). For example, Mejía et al. [112] employed a Coarse Graining method based on the Theory of Corresponding States to identify the appropriate parameters in Equation (3.21) and the value of m that best fits each molecule.

The value of m plays a crucial role in the physicochemical representation of the molecule. In the case of CO_2, due to its non-spherical shape and small size, CO_2 was assigned an m value of 2, which is supported by experimental data [111].

To ensure a consistent representation, the value of λ_a was set to 6 for all species studied. This adjustment is because, by setting a value of 6, we are considering a direct proportionality with the value of r^6, which is typical of London dispersion forces or Van der Waals dispersion-type forces [111].

Once the value of m is established, λ_r, ε, and σ are calculated using the correlations proposed by Mejía et al. [112]. For the calculation of λ_r, Equation (3.22) will be used, where ω_i is the acentric factor of compound i. a_j, b_j, c_j, d_j, f_j, g_j are the constants of the Padé series, presented in Table 3.1, which depend on the value of m selected [112].

$$\lambda_{r,i} = \frac{\sum_{j=0} a_j \omega_i^j}{1 + \sum_{j=1} b_j \omega_i^j} \tag{3.22}$$

To obtain the value of segment energy (ε) Equation (3.23) is used to obtain reduced critical temperature and Equation (3.24) to finally obtain the segment energy, where $T_{c,i}$ is the critical temperature of compound i, k_B is the Boltzmann constant and α_i is the equivalent of SAFT-VR Mie for the Van der Waals attractive parameter, calculated with Equation (3.25) [112].

$$T_{c,i}^* = \frac{\sum_{j=0} c_j \alpha_i^j}{1 + \sum_{j=1} d_j \alpha_i^j} \tag{3.23}$$

$$\varepsilon = \frac{k_B T_{c,i}}{T_{c,i}^*} \tag{3.24}$$

$$\alpha_i = \left(\frac{\lambda_{r,i}}{\lambda_{r,i} - 6}\right)\left(\frac{\lambda_{r,i}}{6}\right)^{\frac{6}{\lambda_{r,i}-6}}\left(\frac{1}{3} - \frac{1}{\lambda_{r,i} - 3}\right) \tag{3.25}$$

To obtain the segment diameter (σ), the reduced liquid density ρ_i^* of compound i is calculated at a reduced temperature $T_r = 0.7$ with Padé constants (Equation (3.26))[112]. Segment diameter is obtained through Equation (3.27) [112], where N_A is the Avogadro's number and v_i the molar volume at reduced temperature of 0.7, which is calculated with Rackett's Equation (Equation (3.28)).

$$\rho_i^*|_{T_r=0.7} = \frac{\sum_{j=0} f_j \, \alpha_i^j}{1 + \sum_{j=1} g_j \alpha_i^j} \tag{3.26}$$

$$\sigma_i = \sqrt[3]{\frac{\rho_i^*|_{T_r=0.7} \cdot v_i|_{T_r=0.7}}{N_A}} \tag{3.27}$$

$$v_i = v_{i,c}\left(\frac{p_{c,i} v_{i,c}}{R T_{c,i}}\right)^{(1-T_r)^{2/7}} \tag{3.28}$$

Table 3.1. Padé series constants for the values of the number of segments (m) used, taken from Mejía et al. [112].

m_i = 2 (CO_2)						
Constant	j = 0	j = 1	j = 2	j = 3	j = 4	j = 5
a_j	8.0034	-22.5111	3.575	60.3129	-	-
b_j	-	-5.2669	10.2299	-6.486	-	-
c_j	0.1125	1.5404	-5.8769	5.2427	-	-
d_j	-	-3.1954	2.5174	0.3518	-0.1654	-
f_j	-0.0696	-1.944	6.2575	-5.4431	0.8731	-
g_j	-	-10.5646	25.4914	-20.5091	3.6753	-

Table 3.1. Padé series constants for the values of the number of segments (m) used, taken from Mejía et al [112]. Cont.

m_i = 6 (Biochanin A)						
Constant	j = 0	j = 1	j = 2	j = 3	j = 4	j = 5
a_j	5.9217	-8.0711	0.4264	2.56	-	-
b_j		-2.5291	2.1864	-0.6298	-	-
c_j	0.1302	1.9357	-6.4591	5.1864	-	-
d_j		-3.1075	2.8058	-0.4375	-	-
f_j	0.2665	-0.4268	-0.2732	0.6486	-	-
g_j		1.7499	-10.137	9.4381	-	-

To solve equations 3.22 to 3.29 properties of CO_2 are obtained from NIST [96]. Additionally, the critical properties of biochanin A ($p_{c,i}$, $T_{c,i}$, $v_{c,i}$,), normal boiling point ($T_{b,i}$) and melting point ($T_{m,i}$) are estimated with group contributions methods developed by Constantinou & Gani [113] and Joback-Reid [114]. Critical properties of the studied molecules are presented in Table 3.2, along with their molecular weight which were obtained from literature [96], [115].

For biochanin A, all molecular parameters (m, σ, ϵ/k_b, λ_r) and association parameters (ε^{AB}/k_b, κ^{AB}) are fit to experimental data of the solute's solubility in ethanol and 2-Propanol.

$$\omega_i = -\frac{\ln\left(\frac{p_{c,i}}{0.101325}\right) + f_i^{(0)}}{f_i^{(1)}} \tag{3.29}$$

$$f_i^{(0)} = \frac{-5.97616\left(1-\frac{T_{b,i}}{T_{c,i}}\right) + 1.29874\left(1-\frac{T_{b,i}}{T_{c,i}}\right)^{1.5} - 0.60394\left(1-\frac{T_{b,i}}{T_{c,i}}\right)^{2.5} - 1.06841\left(1-\frac{T_{b,i}}{T_{c,i}}\right)^{5}}{T_{b,i}/T_{c,i}} \tag{3.30}$$

$$f_i^{(1)} = \frac{-5.03365\left(1-\frac{T_{b,i}}{T_{c,i}}\right) + 1.11505\left(1-\frac{T_{b,i}}{T_{c,i}}\right)^{1.5} - 5.41217\left(1-\frac{T_{b,i}}{T_{c,i}}\right)^{2.5} - 7.46628\left(1-\frac{T_{b,i}}{T_{c,i}}\right)^{5}}{T_{b,i}/T_{c,i}} \tag{3.31}$$

Table 3.2. Properties of pure components for carbon dioxide (1), biochanin A - monomer (2) obtained from the literature or estimated in this work.

Property	Value	Source (Estimation Method)	Reference
Carbon Dioxide			
Molecular Weight (MW_1/Da)	44.01	NIST	[96]
Critical Temperature ($T_{c,1}$/K)	304.2	NIST	
Critical Pressure ($p_{c,1}$/MPa)	7.38	NIST	
Acentric Factor (ω_1)	0.2252	NIST	

Table 3.2. Properties of pure components for carbon dioxide (1), biochanin A - monomer (2) obtained from the literature or estimated in this work. (Cont.)

Property	Value	Source (Estimation Method)	Reference
Biochanin A			
Molecular Weight (MW_2/Da)	284.26	-	[115]
Critical Temperature ($T_{c,2}$/K)	717.522	Constantinou-Gani	[113]
Critical Pressure ($p_{c,2}$/MPa)	3.877	Constantinou-Gani	
Critical Volume ($\tilde{V}_{c,2}$·10^6/m^3·mol^{-1})	835.6	Constantinou-Gani	
Acentric Factor (ω_2)	0.7191	Joback	[114]
Fusion Enthalpy Change ($\Delta\tilde{H}_{fus,2}$ / J·mol^{-1})	44729	Joback	
Melting Temperature ($T_{m,2}$ / K)	404.11	Joback	

Combining rules are needed to model interactions between solvents (CO_2, ethanol and 2-Propanol) and solute (biochanin A). These combining rules are detailed in equations (3.32) for σ_{1i}, (3.33) for ε and (3.34) for $\lambda_{r,1i}$, these come from the work of Lafitte et al. [111]. It is important to note that the adjustable parameter k_{ij} of the SAFT-VR Mie EoS are fitted to the experimental data. The interaction parameter between CO_2 and biochanin A (k_{12}) is adjusted as function of the form $k_{12} = A + B \cdot (1/T - 1/313.15)$. The fit is performed using a mean square error minimization approach for the differences between the solubility calculated by the SAFT-VR Mie model and the experimental data.

$$\sigma_{ij} = \frac{1}{2}(\sigma_i + \sigma_j) \tag{3.32}$$

$$\varepsilon_{ij} = (1 - k_{ij}) \cdot \frac{\sqrt{\sigma_i^3 \sigma_j^3}}{\sigma_{ij}^3} \cdot \sqrt{\varepsilon_i \varepsilon_j} \tag{3.33}$$

$$\lambda_{r,ij} = 3 + \sqrt{(\lambda_{r,j} - 3)(\lambda_{r,j} - 3)} \tag{3.34}$$

A temperature-dependent segment diameter (d) is also defined within the SAFT-VR Mie formulation (Equation (3.35)). This parameter represents the equivalent repulsive effect that the original soft sphere fluid of diameter σ would have if it were a hard sphere fluid [111]. Its combination rule is the same as that of σ and is presented in Equation (3.36) [111].

$$d_i = \int_0^{\sigma_i} \left(1 - \exp\left(-\frac{u_i(r)}{k_B T}\right)\right) dr \tag{3.35}$$

$$d_{ij} = \frac{1}{2} \cdot (d_i + d_j) \tag{3.36}$$

For model representation, the SAFT-VR Mie EoS quantifies the system properties by the residual Helmholtz free energy (a_r) (Equation (3.37)), which is split into contributions from segment-segment interactions (a^{mono}), chain formation (a^{chain}) and association (a^{assoc}) to more accurately account for their individual effect and thus quantify the interactions of the segments with those of other molecules through weaker, non-specific forces such as induced dipoles and London dispersion forces; and they may have one or more association sites that allow them to establish links with other chains through strong, short-range, and specific interactions such as hydrogen bonds [111].

$$a^r = a^{mono} + a^{chain} + a^{assoc} \tag{3.37}$$

a^{mono} refers to both the repulsive and attractive interactions between the segments within the system. That is, the attractive interactions are modeled as perturbations of the repulsive effect by expressing them up to the third order, as detailed in Equations (3.38) and (3.39) [111], where $a_{1,ij}$, $a_{2,ij}$ and $a_{3,ij}$ are the perturbation terms representing attractive forces, which are determined according to Lafitte et al. [111]. This implies that not only the direct repulsive forces between the segments are considered, but also how the attractive interactions modify this repulsive dynamics to a specific degree. This approach allows to more accurately capture the complexity of molecular interactions and their effects on the system properties [111].

$$a^{mono} = a^m \sum_{i=1}^{N} y_i m_i \tag{3.38}$$

$$a^m = a^{hs} + \sum_{i=1}^{N}\sum_{j=1}^{N} y_i y_j \left(\frac{a_{1,ij}}{k_B T} + \frac{a_{2,ij}}{(k_B T)^2} + \frac{a_{3,ij}}{(k_B T)^3}\right) \tag{3.39}$$

a^{hs} is calculated as described in Equation (3.40), where ρ_s is the total number density of spherical segments (Equation (3.41)) and ζ_l are functions that are described as a reduced density of mixture, whose expression is shown in Equation (3.42) [111].

$$a^{hs} = \frac{6}{\pi \rho_s}\left[\left(\frac{\zeta_2^3}{\zeta_3^2} - \zeta_0\right)\ln(1-\zeta_3) + \frac{3\zeta_1\zeta_2}{1-\zeta_3} + \frac{\zeta_2^3}{\zeta_3(1-\zeta_3)^2}\right] \tag{3.40}$$

$$\rho_S = \rho N_A \sum_{i=1}^{N} x_i m_i \tag{3.41}$$

$$\zeta_l = \frac{\pi \rho_s}{6}\left(\sum_{i=1}^{N} x_{s,i} d_{ii}^l\right) \tag{3.42}$$

$x_{s,i}$ is defined as the molar fraction of segments of component i, and its expression is presented in Equation (3.43).

$$x_{s,i} = \frac{m_i y_i}{\sum_{k=1}^{N} m_k y_k} \tag{3.43}$$

The a^{chain} term accounts for the contribution of intramolecular covalent bonds to the residual free energy (a^r) by employing a two-segment RDF. To incorporate the effects of attractive forces between segments and their impact on spatial arrangement, a^{chain} utilizes second-order perturbation terms applied to the hard-sphere RDF, following a logic comparable to the a^{mono} modeling [111]. This relationship is formalized in Equation (3.44).

$$a^{chain} = -\sum_{i=1}^{N} y_i (m_i - 1)\, ln\, g_{ii}^{Mie}(\sigma_{ii}) \tag{3.44}$$

Furthermore, $g_{ii}^{Mie}(\sigma_{ii})$ is detailed in Equation (3.45), where $g_{d,ii}^{hs}(\sigma_{ii})$ represent the hard-sphere fluid RDF at the tangential contact point between segments of the same molecule ($r = \sigma_i$), as derived in Equations (3.46) and (3.47) [111]. The perturbation terms $g_1^{Mie}(\sigma_{ii})$ and $g_2^{Mie}(\sigma_{ii})$, also calculated at $r = \sigma_i$, are intrinsically linked to the a^{mono} perturbation terms, with $g_1^{Mie}(\sigma_{ii})$ and $g_2^{Mie}(\sigma_{ii})$ mirroring the structures of $a_{1,ij}$ and $a_{2,ij}$, respectively [111].

$$g_{ii}^{Mie}(\sigma_{ii}) = g_{ii}^{HS} \cdot \exp\left[\frac{\varepsilon_{ii}}{k_B T} \cdot \left(\frac{g_{1,ii}^{Mie}(\sigma_{ii})}{g_{d,ii}^{hs}(\sigma_{ii})}\right) + \left(\frac{\varepsilon_{ii}}{k_B T}\right)^2 \cdot \left(\frac{g_{2,ii}^{Mie}(\sigma_{ii})}{g_{d,ii}^{hs}(\sigma_{ii})}\right)\right] \tag{3.45}$$

$$g_{ii}^{hs}(\sigma_{ii}) = \exp\left(-\ln(1-\zeta_x) + \frac{42\zeta_x - 39\eta{\zeta_x}^2 + 9{\zeta_x}^3 - 2{\zeta_x}^4}{6(1-\zeta_x)^3} + \frac{{\zeta_x}^4 + 6{\zeta_x}^2 - 12\zeta_x}{2(1-\zeta_x)^3} \cdot \left(\frac{\sigma_i}{d_i}\right) - \frac{3{\zeta_x}^2}{8(1-\zeta_x)^2} \cdot \left(\frac{\sigma_i}{d_i}\right)^2 + \frac{-{\zeta_x}^4 + 3{\zeta_x}^2 + 3\zeta_x}{6(1-\zeta_x)^3} \cdot \left(\frac{\sigma_i}{d_i}\right)^3\right) \tag{3.46}$$

$$\zeta_x = \frac{\pi \rho_s}{6} \sum_{i=1}^{N} \sum_{j}^{N} x_{s,i} x_{s,j} d_{ij}^3 \tag{3.47}$$

The a^{assoc} represents the contribution from association sites that enable compounds to aggregate into dimers or polymers through specific interactions [109]. Calculating a^{assoc} requires the identification of associative groups within the molecule and their corresponding association scheme. A group is classified as associative if their molecules can establish strong, directional, and specific bonds—such as hydrogen bonds—which markedly influence thermodynamic behavior and phase equilibria. These interactions result in a higher degree of molecular organization and intensity compared to non-associative fluids, where forces are primarily dispersive and less directional [116].

Regarding the molecules, both the solid solute and the co-solvent ethanol possess associative -OH groups. In the specific case of biochanin A, both hydroxyl groups are treated as active association sites. In contrast CO_2 is considered a non-associating species ($a^{assoc} = 0$).

Following the framework defined by Lafitte et al. [111], the -OH groups can be modeled either with a 2B or 4C association scheme. The former accounts for one donor and one acceptor site, both on the hydroxyl group in carbon 7, as it is unhindered by other functional groups. 4C scheme accounts for four distinct sites: one on each hydrogen (H) and the other ones the oxygens' lone pairs of electrons (e). Consequently, since CO_2 is inert, Equation (3.48) is used to determine the mole fraction of unassociated sites for the solute ($X^{A,i}$) [111].

$$X^{A,i} = \frac{-1 + \sqrt{1 + 8\rho\Delta^{A,i,B,j}}}{4\rho\Delta^{A,i,B,j}} \tag{3.48}$$

The term $\Delta_{a,b,i,j}$ represents the association bond strength between site A of compound i and site B of compound j. It is calculated with Equation (3.49), where $g_d^{hs}(d_{ij})$ is a function described in Equation (3.50). The association bond strength is a function of the bonding energy volume (κ_{AB}). While κ_{AB} is a fundamental parameter in the EoS, it is not always provided directly. Instead, it is frequently derived through simplified expressions, such as the one proposed by Lafitte et al [111] (Equation 3.51), which calculates κ_{AB} based on the cutoff distance r_{AB}^c and the association range r_{AB}^d.

$$\Delta_{a,b,i,j} = g_d^{hs}(d_{ij}) \cdot \left[\exp\left(\frac{\varepsilon_{AB}}{k_B T}\right)\right] \kappa_{AB} \sigma_{ij}^3 \tag{3.49}$$

$$g_d^{hs}(d_{ij}) = \frac{1}{1-\zeta_3} + 3\frac{d_{ii}d_{jj}}{d_{ii}+d_{jj}} \cdot \frac{\zeta_2}{(1-\zeta_3)^2} + 2\left(\frac{d_{ii}d_{jj}}{d_{ii}+d_{jj}}\right)^2 \cdot \frac{\zeta_2^2}{(1-\zeta_3)^3} \tag{3.50}$$

$$\kappa_{AB} = \frac{4\pi d_{ij}^2}{72\left(r_{AB}^d\right)^2 \sigma_{ij}^3} \left(\begin{array}{c} \ln\left(\frac{r_{AB}^c + 2r_{AB}^d}{d_{ij}}\right)\left(6(r_{AB}^c)^3 + 18(r_{AB}^c)^2 r_{AB}^d - 24\left(r_{AB}^d\right)^3\right) + \\ (r_{AB}^c + 2r_{AB}^d - d_{ij})(22\left(r_{AB}^d\right)^2 - 5r_{AB}^c r_{AB}^d - 7r_{AB}^d d_{ij} - 8(r_{AB}^c)^2 + r_{AB}^c d_{ij} + d_{ij}^2) \end{array} \right) \tag{3.51}$$

These numerical values for ε_{AB}/k_B and κ_{AB} are essential for calculating the total association contribution a^{assoc}, where the number of site types (w_i) and the frequency of each type (n_{ai}) within the molecule must be explicitly defined.

$$a^{assoc} = \sum_{i=1}^{N}\left[x_i \sum_{a=1}^{w_i}\left(n_{a,i} \cdot \left(\ln X_{a,i} - \frac{X_{a,i}}{2} + \frac{1}{2}\right)\right)\right] \tag{3.52}$$

Once all residual free energy (a^r) contributions are established, solubility can be determined by applying the fundamental condition of phase equilibrium. The SAFT-VR Mie model utilizes the isofugacity criterion to define the thermodynamic equilibrium between the solid solute and the supercritical phase. This condition, which ensures no net mass transfer occurs between phases, is expressed by Equation (3.53).

$$y_i \bar{\phi}_i p = p_i^{subl} \cdot \phi_i^{subl} \cdot exp\left(\frac{V_i^{subl}}{RT} \cdot \left(p - p_i^{subl}\right)\right) \tag{3.53}$$

In this context, V_i^{subl} represents the molar volume of the solute in its solid state, estimated here via the Immirzi-Perini group contribution method [117]. The fugacity coefficient of the solute in the supercritical phase, $\bar{\phi}_i$ is derived from a^r as shown in Equations (3.54) and (3.55).

The solute's sublimation pressure, p_i^{subl}, was calculated using the Grain-Watson method [118], with results summarized in Table 3.3. Due to the typically low values of p_i^{subl}, the fugacity coefficient at the sublimation point (ϕ_i^{subl}) is assumed to be unity.

$$z = 1 + \rho_1 \frac{\partial a^r}{\partial \rho_1} \tag{3.54}$$

$$\bar{\phi}_i = \exp\left(a^r + z - 1 + \frac{\partial a^r}{\partial y_i} - y_1 \frac{\partial a^r}{\partial y_1} - y_i \frac{\partial a^r}{\partial y_i} + \ln z\right) \tag{3.55}$$

Physical properties of the solute were estimated through various GC methods (Constantinou-Gani, and Immirzi-Perini) [114], [117], [119]. This predictive approach was necessary because experimental data for boiling points (T_b), melting temperatures ($T_{m,i}$) and sublimation pressures (p_i^{subl}) are often difficult to obtain due to thermal degradation risks and the high cost of specialized equipment.

In these dilute binary systems, the mole fraction of the solute (y_i) is generally below 0.01 mol·mol^{-1}. Consequently, the properties of the supercritical phase are nearly identical to those of pure CO_2, allowing for the simplified representation of the system pressure through Equation (3.56).

$$p = zRT\rho_1 \tag{3.56}$$

Next, a 2 by 2 system of equations is defined, where y_i and ρ_1 are the unknown variables, restricted by Equations (3.53) and (3.56) for the binary system. The system was solved using the Clapeyron.jl package [120] in the coding language Julia.

Table 3.3. Physical properties of the solute required for modeling with the Statistical Theory of Association of Variable Range Fluids with Mie potential energy equation of state (SAFT-VR Mie EoS).

					p_i^{subl} (c) /MPa		
i	Compound	V_i^S (a) / cm³·mol⁻¹	$T_{m,i}$ (d) / K	$T_{b,i}$ (b) / K	313 K	323 K	333 K
2	Biochanin A (Monomer)	205.17	404.11	698.46	$2.34 \cdot 10^{-12}$	$8.67 \cdot 10^{-12}$	$4.03 \cdot 10^{-11}$
5	Biochanin A (Dimer)	410.34	-	838.03	$2.73 \cdot 10^{-17}$	$1.48 \cdot 10^{-16}$	$1.07 \cdot 10^{-15}$

(a) Calculated with Immirzi-Perini method.
(b) Determined with Constantinou-Gani Method.
(c) Estimated with Grain-Watson method.
(d) [121]

The primary advantage of the SAFT-VR Mie EoS lies in its ability to provide a more rigorous description of real repulsive and attractive molecular interactions compared to the empirical a and b parameters used in cubic equations of state [111]. Furthermore, this framework allows for the prediction of phase behavior in CO_2 + solute systems beyond the experimental conditions studied. This is achieved using only a single binary interaction parameter k_{ij} for experimental fitting.

Previous studies have successfully implemented the SAFT-VR Mie model to characterize the solubility of organic compounds, specifically dichlone derivatives, in supercritical CO_2. For instance, Morales-Díaz et al. [122] demonstrated that SAFT-VR Mie offered superior predictive performance with an average absolute deviation of 25.61%, outperforming the SAFT-HR model. Similarly, Schulz et al. [123] found that SAFT-VR Mie surpassed solubility models based on Molecular Connectivity Indices (MCI).

4. Materials and Methods

The materials, experimental equipment and methodology used in this work for measuring the thermodynamic solubility of biochanin A in pure and ethanol-modified SC-CO_2 are presented in this section.

4.1. Materials

The solubility measurements in supercritical CO_2 employed the following reagents: biochanin A provided by Xi'an International Healthcare Factory Co., Ltd. and carbon dioxide provided by AGA-Chile S.A. Table 4.1 presents detailed specifications for each of these chemical samples.

Table 4.1. Specification of chemical samples.

Chemical Name	Source	Initial mass fraction purity, kg·kg^{-1}	Purification method	Final mass fraction purity, kg·kg^{-1}	Analysis Method
Carbon dioxide	AGA-Chile S.A.	0.9999	None	0.9999	None
Biochanin A	Xi'an International Healthcare Factory Co., Ltd	0.9900	None	0.9900	HPLC
Acetic Acid	Merck KGaA	0.998	None	0.998	GC
Methanol	Tedia Company LLC	0.999	None	0.999	GC
Water	Scharlau	0.9999	None	0.9999	GC
Ethanol	Merck KGaA	0.999	None	0.999	GC
2-Propanol	Merck KGaA	0.999	None	0.999	GC

4.2. Experimental Equipment

The apparatus employed for solubility measurements in supercritical CO_2 (Figure 4.1) comprised a 100 cm^3 view-cell placed in a temperature-controlled air-bath (Thar-Tech, Pittsburgh, PA) equipped with an internal stirrer, a Teledyne ISCO 260D syringe pump (Lincoln, NE) for CO_2 charging and pressure control, and a GAH-T23 gear pump (Eurotechnica, Bargteheide, Germany) to recirculate the CO_2-rich phase and promote equilibrium. The recirculation loop was housed within an insulated acrylic enclosure to ensure constant temperature conditions. Sampling of the fluid phase for solute quantification was performed via a Perkin Elmer Series 200 HPLC (Shelton, CT) system, coupled to a series 200 UV-Vis detector.

A high-pressure, six-port sampling valve (Rheodyne 7010, Rohnert Park, CA) equipped with a 20 µL loop was employed to introduce aliquots of the CO_2-rich phase into the HPLC for solubility analysis. Because the view-cell, recirculation pump, and sampling valve are interconnected in a closed loop, and maintained under constant recirculation, the loop itself equilibrates to the same temperature, pressure, and composition as the fluid inside the cell.

Validation of the apparatus was conducted by measuring the binary system ethanol + CO_2 equilibrium isotherms and comparing them with literature data. The standard errors in CO_2 composition was between 0.1% and 0.6% for the solute mole fraction (x_1) and between 0.1% and 1.6% for the supercritical phase (y_1).

A full account of the equipment and methodology is available in reference [124], while only a concise overview is provided in the following section.

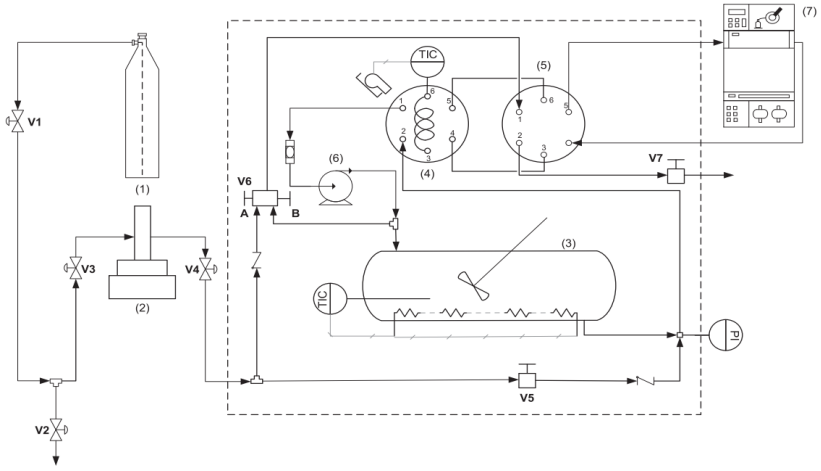

Figure 4.1. Schematic diagram of the experimental apparatus used to measure high-pressure phase equilibrium [125].

4.3. Experimental Methodology

4.3.1. High Pressure Solid + Fluid Experiment

The solubility of the solute in SC-CO_2 was determined using a dynamic-analytical approach [87]. First, the equilibrium cell was charged with an excess amount of solute (typically 2.5–3.0 g, adjusted according to expected solubility) to ensure saturation of the supercritical phase. Any residual air was then purged by displacing it with CO_2 from a high-pressure cylinder, aided by a Welch vacuum pump (Skokie, IL). Subsequently, CO_2 was introduced into the cell via a Teledyne ISCO syringe pump to reach the target pressure. Once both solid and fluid phases were present, as confirmed visually through the view-cell's dual sapphire windows at each temperature and pressure condition, magnetic stirring and recirculation of the CO_2-rich phase were initiated to achieve equilibrium. The solubility isotherm was constructed by incrementally increasing the system pressure via additional CO_2 injection until the desired final pressure was attained [126]. To generate isotherms at different temperatures, the entire procedure was repeated using the new thermal set-point.

4.3.2. *Sampling and analysis of carbon dioxide rich phase*

Before withdrawing samples of the CO_2-rich phase from the equilibrium cell to quantify the dissolved solute, the chromatographic response of a stock solution with a known concentration of biochanin A was established for calibration purposes. This was performed by directly injecting aliquots of the stock solution into the HPLC using a syringe. Each injection was repeated at least five times to obtain an average response with a repeatability of approximately 95%. Calibration was verified daily to ensure the reliable performance of the HPLC system.

The solute content in aliquots taken from the cell was analyzed using the slightly modified isocratic HPLC method of Robert et al. [127]. The mobile phase consisted of a 30:70 v/v mixture of HPLC-grade water from Scharlau (Barcelona, Spain) containing 0.1% glacial acetic acid from Merck KGaA (Darmstadt, Germany) and HPLC-grade methanol from Tedia Company LLC (Ohio, USA), delivered at a flow rate of 1.0 mL·min^{-1}. A reverse-phase C18 column (4.6 mm inner diameter × 25 cm length, 5 µm particle size; Waters Symmetry, Waters, Milford, MA) packed with 5-µm stationary phase particles was maintained at 30 °C in the column oven. Biochanin A was detected at a wavelength of 260 nm. For calibration, a standard solution containing 50 µg·mL^{-1} of biochanin A was prepared in the mobile phase, starting from a stock solution of 1000 µg·mL^{-1} biochanin A in methanol.

After temperature, pressure, and phase equilibrium were reached in the cell (typically after eight hours of equilibration) [128], samples were withdrawn using a six-way valve with the recirculation pump turned off. The withdrawn aliquots were sufficiently small (20 µL) so as not to disturb the equilibrium. At least five replicate injections were performed for each experimental condition, achieving a repeatability of ~95%. After each run, the sample loop was flushed with supercritical CO_2 to avoid contamination with mobile phase of the HPLC between measurements.

4.3.3. *Low Pressure Solid + Liquid Experiment*

The solubility of biochanin A in pure ethanol and 2-propanol was measured at atmospheric pressure and temperatures ranging from 35 to 60 °C (35, 40, 45, 50, 55, and 60 °C). Briefly, 1.0 mL of solvent was placed in a 2 mL Eppendorf tube and thermostated in a Thermomixer (Thermo Scientific, USA) at the desired temperature under continuous stirring (1000 rpm). Biochanin A was added incrementally until a persistent solid phase was observed. The suspension was stirred for 3 h and then allowed to settle for 30 min to ensure solid–liquid equilibrium.

A 0.10 mL aliquot of the clear supernatant was withdrawn, diluted with the corresponding solvent, and analyzed by HPLC using an external calibration curve. If complete dissolution occurred after equilibration, additional solute was added and the procedure was repeated until excess solid remained present. The concentration of the saturated liquid phase was taken as the equilibrium solubility. All measurements were performed in triplicate and are reported as mean values ± standard deviations.

4.3.4. Solubility quantification

The solubility values (y_i) were determined using Equation (4.1) [126], where the chromatographic signal—expressed as the peak area (A_i) corresponding to a 20 µL aliquot (Rheodyne, Rohnert Park, CA) withdrawn from the equilibrium cell loop (V_{iv})—was compared against the peak area (A_{si}) obtained from a 20 µL aliquot (V_s) of a calibration stock solution of known concentration (C_{s2}) injected through the HPLC loop. The calculation also required the molar mass of CO_2 (MW_1) and its specific volume at the experimental conditions (v_1), which were estimated as functions of temperature and pressure using the NIST database [96]. In applying Equation (4.1), it was assumed that the density of the mixture is equal to that of pure CO_2, an approximation considered valid for solute mole fractions below $1{\cdot}10^{-3}$ mol·mol^{-1}.

$$y_i = \left(\frac{A_i/V_{IV}}{A_{Si}/V_S}\right) \cdot C_{si} \cdot v_1 \cdot MW_1 \qquad (4.1)$$

5. Results and Discussion

5.1. Biochanin A in Liquid Solvents

This section presents the solubility data obtained for the solid + liquid systems: biochanin A + Ethanol and biochanin A + 2-Propanol. Table 5.1 reports the solubility as a function of temperature at a constant pressure of 1 atm, along with the standard deviation of the data. The increase in solubility with temperature is expected for a crystalline solid in organic solvents.

Table 5.1. Experimental molar fraction of Biochanin A (2) solubility in ethanol (3) and 2-Propanol(4) as a function of system temperature from 35°C to 60° at 1 atm.

		Ethanol		2-Propanol	
p / atm	T / K	x_2 / mol·mol^{-1}	σ_2 / mol·mol^{-1}	x_2 / mol·mol^{-1}	σ_2 / mol·mol^{-1}
1.00	308.15	0.00246	$6.17 \cdot 10^{-6}$	0.00250	$1.42 \cdot 10^{-5}$
	313.15	0.00287	$7.82 \cdot 10^{-6}$	0.00265	$1.60 \cdot 10^{-5}$
	318.15	0.00336	$2.07 \cdot 10^{-5}$	0.00308	$3.59 \cdot 10^{-6}$
	323.15	0.00403	$2.89 \cdot 10^{-5}$	0.00375	$5.31 \cdot 10^{-5}$
	328.15	0.00545	$4.67 \cdot 10^{-5}$	0.00501	$4.39 \cdot 10^{-6}$
	333.15	0.00653	$2.79 \cdot 10^{-5}$	0.00605	$3.21 \cdot 10^{-5}$

5.2. Biochanin A in Supercritical Carbon Dioxide

This section presents the experimental solubility data obtained in this work for the fluid + solid system: CO_2 + Biochanin A, that was validated with the estimation of uncertainties and the evaluation of the thermodynamic consistency and self-consistency of the data. First, the experimental results for both systems, with their corresponding uncertainties, are presented, followed by the thermodynamic consistency and self-consistency test results.

5.2.1. Solubility in Supercritical Carbon Dioxide

Isothermal solubility for the system (CO_2 + biochanin A) at temperatures of 313, 323 and 333 K as a function of pressure are reported in Table 5.2 and presented graphically in Figure 5.1. The estimation of the standard and combined expanded uncertainties was conducted using the information gathered from the experimental setup, the established methodology, and the recorded measurements. The outcomes of this estimation are compiled in Table 5.2, which includes data for temperature, pressure, and the individual mole fraction measurements. Details regarding the uncertainty estimation methodology for all variables and properties of biochanin A in SC-CO_2 are provided in Table 5.3.

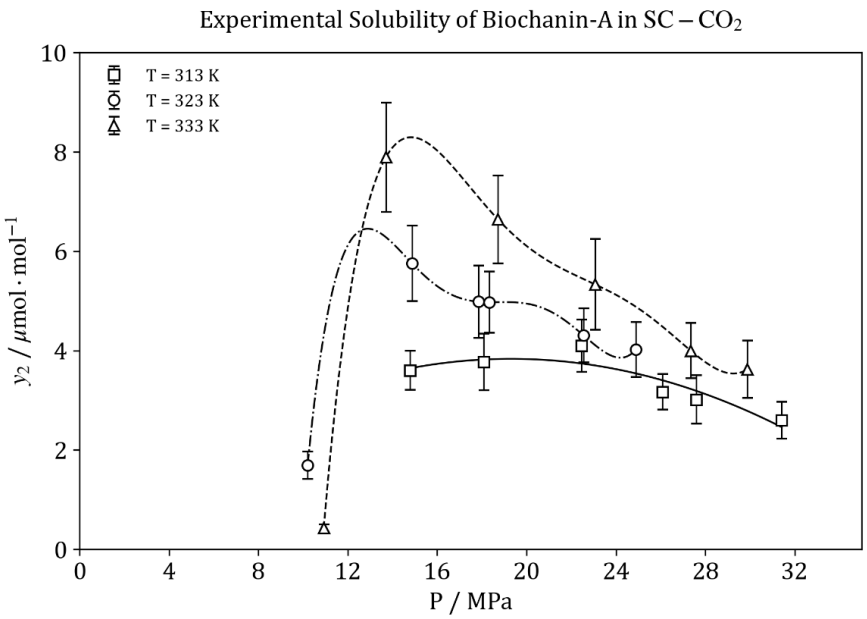

Figure 5.1. Molar fraction of biochanin A (2) (solubility, y_2) in supercritical CO_2 (1)-rich phase as a function of system pressure (p) at temperatures 313 K (□, —), 323 K (○, —·—) and 333 K (△, ——) K. Error bars represent the uncertainties informed in Table 5.2.

Results indicate that solubility started from y_2 = 0.430 μmol·mol^{-1} at T = 333.15 K and p = 10.922 MPa and increased up to y_2 = 7.89 μmol·mol^{-1} at T = 333.15 K and p = 13.702 MPa. As depicted in Figure 5.1, the solubility profiles exhibit an anomalous behavior. Typically, isothermal solubility in supercritical fluids increases monotonically with pressure due to the continuous rise in solvent density. In contrast, this system shows a sharp initial growth followed by a pronounced and unexpected decline, displaying a distinct solubility maximum around the 14.0–16.0 MPa range for all studied isotherms. Additionally, a temperature crossover region is observed at lower pressures, particularly between the 313.15 K and 323.15 K isotherms.

Given the highly unconventional nature of this non-monotonic trend, a series of rigorous methodological verification steps were implemented to systematically eliminate potential sources of experimental error. First, to ensure strict thermodynamic equilibrium, the system equilibration time was significantly extended from the standard 4 hours to 48 hours. Second, the interval between consecutive sampling injections at a fixed pressure was increased from the standard 30-minute HPLC runtime to a full hour to rule out transient concentration gradients within the cell. Third, to prevent carryover or accumulation effects, the equilibrium cell was thoroughly washed, and blank supercritical CO_2 injections were performed to verify that the system was completely solute-free prior to reloading. Lastly, external lines and connections located outside the temperature-controlled cell, which were susceptible to ambient

temperature drops, were thermally insulated to prevent premature solute precipitation during sampling.

Table 5.2. Experimental molar fraction of biochanin A (2) solubility (y_2) in supercritical CO_2 (1)-rich phase as a function of system pressure (p) or density of pure CO_2 (ρ_1) at temperatures (T) of (313, 323 and 333) K.

T / K	p / MPa	ρ_1 / kg m^{-3}	$y_2 \cdot 10^6$ / mol·mol^{-1}	$U_{comb}(y_2) \cdot 10^6$ / mol·mol^{-1}
313	14.781	776.25	3.604	0.391
	18.082	819.48	3.775	0.568
	22.446	860.39	4.099	0.529
	26.086	886.10	3.172	0.358
	27.594	895.20	3.017	0.487
	31.417	916.73	2.597	0.371
323	10.202	408.01	1.691	0.275
	14.876	694.11	5.756	0.761
	17.846	753.29	4.985	0.733
	18.323	761.08	4.975	0.620
	22.553	811.38	4.306	0.541
	24.892	832.43	4.023	0.556
333	10.922	349.45	0.430	0.073
	13.702	543.63	7.893	1.102
	18.719	700.39	6.643	0.886
	23.062	764.23	5.335	0.915
	27.345	806.86	4.000	0.556
	29.884	828.23	3.628	0.578

$u(T)$ = 0.1 K, $u(p)$ = 0.001 MPa. Combined expanded uncertainties for molar fraction of biochanin, $U_{comb}(y_2)$, were estimated with a 0.90 level of confidence.

Furthermore, while the experimental measurements exhibit relatively large combined expanded uncertainties, the non-monotonic trend remains statistically robust. An analysis of the uncertainty boundaries reveals that the lower limits of the data points at the solubility peaks do not overlap with the upper limits of the measurements recorded at high pressures. Together, the high reproducibility of the measurements across the modified protocols and the statistical separation of the error bars confirmed that the observed solubility drop is an intrinsic thermodynamic phenomenon rather than an experimental artifact or measurement noise.

Table 5.3. Estimation of the combined expanded uncertainty for molar fraction of biochanin A (2) (y_2) in supercritical CO_2 (1)-rich phase, $U_{Comb}(y_2)$, based on the contributions of properties and variables measured and calculated [126].

Property, Variable	Type of Uncertainty (Level of confidence / %)	Uncertainty	Contribution to $U_{comb}(y_2)$ / %
Temperature (313 ≤ T ≤ 333) K	Standard	u(T) = 0.1 K	-
Pressure (10.202 ≤ p ≤31.417) MPa	Standard	u(p) = 0.01 MPa	-
Chromatographic Area for sample of Biochanin A dissolved in CO_2 (218323 ≤ A_2 ≤ 6936099) AU	Standard	u(A_2) = 3500 AU	1
Chromatographic area for stock solution (11701948 ≤ A_{S2} ≤ 13519213) AU	Standard	u(A_{S2}) = 3500 AU	12
Volume of sampler loop of the equilibrium cell (V_{IV} = 20 µL)	Standard	u(V_{IV}) = 2 µL	13
Volume loop of the HPLC injector (VS = 20 µL)	Standard	u(V_S) = 2 µL	13
Concentration of stock solution $C_{S2}=\frac{m_2}{V_{IV}\cdot MW_2}$ C_{S2} = 0.183 mol·cm^{-3}	Combined	$\frac{u_{comb}(C_{S2})}{C_{S2}}=\frac{u(m_2)}{m_2}+\frac{u(V_{VF})}{V_{VF}}$	60
Mass of biochanin A dissolved in methanol m_2 = 0,052 g	Standard	u(m_2) = 0.0001 g	-
Volume of flask to dissolve Biochanin A in methanol V_{VF} = 50 cm^3	Standard	u(V_{VF}) = 0.08 cm^3	-
Specific volume of CO_2 V_1 = f(T,p) (4.80 ≤ V_1 ≤ 12.59) x10^{-5} m^3·mol^{-1}	Combined	$\frac{u_{comb}(V_1)}{V_1}=\frac{1}{V_1}\cdot\left\lvert\frac{\partial V_1}{\partial T}\right\rvert\cdot u(T)+\left\lvert\frac{1}{V_1}\cdot\frac{\partial V_1}{\partial p}\right\rvert\cdot u(p)$	1
Volumetric expansibility of CO_2 $\alpha_1=\left\lvert\frac{1}{V_1}\cdot\frac{\partial V_1}{\partial T}\right\rvert$ (0.0041075 ≤ α1 ≤ 0.0440610) K^{-1}	-	NIST	-
Isothermal compressibility of CO_2 $\beta_1=\left\lvert\frac{1}{V_1}\cdot\frac{\partial V_1}{\partial p}\right\rvert$ (0.0056513 ≤ β1 ≤ 3005400) MPa^{-1}	-	NIST	-
Molar fraction of Biochanin A in CO_2-rich phase $y_2=\left(\frac{A_2/V_{IV}}{A_{S2}/V_S}\right)\cdot C_{S2}\cdot V_1\cdot MW_1$ (0.430 ≤ y2 ≤ 7.893)·10^{-6} molmol^{-1}	Combined expanded	$\frac{U_{comb}(y_2)}{1.645\cdot y_2}=\frac{\Delta A_2}{A_2}+\frac{\Delta A_{S2}}{A_{S2}}+\frac{\Delta V_{IV}}{V_{IV}}+\frac{\Delta V_S}{V_S}+\frac{\Delta C_{S2}}{C_{S2}}+\frac{\Delta V_1}{V_1}$	-

The non-monotonic solubility profile observed across all three isotherms is consistent with a progressive shift in the dominant intermolecular interactions as pressure increases. At lower pressures (below ~14–16 MPa), the rapid rise in SC-CO_2 density enhances its solvating power, driving an increase in the dissolved molar fraction of biochanin A. Beyond this threshold, however, the trend reverse sharply. It is hypothesized that the reduction in free volume at elevated pressures brings solute molecules into closer proximity, likely creating conditions favorable for hydrogen bonding via the unhindered hydroxyl group at position 7. The

consequent formation of associated species — possessing larger effective molecular mass and lower volatility than the free monomer — might diminish the affinity of biochanin A for the supercritical fluid phase, producing the observed solubility decline. Notably, the solubility maximum shifts from approximately 16.0 MPa at 313.15 K to approximately 14.0 MPa at 333.15 K (Table 5.2), suggest that higher temperatures might require less compression to overcome the entropic penalty of association, which would align with the endothermic nature of hydrogen bond disruption. The potential nature and stoichiometry of these hypothesized associated species are further examined in Section 5.4, where structural evidence from the chromatographic profiles and thermodynamic modeling are presented.

5.2.2. Characterization of the Structure of Biochanin A

To confirm the chemical stability and structural integrity of the solute during the high-pressure experiments, Nuclear Magnetic Resonance (NMR) analyses were conducted on the biochanin A samples both before and after exposure to the supercritical equilibrium phase. The resulting NMR spectrum (Figure 5.2) showed no structural alterations, shifts, or degradation products, verifying that the solid phase remained unequivocally as biochanin A throughout the process. This structural preservation is crucial for the thermodynamic interpretation of the system. It demonstrates that the stabilization or reduction in molar solubility observed at elevated pressures (as shown in Figure 5.1) is driven exclusively by physical phenomena—such as density-dependent solute self-association and reversible dimerization—rather than any chemical transformation or decomposition of the monomeric species.

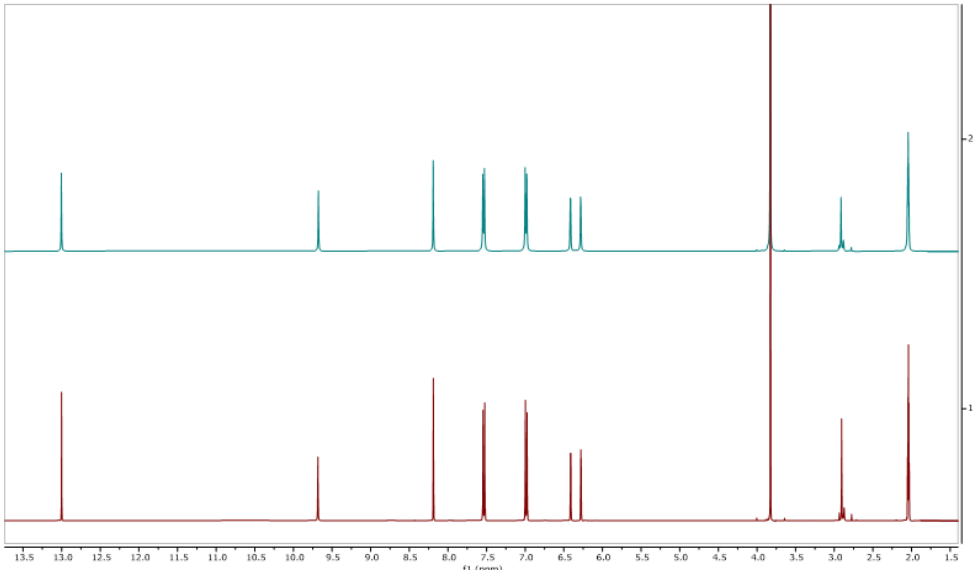

Figure 5.2. Biochanin A NMR spectrum before (top) and after (bottom) undergoing equilibrium with SC-CO_2.

5.3. Data Validation

Upon completion of the experimental measurements, the semi-empirical model proposed by Mendez-Santiago and Teja (MS-T) was fitted to the solubility data for biochanin A using Equation (5.1). This regression resulted in an Average Absolute Relative Deviation (AARD) of 33.30% for the set of measurements. These deviations are attributed to the inherent mathematical constraints of the MS-T model, as detailed in Section 3.3.3. The self-consistency results are graphically represented in Figure 5.3, following the linear expressions:

$$T[\ln(y_i p) - 18.04] = -5673.77 + 1.63 \cdot \rho_1 \quad (5.1)$$

As illustrated in the plot, most of the data points for biochanin A exhibit a strong linear trend, particularly at solvent densities exceeding 600 kg·m^{-3}. This alignment across different isotherms suggests that the high-pressure measurements are mutually consistent and follow the fundamental thermodynamic behavior expected in supercritical systems. However, the data analysis revealed that 2 out of 18 experimental points for biochanin A did not conform to the expected linear trend. Since these points could not be validated for self-consistency, they were excluded from the final model regression.

Figure 5.3. Representation of $\boldsymbol{y_i}$, $\boldsymbol{\rho_1}$ and T in a two-dimensional array: $\boldsymbol{T}\cdot[\boldsymbol{ln}(\boldsymbol{y_i}\cdot\boldsymbol{p})-\boldsymbol{C_i}]$ versus $\boldsymbol{\rho_1}$(T,p). The symbols represent the experimental data of biochanin A (2) at 313 K (□), 323 K (○) and 333 K (△).

As highlighted by Mendez-Santiago and Teja [101], Equation (3.7) exhibits limitations under low-density conditions. Consequently, solubility data points with ρ_1 values below 550 kg·m^{-3} may require alternative correlations to overcome the predictive deficiencies of the model and

verify their consistency. Nevertheless, accurately representing the pressure and temperature behavior of pure substances near the critical point is already a complex task [129]; this difficulty is significantly amplified in mixtures, even when the solute is highly dilute. Furthermore, the scatter observed may indicate higher experimental uncertainty at elevated temperatures or the onset of more pronounced dimerization effects that the linear MST model cannot fully capture.

The thermodynamic consistency test [97] utilized the solubility results modeled with the SAFT-VR Mie equation of state (detailed in Section 3.4.3) to calculate the absolute area deviations (ΔA_{1i}), which are necessary to evaluate the thermodynamic integrity of each isotherm. These results are summarized in Table 5.4.

Table 5.4. Thermodynamic consistency test results for the equilibrium CO_2 (1) + Biochanin A (2).

j	p / MPa	$\delta(y_i)_j$ / %	(ΔA_{1i}) / %	p / MPa	$\delta(y_i)_j$ / %	(ΔA_{1i}) / %	p / MPa	$\delta(y_i)_j$ / %	(ΔA_{1i}) / %
	T = 313 K			T = 323 K			T = 333 K		
Biochaninin-A									
1	14.78	44.9%	0.29%	10.20	99.6%	6.71%	10.92	-96.6%	5.45%
2	18.08	-2.8%	0.81%	14.88	81.1%	5.74%	13.70	-96.8%	7.50%
3	22.45	-65.3%	2.35%	17.85	38.8%	1.01%	18.72	43.9%	2.59%
4	26.09	-198.1%	2.39%	18.32	31.1%	1.36%	23.06	-92.7%	5.82%
5	27.59	-253.0%	1.76%	22.55	-70.4%	2.25%	27.35	-376.4%	3.60%
6	31.42	-430.7%	1.74%	24.89	-144.9%	0.50%	29.88	-592.2%	0.71%

[a] $\delta(y_i)_j = \left(y_i^{calc} - y_i\right)_j / y_{i,j}$: Individual relative deviations (j) between the calculated ($y_{i,j}^{calc}$) and measured ($y_{i,j}$) values of the solute solubility (i).

[b] $(\Delta A_{1i})_j$: Fraction of individual area deviation (j).

The ΔA_{1i} values for all experimental data points were found to be below 7.498%, suggesting a generally high level of consistency. However, it was observed that in 17 out of 18 solubility measurements for biochanin A, the absolute relative deviations ($|\delta(y_i)|$) exceeded the 20% threshold, indicating that thermodynamic consistency could not be verified in those specific instances.

The apparent contradiction between the low area deviations (all ΔA_{1i} < 7.5%) and the high individual relative deviations ($|\delta(y_i)|$ > 20% in 17 out of 18 data points) warrants careful interpretation. The thermodynamic consistency framework proposed by Valderrama and Zavaleta [97] is built upon two sequential requirements: first, that the selected equation of state adequately describes the solubility isotherms within ±20% RRMSD (Stage 1); and second, that the Gibbs-Duhem integral deviations fall within acceptable limits (Stage 2). The Stage 1 criterion presupposes that the reference EoS is capable of representing the essential physics of

the system under evaluation. In the present case, however, the experimental solubility profile is non-monotonic — a behavior that a standard monomeric equation of state is structurally unable to capture. This limitation is not a property of the data, but a consequence of the thermodynamic phenomenon driving the system: the formation of associated species in the supercritical phase, proposed in Section 5.2.1 and evidenced by the emergence of secondary chromatographic signals at elevated pressures (Tables 5.9–5.11).

When the Stage 1 criterion cannot be met because the reference model is inadequate for the system, the large $\delta(y_i)$ values produced in Stage 2 are an artifact of the model's failure, not an indicator of data quality. This interpretation is supported by the low area deviations (ΔA_{1i}), which confirm that the integral form of the Gibbs-Duhem equation is satisfied locally between consecutive data points along each isotherm, demonstrating internal coherence of the measurements.

Taken together, the low procedural uncertainties, the high measurement repeatability (>95%), the strong linear trend in the MS-T self-consistency plot at densities above 600 kg·m^{-3}, and the physically coherent behavior of the data across all three isotherms provide robust evidence that the experimental measurements are reliable, even in the absence of formal thermodynamic consistency verification under a monomeric framework.

5.4. Solubility Modeling

5.4.1. SAFT-VR Mie Equation of State

The SAFT-VR Mie EoS was employed to correlate the experimental solubility isotherms of biochanin A in supercritical carbon dioxide. The application of this framework required the prior determination of the molecular and association parameters for biochanin A. These parameters were fitted through the regression of experimental solubility data obtained from biochanin A + ethanol and biochanin A + 2-propanol systems. Consequently, the pure-component parameters for the selected alcohols were independently fitted using available literature vapor pressure data. The source code utilized for these regression routines is detailed in Appendices A and C.

The molecular and self-association parameters for ethanol and 2-Propanol, namely the segment number (m), segment diameter (σ), dispersion energy (ε_{assoc}/k_B), Mie repulsive exponent (λ_r), association energy ($\varepsilon^{AB}_{assoc}/k_B$) and bonding volume ($\kappa^{AB}_{assoc}$), were fitted simultaneously using experimental vapor pressure data from Ambrose & Sprake [130]. A 2B association scheme was used for the fit of both solvents, yielding low deviations with an AARD of 1.497% for ethanol and 0.317% for 2-propanol. The model fit is shown in Figure 5.4.

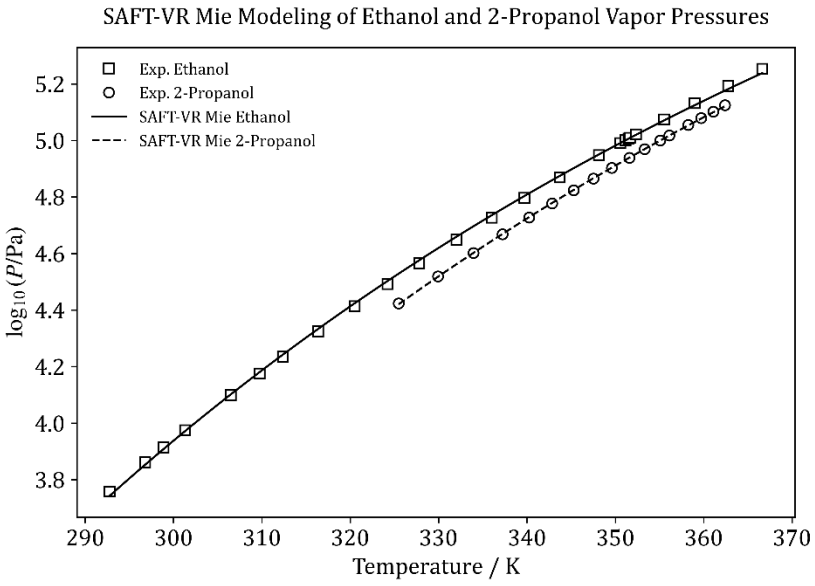

Figure 5.4. Vapor pressure (log10(P/Pa)) as a function of temperature (T / K) for ethanol and 2-propanol. Experimental data obtained from Ambrose & Sprake [130].

The molecular and self-association parameters for biochanin A—m, σ,ε/k_B, λ_r, ε^{AB}/k_B and κ^{AB}—were fitted using experimental solid-liquid equilibrium (SLE) solubility data from the

binary systems biochanin A + ethanol and biochanin A + 2-propanol across a temperature range from 308.15 K to 333.15 K at atmospheric pressure.

Two association schemes were considered for the parameter fit of biochanin A, 2B and 4C, the fitted parameters for each scheme are presented in Table 5.5. The 4C association scheme was selected over the 2B scheme to model biochanin A because its optimized SAFT-VR Mie parameters are more consistent with the physical and chemical nature of the molecule. This is consistent with the presence of two hydroxyl groups on the molecule (see Figure 1.3), presenting 2 donor and 2 acceptor sites.

The 4C scheme yields a softer repulsive exponent, whereas the 2B scheme results in an unusually steep repulsion that is less representative of complex organic fluids. Furthermore, the association volume obtained with the 4C scheme provides a much more reasonable spatial range for hydrogen-bonding interactions compared to the excessively small, non-physical value derived from the 2B scheme. Combined with a more realistic association energy and chain length, the 4C scheme accurately captures the multi-site associative behavior and steric complexity of the biochanin A molecule without relying on artificial parameter values.

Table 5.5. Molecular and association parameters obtained for Biochanin A (2) with association schemes 2B and 4C.

Association Scheme	m / -	σ / Å	ε/k_B / K	λ_r / -	ε^{AB}/k_B / K	κ^{AB} / Å^3
2B	9.5268	2.5414	213.141	23.2819	3620.63	0.01290
4C	14.113	2.5199	144.045	10.9082	2644.29	0.31813

The 2B association scheme regression resulted in an AARD of 6.15% for ethanol and 11.60% for 2-propanol, and a combined AARD of 8.88%. The 4C association scheme regression resulted in an AARD of 3.66% in ethanol and 5.40% in 2-propanol, culminating in a total combined AARD of 4.53%. The experimental data and deviation for each point is reported in Appendix B. The quality of the 4C fit is visually demonstrated in Figure 5.5. The optimized parameters for both the liquid solvents and the solid solute are summarized in Table 5.6.

Table 5.6. SAFT-VR Mie equation of state parameters for CO_2 (1), biochanin A (2), ethanol (3) and 2-Propanol (4), determined using the Coarse Granulation (CG) method by Mejía et al. [112] and fitted to experimental data.

i	Compound	m / -	σ / Å	ε/k_B / K	λ_r / -	λ_a / -	ε^{AB}/k_B / K	κ^{AB} / Å^3
1	CO_2	2.000	2.8363	195.396	14.6989	6	-	-
2	Biochanin A	14.113	2.5199	144.045	10.9082	6	2644.285	0.31813
3	Ethanol	1.940	3.2098	247.245	8.0632	6	2725.085	0.97871
4	2-Propanol	1.964	3.2831	241.172	8.0713	6	3071.149	0.68899

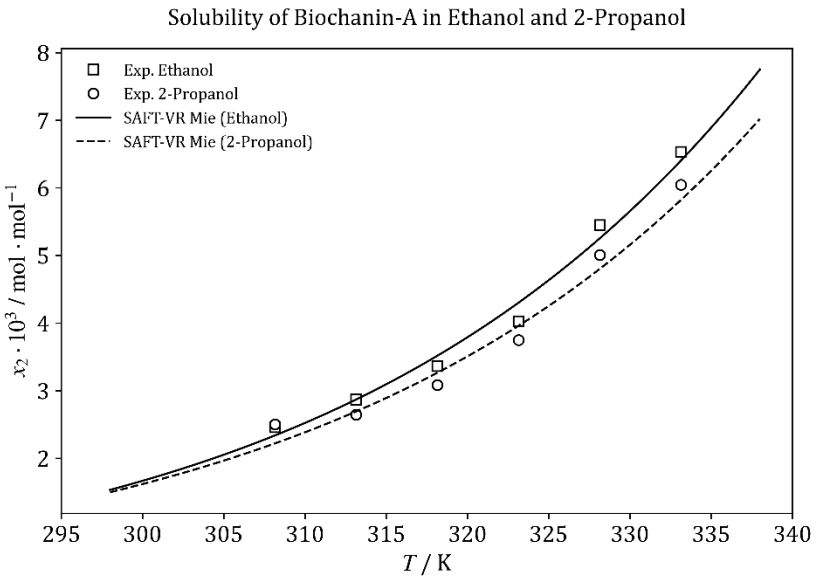

Figure 5.5. Solubility ($x_2 \cdot 10^3$ / mol·mol^{-1}) of biochanin A in ethanol and 2-propanol as a function of temperature (308.15 to 333.15 K) at 1 atm.

Once the pure fluid and solute parameters were established, the cross-interaction parameter (k_{12}) for the binary CO_2+ biochanin A system was optimized against the high-pressure solubility measurements obtained in this work. To accurately reflect thermal dependencies over the operational range, k_{12} was regressed as a temperature-dependent function, as defined in Equation (5.2). The code used for the regression of parameters A and B is available in Appendix D.

$$k_{12} = A + B \cdot (1/T - 1/313.15) \quad (5.2)$$

The regressed parameters for Equation (5.2) along with their corresponding deviations are reported in Table 5.7. The application of this single temperature-dependent binary interaction parameter yielded an overall modeling AARD of 160.37% for the biochanin A solubility, with individual isothermal deviations reaching up to 592.24% at 333.15 K. As visually illustrated in Figure 5.6, the SAFT-VR Mie framework fails to capture the qualitative phase behavior of the system. While the model predicts a continuous, monotonic increase in solubility driven by the rising density and solvating power of supercritical CO_2, the experimental data reveals a prominent solubility maximum between 14 and 18 MPa, followed by a non-monotonic decline at higher pressures.

Phenomenologically, the discrepancy becomes critical at higher pressures. While the theoretical model predicts a continuous, exponential increase in solubility driven by solvent density, the experimental data exhibits an anomalous behavior: the solubility plateaus or even slightly

decreases at pressures above 20 MPa. The model, even when utilizing temperature-dependent binary interaction parameters (k_{12}), is inherently incapable of reproducing this inflection.

Table 5.7. Regressed parameters for the temperature-dependent binary interaction function, discrete k_{12} values, and corresponding average absolute relative deviations (AARD%) for the CO_2 (1) + biochanin A (2) system.

i	Compound	A / -	B / K	AARD [a] / %
2	Biochanin A	-0.687627	236.12	160.37
T, K		k_{12}, -		AARD [a] / %
313.15		-0.13606		165.8%
323.15		-0.14561		77.6%
333.15		-0.15459		276.3%

[a] AARD = $(100/N) \cdot \sum_{j=1}^{N} \left(y_i^{model} - y_i^{exp}\right)_j / \left(y_i^{exp}\right)_j$

This severe discrepancy can be fundamentally justified by the underestimation of the phenomenon of solute self-association. As previously hypothesized in Section 1.1 and Section 5.1.1, the molecular structure of biochanin A features hydroxyl groups at positions 5 and 7, rendering it highly susceptible to hydrogen bonding. At elevated pressures (> 18 MPa), the reduction in free volume brings solute molecules closer together, shifting the equilibrium toward the formation of reversible dimers. Dimer formation would drastically increase the effective molecular volume and reduce the apparent vapor pressure of the solute, phenomena that would counteract the solvating power of the highly compressed supercritical CO_2.

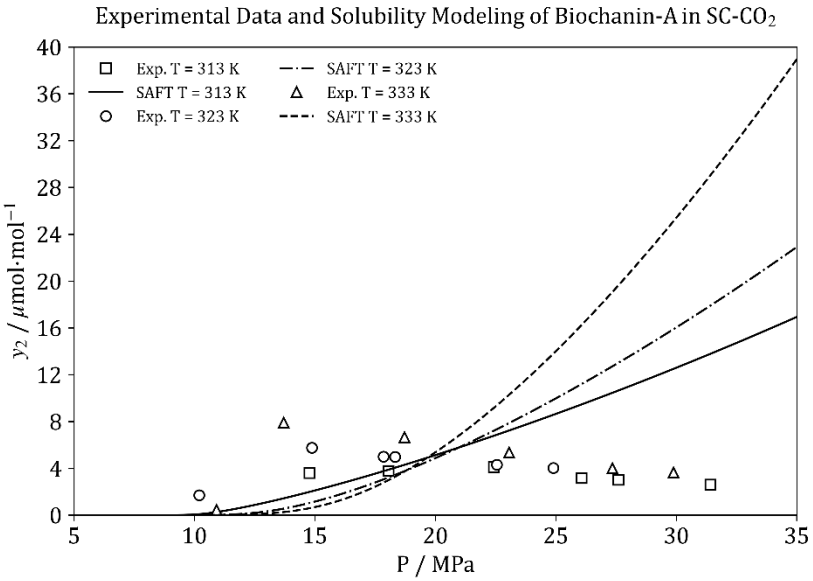

Figure 5.6. Modelling of the isothermal solubility of biochanin A (2) in supercritical CO_2 (1) as a function of system pressure at 313 K (□, —), 323.15 K (○, —·—), and 333.15 K (△, ——). Lines represent the isotherms calculated by means of the SAFT-VR Mie.

Although the SAFT framework inherently accounts for molecular self-association, the model struggles to capture the non-monotonic solubility behavior or high-pressure inflections often observed in these systems. This limitation primarily stems from two intrinsic simplifications within the first-order Wertheim perturbation theory (TPT1) mapped onto the SAFT-VR Mie EoS. First, the local density at the bonding site is approximated using the radial distribution function of a non-associating reference fluid. This approximation fails in highly compressible, high-pressure regimes where density fluctuations drastically alter the local molecular packing around active sites [131]. Second, TPT1 strictly prohibits the formation of closed cyclic structures and intramolecular bonding. For multifunctional molecules with complex spatial architectures, such as biochanin A, the competitive equilibrium between intramolecular shielding and the formation of highly stable, cooperative cyclic dimers represents a dominant thermodynamic driver [132]. By forcing association into purely open, linear oligomers, the model imposes a topological constraint that underestimates the true aggregation state of the solute, thereby missing the macroscopic solubility inflections driven by localized molecular clustering.

To quantitatively assess the magnitude of this underestimation and isolate the physical impact of aggregation, a phenomenological boundary-case analysis was conducted. By forcing the equation of state to evaluate a hypothetical fully-associated state (pure dimer), it becomes possible to map the theoretical limits of the system's phase behavior. The phase behavior of a hypothetical pure dimer form of biochanin A was modeled with SAFT-VR Mie EoS. The EoS was employed to model solubility isotherms at 313.15, 323.15 and 333.15 K. The sublimation pressure of the dimer was estimated using the Grain–Watson method [118] while its molecular parameters were extrapolated from those of the monomer.

The transfer of SAFT-VR Mie parameters from the biochanin A monomer to its dimeric form is based on the segment identity principle inherent to the SAFT framework. Assuming that the dimer is composed of the same fundamental chemical segments as the monomer, the interactions associated with each segment are considered invariant. Consequently, the segment diameter, the segment dispersion energy, and the repulsive exponent were kept constant. The increase in molecular size was accounted for by doubling the chain length parameter and molecular weight, thereby reflecting the structural duplication of the molecule.

For the dimeric species, all association parameters were set to zero. This assumption considers that the self-association sites responsible for dimer formation become fully saturated upon

aggregation, leaving no available sites for additional hydrogen bonding or association interactions. In addition, the binary interaction parameter, (k_{ij}), was set to zero due to the lack of experimental data required for its estimation. This approach isolates the effects of dispersion and repulsion arising from the extended molecular chain while avoiding the introduction of unverified association and interaction parameters. The set of parameters employed in the calculations is presented in Table 5.8.

Table 5.8. SAFT-VR Mie molecular parameters of Biochanin A dimer species.

Compound	m / -	σ / Å	ε/k_B / K	λ_r / -	ε^{AB}/k_B/ K	κ^{AB} / Å^3
Biochanin A (Dimer)	28.226	2.5199	166.89	12.619	-	-

As shown in Figure 5.7 the monomer model predicts solubility values approximately two to three orders of magnitude higher than the non-associating dimer model across the entire pressure range. Both models successfully capture the characteristic crossover pressure region between 15 MPa and 20 MPa. However, the non-associating dimer model severely underpredicts the experimental data. This underestimation is a direct consequence of the strictly predictive approach—extrapolating parameters and setting $k_{ij} = 0$ fails to account for the necessary dispersive cross-interactions between the solvent and the extended dimeric structure.

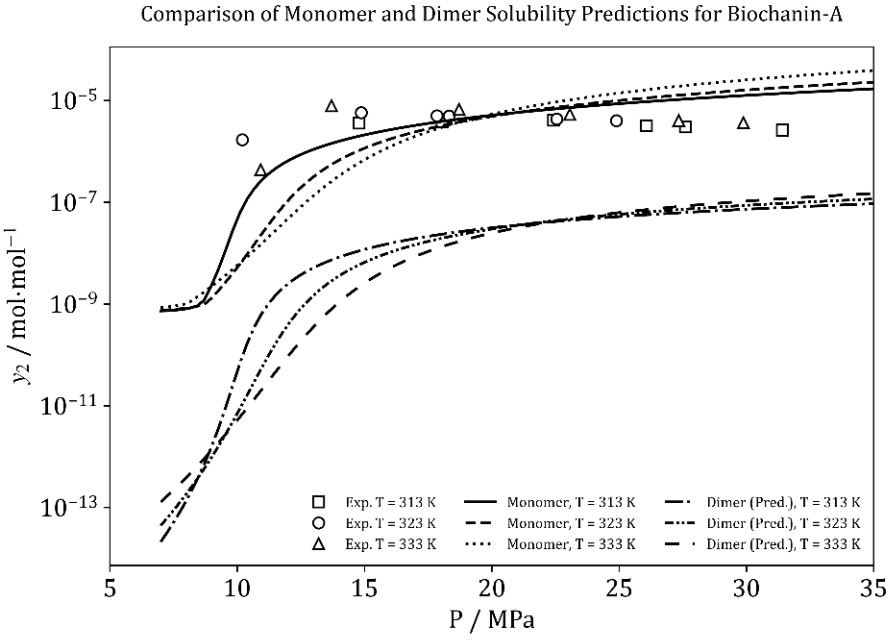

Figure 5.7. Molar fraction of biochanin A (2) monomer and dimer form in supercritical CO_2 (1)-rich phase as a function of system pressure (p) at temperatures 313 K (□), 323 K (○) and 333 K (△) K. Lines represent SAFT-VR Mie modelling.

Ultimately, while evaluating the dimer as an isolated entity is quantitatively inaccurate, the systematic high-pressure deviations in the baseline model indicate that the standard SAFT-VR Mie association framework does not capture the full physical extent of molecular aggregation. The forced dimeric prediction was modeled to phenomenologically demonstrate the severe thermodynamic impact of an increased effective volume and reduced solute volatility upon association. Furthermore, the inability of the model to capture the experimental decrease may not rely solely on the underestimation of the association fraction. It is critical to consider the influence of highly the solid sublimation pressure. Since the vapor pressure of biochanin A was estimated utilizing predictive correlations rather than direct experimental measurements, any inherent deviations in these estimated properties could significantly propagate through the equation of state, further skewing the phase equilibrium calculations at elevated pressures.

Driven by these associative constraints, the overall solubility of biochanin A in pure supercritical CO_2 remains remarkably low, making the utilization of a polar cosolvent a practical necessity to enhance mass transfer rates. To overcome this limitation, the introduction of ethanol was evaluated. For the modeling of the cosolvent system, the previously adjusted parameters for ethanol were employed. The binary interaction parameters between the cosolvent and the solute (k_{23}) and between the cosolvent and CO_2 (k_{13}) were both set to zero.

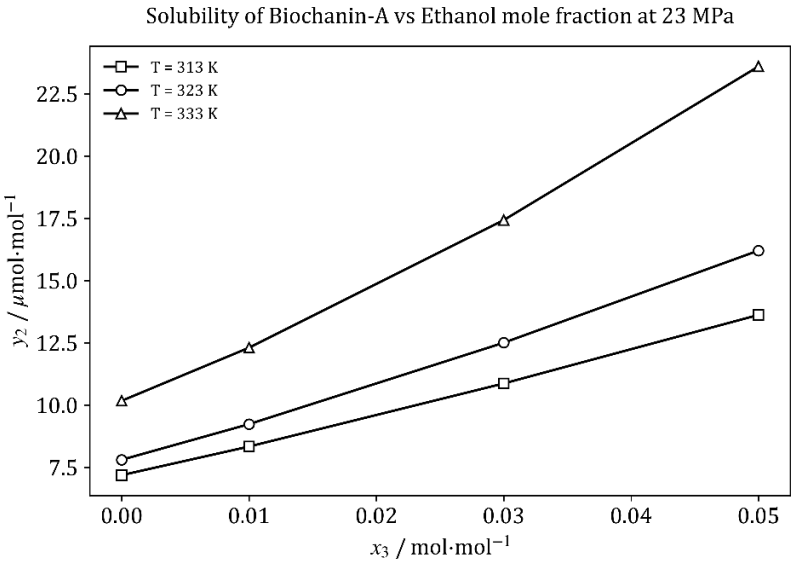

Figure 5.8. SAFT-VR Mie Molar fraction modelling of biochanin A (2) in supercritical CO_2 (1)-rich phase as a function of system ethanol (3) molar fraction at 23 MPa. Temperatures 313 K (□), 323 K (○) and 333 K (△) K.

The results demonstrate that the addition of ethanol significantly enhances the solubility of biochanin A across all investigated conditions. As depicted in Figure 5.8, at a constant pressure of 23 MPa, the solubility increases monotonically with the ethanol mole fraction (x_3). This

enhancement exhibits a synergistic effect with temperature; the solubility difference between the pure supercritical CO_2 system ($x_3 = 0$) and the 5% ethanol mixture is substantially greater at 333 K than at 313 K.

Furthermore, the solubility isotherms at 40°C, 50°C and 60°C (Figures 5.9, 5.10, and 5.11, respectively) illustrate that this beneficial effect persists across the entire pressure range. Increasing the ethanol content systematically shifts the solubility curves upward, indicating that equivalent solubility levels can be attained at lower operational pressures.

From a physicochemical perspective, this behavior is attributed to the higher polarity of ethanol relative to supercritical CO_2. The cosolvent increases the overall polarity of the fluid phase, promoting stronger intermolecular interactions—specifically hydrogen bonding—with the polar functional groups of biochanin A. This specific interaction disrupts potential solute self-association and reduces the affinity mismatch between the solid solute and the solvent phase, thereby maximizing solvent power.

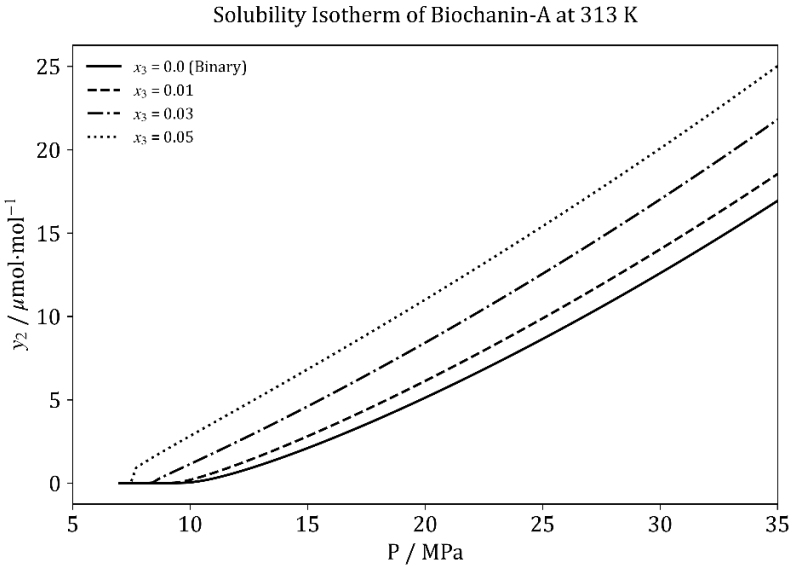

Figure 5.9. SAFT-VR Mie molar fraction modelling of biochanin A (2) in supercritical CO_2 (1)-rich phase as a function of system pressure (p) at 313 K and ethanol (3) molar fraction 0.00 (—), 0.01 (---), 0.03 (— · —) and 0.05 (·····).

This predicted cosolvent effect is highly consistent with the experimental observations reported by Nakada et al. [83] for structurally related isoflavones (daidzein and genistein). Their experimental data demonstrates a comparable, significant increase in solubility for genistein and daidzein upon the addition of ethanol to supercritical CO_2. This agreement supports the hypothesis that polar cosolvents effectively enhance the solvation of polyphenolic compounds

through specific interactions, providing further validation for the model's predictive capability within this chemical class.

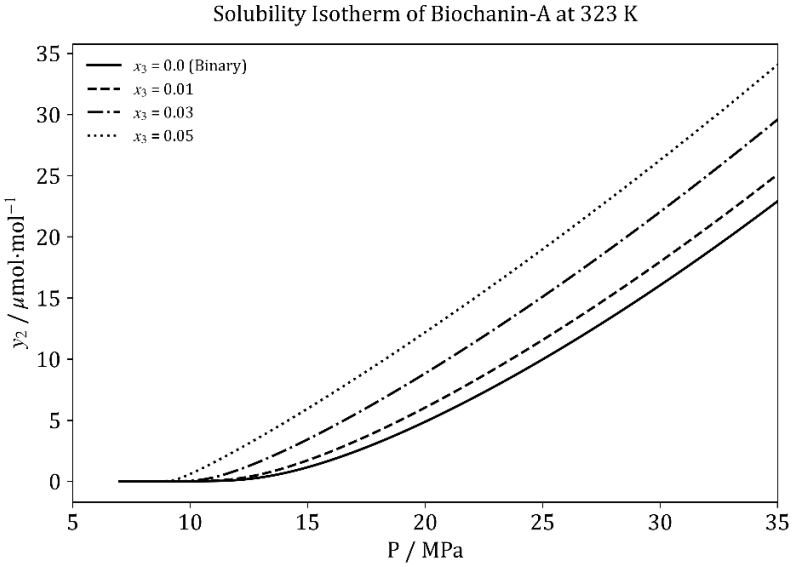

Figure 5.10. SAFT-VR Mie molar fraction modelling of biochanin A (2) in supercritical CO_2 (1)-rich phase as a function of system pressure (p) at 323 K and ethanol (3) molar fraction 0.00 (—), 0.01 (---), 0.03 (— · —) and 0.05 (·····).

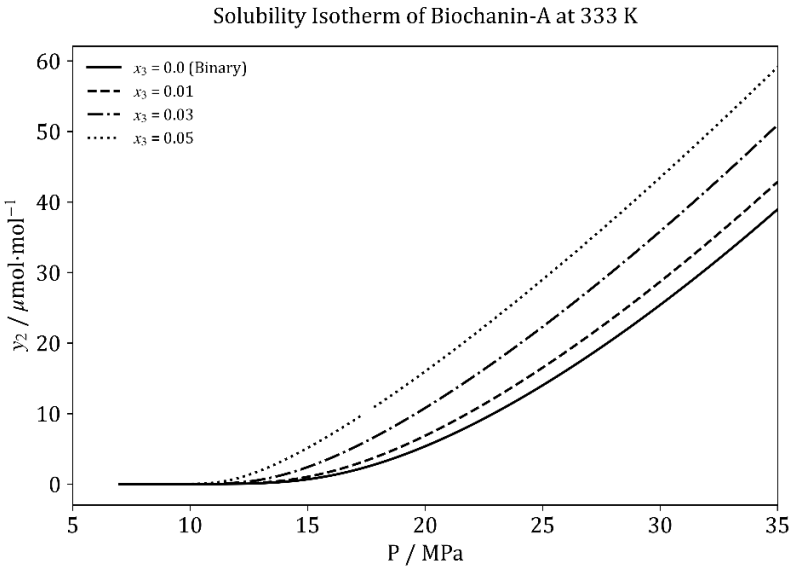

Figure 5.11. SAFT-VR Mie molar fraction modelling of biochanin A (2) in supercritical CO_2 (1)-rich phase as a function of system pressure (p) at 333 K and ethanol (3) molar fraction 0.00 (—), 0.01 (---), 0.03 (— · —) and 0.05 (·····).

5.4.2. Chromatographic Evidence and Molecular Structure Analysis

This subsection presents the experimental chromatographic profiles obtained for the binary CO_2 + biochanin A system, displaying three representative chromatograms for each isotherm evaluated at low, intermediate, and high operational pressures (Tables 5.9, 5.10 and 5.11).

Table 5.9. Evolution of the experimental HPLC chromatographic profiles for the binary CO_2 (1)+ Biochanin A (2) system at 313.15 K under low, intermediate, and high operational pressures.

T / K	p / MPa	HPLC Chromatograms
313.15	10.600	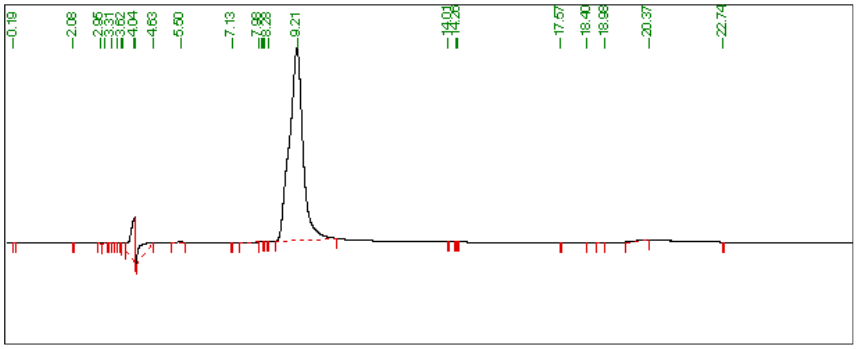
	14.843	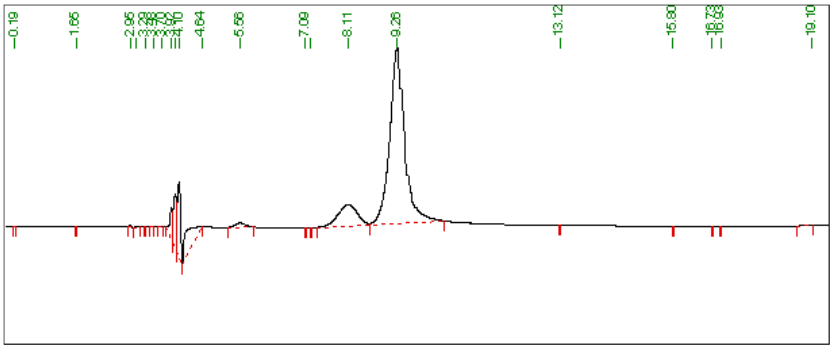
	19.384	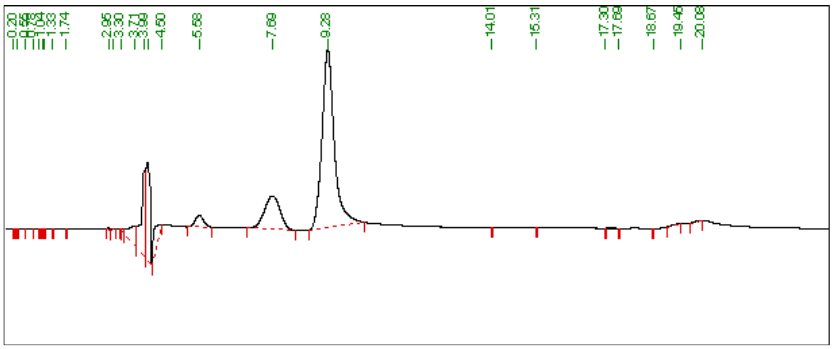

As the operational pressure increases within each isotherm, the peak area corresponding to the biochanin A monomer undergoes a relative decrease compared to the preceding low-pressure conditions. Concurrently, an emergence and gradual growth of secondary and tertiary signals are observed across all evaluated temperatures. This coordinated peak evolution is consistent

with mass conservation during solute self-association. The reduction in macroscopic free volume likely drives a fraction of the monomers to engage in self-association, thereby altering their chromatographic affinity and shifting their elution order.

Table 5.10. Evolution of the experimental HPLC chromatographic profiles for the binary CO_2 (1)+ Biochanin A (2) system at 323.15 K under low, intermediate, and high operational pressures.

T / K	p / MPa	HPLC Chromatograms
323.15	10.193	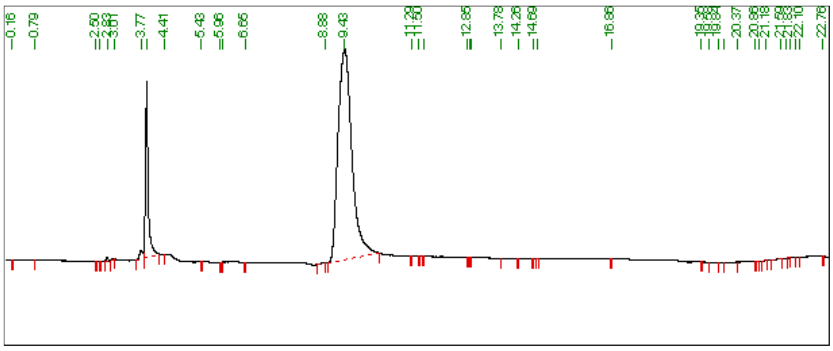
	18.343	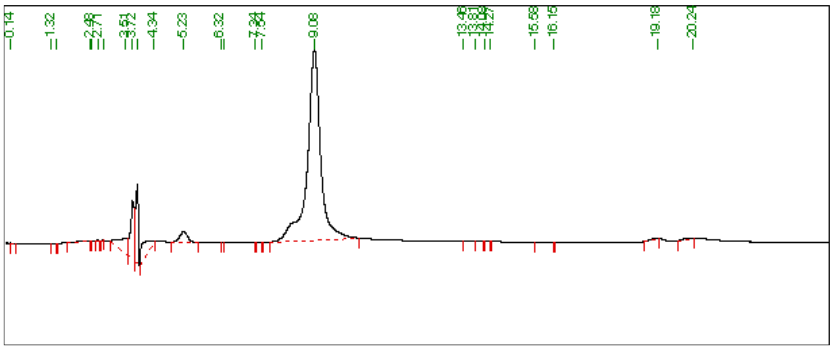
	24.946	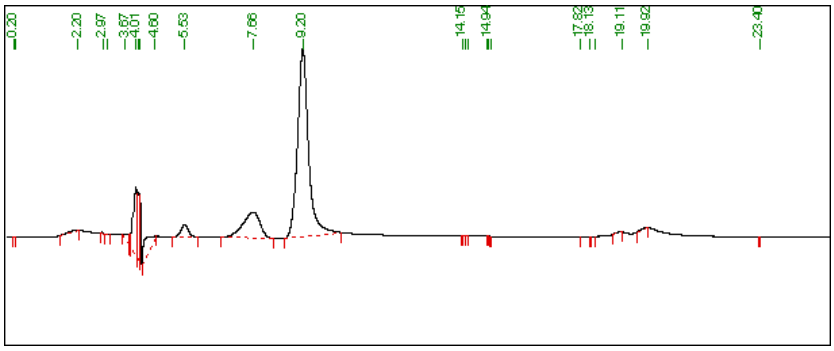

Furthermore, the quantitative magnitude of these additional peaks indicates that this phenomenon represents a significant structural shift rather than a minor trace effect. At a system temperature of 40 °C, the secondary and tertiary signals account for approximately 20% of the main monomer peak area—a relative contribution that systematically increases with

rising temperature, registering 22% at 50 °C and peaking at 25% at 60 °C under the highest-pressure conditions.

Table 5.11. Evolution of the experimental HPLC chromatographic profiles for the binary CO_2 (1)+ Biochanin A (2) system at 333.15 K under low, intermediate, and high operational pressures.

T / K	p / MPa	HPLC Chromatograms
333.15	13.666	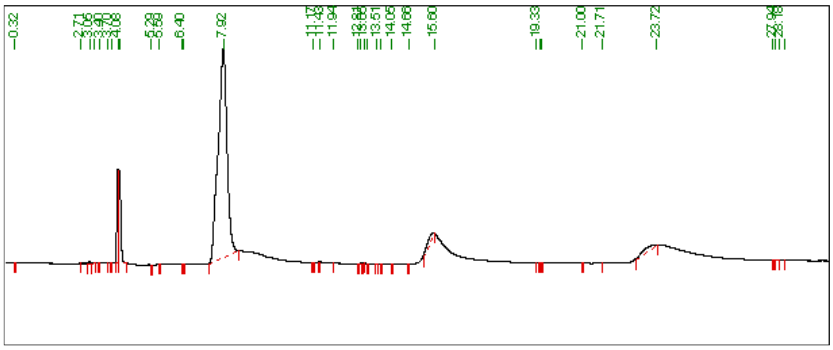
	18.712	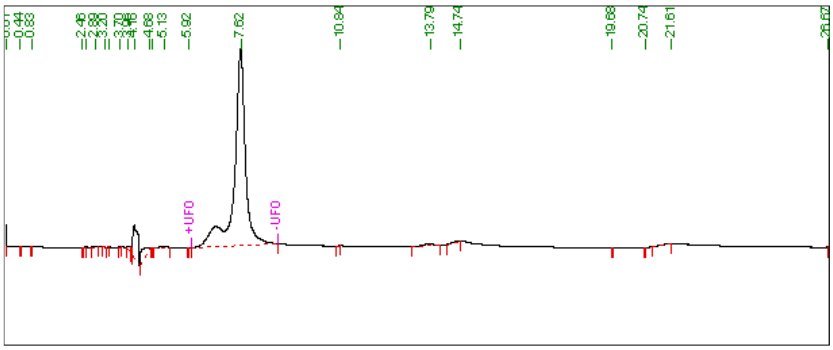
	27.408	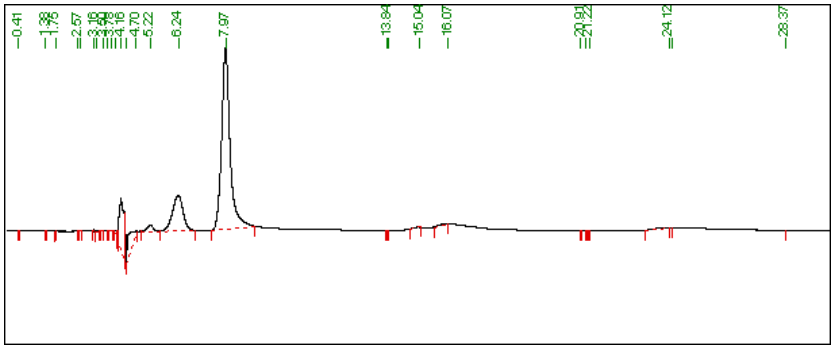

While the chromatographic evidence presented in Tables 5.9–5.11 is strongly consistent with the progressive formation of associated species at elevated pressures, definitive structural characterization of these eluting complexes requires complementary analytical techniques. High-Performance Liquid Chromatography coupled to Mass Spectrometry (HPLC-MS) is the most direct approach: by providing molecular weight information for each chromatographic

peak, it would confirm whether the secondary and tertiary signals correspond to species with masses consistent with biochanin A dimers ($MW \approx 568.52$ Da) or higher-order aggregates. High-pressure Nuclear Magnetic Resonance (HP-NMR) spectroscopy, performed in situ within the supercritical CO_2 phase, would offer complementary evidence by monitoring changes in the chemical shift of the C7 hydroxyl proton and the aromatic protons as a function of pressure — shifts indicative of hydrogen bonding and $\pi-\pi$ stacking interactions, respectively. Similarly, High-Pressure Fourier Transform Infrared (HP-FTIR) spectroscopy would allow tracking of the O-H stretching frequency (~3200–3600 cm^{-1}) and the carbonyl stretching band (~1630 cm^{-1}) as pressure-dependent markers of association state. These experimental directions are identified as targets for future work, as they would provide the molecular-level evidence necessary to unambiguously establish the stoichiometry and geometry of the biochanin A associates.

Table 5.12 outlines the three-dimensional conformation and solvent-accessible surface of biochanin A. The molecule features a rigid, planar benzopyran core. This planar geometry promotes parallel π – π stacking interactions within the crystal lattice. This stacking causes aromatic ring overlap at close contact distances. [133], [134]. This molecular packing increases the sublimation enthalpy (ΔH^{subl}). The increased sublimation enthalpy raises the energy required to disrupt the solid matrix. This crystalline stability reduces the solute escaping tendency into the fluid phase, explaining the overall low solubility of biochanin A.

The hydroxyl group at the C7 position projects into the fluid and remains accessible for intermolecular association. At low pressures, the free volume of supercritical CO_2 keeps the biochanin A molecules separated. Beyond the 15–18 MPa threshold, the reduction in free volume forces the rigid aromatic structures into closer proximity. Under this alignment, the C7 hydroxyl groups cross the proximity threshold for hydrogen bonding. This transition triggers a shift toward fluid-phase self-association, forming reversible dimeric or trimeric complexes. This intermolecular aggregation reduces the polarity of the effective species in solution and diminishes its affinity for the supercritical solvent phase. This structural shift reduces the solute volatility, explaining the experimental non-monotonic solubility drop observed at elevated pressures.

Table 5.12. 3D representation of the molecular structure of each solute in its lowest energy (most stable) conformation, generated with Avogadro software [135] and displayed from different angles using UCSF ChimeraX [136], [137]. Atoms are color-coded for carbon (gray), hydrogen (white), and oxygen (red). The surface area corresponds to the surface excluded by the solvent.

Biochanin A 3D Structure	
View 1	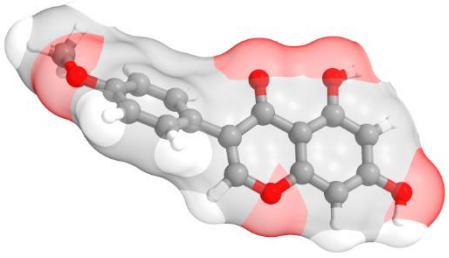
View 2	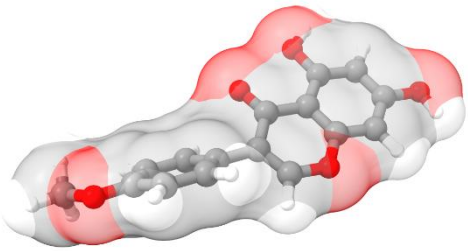
View 3	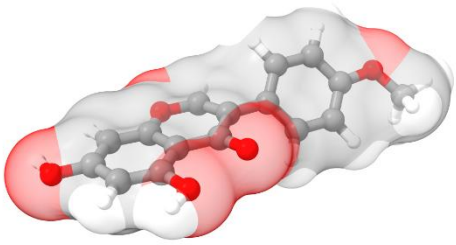

Conclusion

The isothermal solubility of the bioactive flavonoid compound, 5,7-dihydroxy-4'-methoxyisoflavone (biochanin A), dissolved in supercritical carbon dioxide at T = (313.15, 323.15 and 333.15) K and pressures ranging up to 32.0 MPa was successfully measured using a dynamic-analytical method. The three experimental solubility datasets were comprehensively validated through a rigorous procedure that allowed the estimation of the combined expanded uncertainty (U_{comb}) for each individual mole fraction (y_2), the evaluation of the thermodynamic self-consistency via the semi-empirical Méndez-Santiago and Teja (MS-T) density-based model, and the determination of thermodynamic consistency using the Valderrama and Zavaleta test. The validation procedure indicated that the measured solubility values were highly precise, yielding low procedural uncertainties and confirming strong internal self-consistency at solvent densities above 600 kg·m^{-3}. However, the thermodynamic consistency test highlighted limitations inherent to highly dilute systems, as individual deviations frequently exceeded the standard 20% validation threshold. Additionally, Nuclear Magnetic Resonance (NMR) spectroscopic analysis confirmed that the solute retained absolute chemical and structural integrity, establishing that no thermal or chemical degradation occurred during the high-pressure experimental runs.

The solubility behavior of the investigated biochanin A + CO_2 system exhibited a unique solubility profile that deviated significantly from standard, monotonic density-driven trends. Instead of continuously increasing with pressure, the molar fraction of biochanin A reached a prominent solubility maximum between 14.0 and 16.0 MPa across all three isotherms, followed by a sharp solubility drop at higher pressures. This non-monotonic behavior was justified by physical solute-solute self-association in the fluid phase. At elevated operational pressures, the severe reduction in fluid free volume brings the rigid, planar aromatic structures of biochanin A into close proximity, facilitating hydrogen bonding via the hydroxyl group at the C7 position to form heavier, less volatile molecular dimers that precipitate out of the supercritical phase.

Thermodynamic modeling using the advanced SAFT-VR Mie Equation of State (EoS) further substantiated this physical phenomenon. Pure-component and association parameters for biochanin A were successfully regressed using solid-liquid equilibrium data in alcohol modifiers, where a 4C association scheme yielded an excellent fit (AARD = 4.53%). However, when applied to the high-pressure binary CO_2 system, the standard monomeric SAFT-VR Mie framework failed to capture the solubility drop, yielding an overall AARD of 160.37% because

it does not explicitly account for competitive fluid-phase dimerization. Initial modeling within a dimeric framework verified that capturing this monomer-dimer chemical equilibrium is fundamentally necessary to reproduce the true non-monotonic solubility curve. Finally, modeling of the ternary system confirmed that the addition of an ethanol cosolvent acts as a highly effective operational strategy, structurally disrupting these solute-solute self-association networks via preferential solute-cosolvent hydrogen bonding and dramatically enhancing extraction yields.

Ongoing Work

A natural progression of this research could involve a more comprehensive thermodynamic modeling approach aimed at capturing and quantifying the hypothesized self-association of biochanin A. One promising direction would be the systematic exploration of alternative Equations of State better suited to associating systems, evaluating their descriptive and predictive capabilities against the currently employed SAFT-VR Mie framework. To address the limitations inherent in extrapolating dimeric properties from monomeric parameters, advanced computational chemistry methods — such as Density Functional Theory (DFT) or ab initio molecular dynamics simulations — could be integrated into the parameter estimation workflow. These approaches would offer rigorous, non-empirical estimations of key dimer molecular properties, including optimized geometry, effective molecular volume, and dispersion energies, without relying on the segment-identity assumptions discussed in Section 5.4.1.

On the experimental side, investigating the phase behavior of biochanin A in supercritical CO_2 modified with ethanol as a polar cosolvent may provide further insight into the self-association mechanism. Systematic solubility measurements in the ternary CO_2 + biochanin A + ethanol system could help assess whether the cosolvent preferentially disrupts solute-solute hydrogen bonding at high pressures — thereby attenuating the solubility decline — or whether it acts primarily by enhancing the overall solvating power of the supercritical phase. The experimental data generated from such a study would serve as a meaningful benchmark for the refined thermodynamic models described above. Collectively, these directions may yield a more complete mechanistic picture of the intermolecular forces governing the solubilization of complex isoflavones in supercritical fluids, potentially informing the optimization of sustainable extraction processes within the broader context of green chemistry applications.

References

[1] E. O. Lawrence, C. Galitsky, S.-C. Chang, E. Worrell, and E. Masanet, "Energy Efficiency Improvement and Cost Saving Opportunities for the Pharmaceutical Industry," 2008.

[2] M. Haji, L. Kerbache, and T. Al-Ansari, "Food Quality, Drug Safety, and Increasing Public Health Measures in Supply Chain Management," *Processes*, vol. 10, no. 9, p. 1715, Aug. 2022, doi: 10.3390/pr10091715.

[3] H. K. Biesalski *et al.*, "Bioactive compounds: Definition and assessment of activity," *Nutrition*, vol. 25, no. 11–12, pp. 1202–1205, Nov. 2009, doi: 10.1016/j.nut.2009.04.023.

[4] A. M. L. Seca and L. Moujir, "Natural compounds: A dynamic field of applications," Jun. 01, 2020, *MDPI AG*. doi: 10.3390/app10114025.

[5] J. K. Liu, "Natural products in cosmetics," Dec. 01, 2022, *Springer*. doi: 10.1007/s13659-022-00363-y.

[6] A. Hamzalıoğlu and V. Gökmen, "Interaction between Bioactive Carbonyl Compounds and Asparagine and Impact on Acrylamide," in *Acrylamide in Food*, Elsevier, 2016, pp. 355–376. doi: 10.1016/B978-0-12-802832-2.00018-8.

[7] D. J. Newman and G. M. Cragg, "Natural products as sources of new drugs over the 30 years from 1981 to 2010," Mar. 23, 2012. doi: 10.1021/np200906s.

[8] C. Forni *et al.*, "Beneficial role of phytochemicals on oxidative stress and age-related diseases," 2019, *Hindawi Limited*. doi: 10.1155/2019/8748253.

[9] B. B. Mishra and V. K. Tiwari, "Natural products: An evolving role in future drug discovery," 2011, *Elsevier Masson SAS*. doi: 10.1016/j.ejmech.2011.07.057.

[10] A. Sarfraz *et al.*, "Biochanin A: A novel bioactive multifunctional compound from nature," Jun. 20, 2020, *Elsevier B.V.* doi: 10.1016/j.scitotenv.2020.137907.

[11] A. Jain, J. C. K. Lai, and A. Bhushan, "Biochanin A inhibits endothelial cell functions and proangiogenic pathways: Implications in glioma therapy," *Anticancer Drugs*, vol. 26, no. 3, pp. 323–330, 2015, doi: 10.1097/CAD.0000000000000189.

[12] C. P. Mungwari, C. K. King'ondu, P. Sigauke, and B. A. Obadele, "Conventional and modern techniques for bioactive compounds recovery from plants: Review," *Sci. Afr.*, vol. 27, p. e02509, Mar. 2025, doi: 10.1016/j.sciaf.2024.e02509.

[13] E. Reverchon and I. De Marco, "Supercritical fluid extraction and fractionation of natural matter," *J. Supercrit. Fluids*, vol. 38, no. 2, pp. 146–166, Sep. 2006, doi: 10.1016/j.supflu.2006.03.020.

[14] A. N. Panche, A. D. Diwan, and S. R. Chandra, "Flavonoids: an overview," *J. Nutr. Sci.*, vol. 5, p. e47, Dec. 2016, doi: 10.1017/jns.2016.41.

[15] R. L. Prior, X. Wu, and L. Gu, "Flavonoid metabolism and challenges to understanding mechanisms of health effects," *J. Sci. Food Agric.*, vol. 86, no. 15, pp. 2487–2491, Dec. 2006, doi: 10.1002/jsfa.2611.

[16] L. Bravo, "Polyphenols: Chemistry, Dietary Sources, Metabolism, and Nutritional Significance," *Nutr. Rev.*, vol. 56, no. 11, pp. 317–333, Apr. 2009, doi: 10.1111/j.1753-4887.1998.tb01670.x.

[17] R. Tsao, "Chemistry and Biochemistry of Dietary Polyphenols," *Nutrients*, vol. 2, no. 12, pp. 1231–1246, Dec. 2010, doi: 10.3390/nu2121231.

[18] N. V. Zagoskina *et al.*, "Polyphenols in Plants: Structure, Biosynthesis, Abiotic Stress Regulation, and Practical Applications (Review)," *Int. J. Mol. Sci.*, vol. 24, no. 18, p. 13874, Sep. 2023, doi: 10.3390/ijms241813874.

[19] V. Lattanzio, "Phenolic compounds: Introduction," in *Natural Products: Phytochemistry, Botany and Metabolism of Alkaloids, Phenolics and Terpenes*, Springer Berlin Heidelberg, 2013, pp. 1543–1580. doi: 10.1007/978-3-642-22144-6_57.

[20] M. M. Alshehri *et al.*, "Therapeutic Potential of Isoflavones with an Emphasis on Daidzein," 2021, *Hindawi Limited*. doi: 10.1155/2021/6331630.

[21] S. A. Tidke *et al.*, "Assessment of Anticancer, Anti-inflammatory and Antioxidant Properties of Isoflavones Present in Soybean," *Research Journal of Phytochemistry*, vol. 12, pp. 35–42, 2018, [Online]. Available: https://api.semanticscholar.org/CorpusID:55610467

[22] M. Hämäläinen, R. Nieminen, P. Vuorela, M. Heinonen, and E. Moilanen, "Anti-inflammatory effects of flavonoids: Genistein, kaempferol, quercetin, and daidzein inhibit STAT-1 and NF-κB activations, whereas flavone, isorhamnetin, naringenin, and pelargonidin inhibit only NF-κB activation along with their inhibitory effect on iNOS expression and NO production in activated macrophages," *Mediators Inflamm.*, vol. 2007, 2007, doi: 10.1155/2007/45673.

[23] J. Yu, X. Bi, B. Yu, and D. Chen, "Isoflavones: Anti-inflammatory benefit and possible caveats," Jun. 10, 2016, *MDPI AG*. doi: 10.3390/nu8060361.

[24] X.-Z. He and R. A. Dixon, "Genetic Manipulation of Isoflavone 7- O -Methyltransferase Enhances Biosynthesis of 4′-O-Methylated Isoflavonoid Phytoalexins and Disease Resistance in Alfalfa," *Plant Cell*, vol. 12, no. 9, pp. 1689–1702, Sep. 2000, doi: 10.1105/tpc.12.9.1689.

[25] H. Hussain and I. R. Green, "A patent review of the therapeutic potential of isoflavones (2012-2016)," Oct. 03, 2017, *Taylor and Francis Ltd*. doi: 10.1080/13543776.2017.1339791.

[26] H. Chen *et al.*, "Developmental dynamic transcriptome and systematic analysis reveal the major genes underlying isoflavone accumulation in soybean," *Front. Plant Sci.*, vol. 14, Mar. 2023, doi: 10.3389/fpls.2023.1014349.

[27] UkrAgroConsult, "Global soybean production will reach a record level – IGC." Accessed: Mar. 12, 2025. [Online]. Available: https://ukragroconsult.com/en/news/global-soybean-production-will-reach-a-record-level-igc/

[28] V. Ramachandran, I. K. V, K. K. hr, R. Tiwari, and G. Tiwari, "Biochanin-A: A Bioactive Natural Product with Versatile Therapeutic Perspectives," *Curr. Drug Res. Rev.*, vol. 14, no. 3, pp. 225–238, Nov. 2022, doi: 10.2174/2589977514666220509201804.

[29] P. Sithisarn, M. Michaelis, M. Schubert-Zsilavecz, and J. Cinatl, "Differential antiviral and anti-inflammatory mechanisms of the flavonoids biochanin A and baicalein in H5N1 influenza A virus-infected cells," *Antiviral Res.*, vol. 97, no. 1, pp. 41–48, Jan. 2013, doi: 10.1016/j.antiviral.2012.10.004.

[30] A. Kumar, E. Angelopoulou, E. Pyrgelis, C. Piperi, and A. Mishra, "Harnessing Therapeutic Potentials of Biochanin A in Neurological Disorders: Pharmacokinetic and Pharmacodynamic Overview," *Chem. Biodivers.*, vol. 21, no. 8, Aug. 2024, doi: 10.1002/cbdv.202400709.

[31] L. Kole, B. Giri, S. K. Manna, B. Pal, and S. Ghosh, "Biochanin-A, an isoflavon, showed anti-proliferative and anti-inflammatory activities through the inhibition of iNOS expression, p38-MAPK and ATF-2 phosphorylation and blocking NFκB nuclear translocation," *Eur. J. Pharmacol.*, vol. 653, no. 1–3, pp. 8–15, Feb. 2011, doi: 10.1016/j.ejphar.2010.11.026.

[32] J. Tan and M. Kim, "Neuroprotective Effects of Biochanin A against β-Amyloid-Induced Neurotoxicity in PC12 Cells via a Mitochondrial-Dependent Apoptosis Pathway," *Molecules*, vol. 21, no. 5, p. 548, Apr. 2016, doi: 10.3390/molecules21050548.

[33] A.-S. A.-S. Newairy, F. A. Hamaad, M. M. Wahby, M. Ghoneum, and H. M. Abdou, "Neurotherapeutic effects of quercetin-loaded nanoparticles and Biochanin-A extracted from Trifolium alexandrinum on PI3K/Akt/GSK-3β signaling in the cerebral cortex of male diabetic rats," *PLoS One*, vol. 19, no. 4, p. e0301355, Apr. 2024, doi: 10.1371/journal.pone.0301355.

[34] R. S. Aldhahri *et al.*, "Biochanin A Improves Memory Decline and Brain Pathology in Cuprizone-Induced Mouse Model of Multiple Sclerosis," *Behavioral Sciences*, vol. 12, no. 3, p. 70, Mar. 2022, doi: 10.3390/bs12030070.

[35] Y. J. Moon, S. Zhang, D. A. Brazeau, and M. E. Morris, "Effects of the flavonoid biochanin A on gene expression in primary human hepatocytes and human intestinal cells," *Mol. Nutr. Food Res.*, vol. 51, no. 3, pp. 317–323, Mar. 2007, doi: 10.1002/mnfr.200600156.

[36] L. Bravo, "Polyphenols: Chemistry, Dietary Sources, Metabolism, and Nutritional Significance," *Nutr. Rev.*, vol. 56, no. 11, pp. 317–333, Apr. 2009, doi: 10.1111/j.1753-4887.1998.tb01670.x.

[37] K. D. R. Setchell and A. Cassidy, "Dietary Isoflavones: Biological Effects and Relevance to Human Health," *J. Nutr.*, vol. 129, no. 3, pp. 758S-767S, Mar. 1999, doi: 10.1093/jn/129.3.758S.

[38] O. K. Chun, S. J. Chung, and W. O. Song, "Estimated Dietary Flavonoid Intake and Major Food Sources of U.S. Adults," *J. Nutr.*, vol. 137, no. 5, pp. 1244–1252, May 2007, doi: 10.1093/jn/137.5.1244.

[39] M. Mikulić *et al.*, "Phytochemical Composition of Different Red Clover Genotypes Based on Plant Part and Genetic Traits," *Foods*, vol. 13, no. 1, p. 103, Dec. 2023, doi: 10.3390/foods13010103.

[40] Z.-J. Feng and W.-F. Lai, "Chemical and Biological Properties of Biochanin A and Its Pharmaceutical Applications," *Pharmaceutics*, vol. 15, no. 4, p. 1105, Mar. 2023, doi: 10.3390/pharmaceutics15041105.

[41] T. Blicharski and A. Oniszczuk, "Extraction Methods for the Isolation of Isoflavonoids from Plant Material," *Open Chem.*, vol. 15, no. 1, pp. 34–45, Mar. 2017, doi: 10.1515/chem-2017-0005.

[42] Z. Luo *et al.*, "Optimization of ultrasound-assisted extraction based on response surface methodology using HPLC-DAD for the analysis of red clover (Trifolium pretense L.) isoflavones and its anti-inflammatory activities on LPS-induced 3D4/2 cell," *Front. Vet. Sci.*, vol. 10, Oct. 2023, doi: 10.3389/fvets.2023.1279178.

[43] M. A. Rostagno, M. Palma, and C. G. Barroso, "Microwave assisted extraction of soy isoflavones," *Anal. Chim. Acta*, vol. 588, no. 2, pp. 274–282, Apr. 2007, doi: 10.1016/j.aca.2007.02.010.

[44] T. Bajer, M. Adam, L. Galla, and K. Ventura, "Comparison of various extraction techniques for isolation and determination of isoflavonoids in plants," *J. Sep. Sci.*, vol. 30, no. 1, pp. 122–127, Jan. 2007, doi: 10.1002/jssc.200600306.

[45] Y. Hao, F. Pei, J. Huang, G. Li, and C. Zhong, "Application of deep eutectic solvents on extraction of flavonoids," *J. Sep. Sci.*, vol. 47, no. 9–10, May 2024, doi: 10.1002/jssc.202300925.

[46] S. Bajkacz and J. Adamek, "Evaluation of new natural deep eutectic solvents for the extraction of isoflavones from soy products," *Talanta*, vol. 168, pp. 329–335, Jun. 2017, doi: 10.1016/j.talanta.2017.02.065.

[47] B. A. S. Machado, C. G. Pereira, S. B. Nunes, F. F. Padilha, and M. A. Umsza-Guez, "Supercritical Fluid Extraction Using CO_2: Main Applications and Future Perspectives," *Sep. Sci. Technol.*, vol. 48, no. 18, pp. 2741–2760, Dec. 2013, doi: 10.1080/01496395.2013.811422.

[48] M. A. Rostagno, J. M. A. Araújo, and D. Sandi, "Supercritical fluid extraction of isoflavones from soybean flour," *Food Chem.*, vol. 78, no. 1, pp. 111–117, Jul. 2002, doi: 10.1016/S0308-8146(02)00106-1.

[49] J. D. Chea, A. L. Lehr, J. F. Stanzione, and K. M. Yenkie, "Evaluation of isoflavone extraction options at commercial scale," *Biofuels, Bioproducts and Biorefining*, vol. 16, no. 6, pp. 1708–1725, Nov. 2022, doi: 10.1002/bbb.2411.

[50] A. Witkowski, M. Majkut, and S. Rulik, "Analysis of pipeline transportation systems for carbon dioxide sequestration," *Archives of Thermodynamics*, vol. 35, no. 1, pp. 117–140, Mar. 2014, doi: 10.2478/aoter-2014-0008.

[51] A. E. Ramazanova and I. M. Abdulagatov, "Thermal Conductivity of Supercritical CO2-Saturated Coal," *Int. J. Thermophys.*, vol. 42, no. 1, p. 2, Jan. 2021, doi: 10.1007/s10765-020-02756-y.

[52] J. M. H. L. Sengers, "Supercritical Fluids: Their Properties and Applications," in *Supercritical Fluids: Fundamentals and Applications*, P. G. and P. C. J. Kiran Erdogan and Debenedetti, Ed., Dordrecht: Springer Netherlands, 2000, pp. 1–29. doi: 10.1007/978-94-011-3929-8_1.

[53] M. Mukhopadhyay, "Extraction and processing with supercritical fluids," *Journal of Chemical Technology & Biotechnology*, vol. 84, no. 1, pp. 6–12, Jan. 2009, doi: 10.1002/jctb.2072.

[54] A. Majumdar *et al.*, "Direct observation of ultrafast cluster dynamics in supercritical carbon dioxide using X-ray Photon Correlation Spectroscopy," *Nat. Commun.*, vol. 15, no. 1, p. 10540, Dec. 2024, doi: 10.1038/s41467-024-54782-1.

[55] T. Ahmad, F. A. Masoodi, S. A. Rather, S. M. Wani, and A. Gull, "Supercritical Fluid Extraction: A Review," *Journal of Biological and chemical Chronicles*, vol. 5, no. 1, pp. 114–122, Feb. 2019, doi: 10.33980/jbcc.2019.v05i01.019.

[56] Mr. W. Yash Prakash, Assist. Prof. K. S. Kale, and Dr. M. Salve, "A review Article on: Supercritical Fluid Extraction," *International Journal of Pharmaceutical Research and Applications*, vol. 09, no. 05, pp. 1172–1178, May 2024, doi: 10.35629/4494-090511721178.

[57] R. P. F. F. da Silva, T. A. P. Rocha-Santos, and A. C. Duarte, "Supercritical fluid extraction of bioactive compounds," Feb. 01, 2016, *Elsevier B.V.* doi: 10.1016/j.trac.2015.11.013.

[58] M. Herrero, J. A. Mendiola, A. Cifuentes, and E. Ibáñez, "Supercritical fluid extraction: Recent advances and applications," *J. Chromatogr. A*, vol. 1217, no. 16, pp. 2495–2511, Apr. 2010, doi: 10.1016/j.chroma.2009.12.019.

[59] C. L. Phelps, N. G. Smart, and C. M. Wai, "Past, Present, and Possible Future Applications of Supercritical Fluid Extraction Technology," 1996. [Online]. Available: https://pubs.acs.org/sharingguidelines

[60] K.-Y. Khaw, M.-O. Parat, P. N. Shaw, and J. R. Falconer, "Solvent Supercritical Fluid Technologies to Extract Bioactive Compounds from Natural Sources: A Review," *Molecules*, vol. 22, no. 7, p. 1186, Jul. 2017, doi: 10.3390/molecules22071186.

[61] E. Reverchon and I. De Marco, "Supercritical fluid extraction and fractionation of natural matter," *J. Supercrit. Fluids*, vol. 38, no. 2, pp. 146–166, Sep. 2006, doi: 10.1016/j.supflu.2006.03.020.

[62] E. Reverchon and I. De Marco, "Essential Oils Extraction and Fractionation Using Supercritical Fluids," in *Supercritical Fluid Extraction of Nutraceuticals and Bioactive Compounds*, J. L. Martinez, Ed., CRC Press, 2008, pp. 305–328.

[63] Ž. Knez, E. Markočič, M. Leitgeb, M. Primožič, M. Knez Hrnčič, and M. Škerget, "Industrial applications of supercritical fluids: A review," *Energy*, vol. 77, pp. 235–243, Dec. 2014, doi: 10.1016/j.energy.2014.07.044.

[64] Y. B. Zuo, A. W. Zeng, X. G. Yuan, and K. T. Yu, "Extraction of soybean isoflavones from soybean meal with aqueous methanol modified supercritical carbon dioxide," *J. Food Eng.*, vol. 89, no. 4, pp. 384–389, Dec. 2008, doi: 10.1016/j.jfoodeng.2008.05.004.

[65] J.-Z. He, P. Shao, J.-H. Liu, and Q.-M. Ru, "Supercritical Carbon Dioxide Extraction of Flavonoids from Pomelo (Citrus grandis (L.) Osbeck) Peel and Their Antioxidant Activity," *Int. J. Mol. Sci.*, vol. 13, no. 10, pp. 13065–13078, Oct. 2012, doi: 10.3390/ijms131013065.

[66] M. V. Palmer and S. S. T. Ting, "Applications for supercritical fluid technology in food processing," *Food Chem.*, vol. 52, no. 4, pp. 345–352, Jan. 1995, doi: 10.1016/0308-8146(95)93280-5.

[67] D. K. Dandge, J. P. Heller, and K. V Wilson, "Structure solubility correlations: organic compounds and dense carbon dioxide binary systems," *Industrial & Engineering Chemistry Product Research and Development*, vol. 24, no. 1, pp. 162–166, Mar. 1985, doi: 10.1021/i300017a030.

[68] M. McHugh and M. E. Paulaitis, "Solid solubilities of naphthalene and biphenyl in supercritical carbon dioxide," *J. Chem. Eng. Data*, vol. 25, no. 4, pp. 326–329, Oct. 1980, doi: 10.1021/je60087a018.

[69] V. Reddy and M. Saharay, "Solubility of Caffeine in Supercritical CO2 : A Molecular Dynamics Simulation Study," *J. Phys. Chem. B*, vol. 123, no. 45, pp. 9685–9691, Nov. 2019, doi: 10.1021/acs.jpcb.9b08351.

[70] F. Ingrosso and M. F. Ruiz-López, "Modeling Solvation in Supercritical CO2," *ChemPhysChem*, vol. 18, no. 19, pp. 2560–2572, Oct. 2017, doi: 10.1002/cphc.201700434.

[71] M. Calcara and M. Caricaterra, "CO2 Dipole Moment: A Simple Model and Its Implications for CO2-Rock Interactions," *Minerals*, vol. 13, no. 1, p. 87, Jan. 2023, doi: 10.3390/min13010087.

[72] P. Raveendran, Y. Ikushima, and S. L. Wallen, "Polar attributes of supercritical carbon dioxide," *Acc. Chem. Res.*, vol. 38, no. 6, pp. 478–485, Jun. 2005, doi: 10.1021/ar040082m.

[73] B. Gerd, "Supercritical Gases as Solvents: Phase Equilibria," Springer-Verlag Berlin Heidelberg, 1994, ch. 3. doi: 10.1007/978-3-662-07380-3.

[74] Z.-Z. Yang, Q.-W. Song, and L.-N. He, *Capture and Utilization of Carbon Dioxide with Polyethylene Glycol*. Berlin, Heidelberg: Springer Berlin Heidelberg, 2012. doi: 10.1007/978-3-642-31268-7.

[75] J. Jin, C. Chang, J. Zhu, H. Wu, and Z. Zhang, "Solubility of Poly(vinylpyrrolidone) with Different Molecular Weights in Supercritical Carbon Dioxide," *J. Chem. Eng. Data*, vol. 60, no. 11, pp. 3397–3403, Nov. 2015, doi: 10.1021/acs.jced.5b00659.

[76] E. Girard, T. Tassaing, J.-D. Marty, and M. Destarac, "Influence of macromolecular characteristics of RAFT/MADIX poly(vinyl acetate)-based (co)polymers on their solubility in supercritical carbon dioxide," *Polym. Chem.*, vol. 2, no. 10, p. 2222, 2011, doi: 10.1039/c1py00209k.

[77] J. M. Dobbs, J. M. Wong, R. J. Lahiere, and K. P. Johnston, "Modification of supercritical fluid phase behavior using polar cosolvents," *Ind. Eng. Chem. Res.*, vol. 26, no. 1, pp. 56–65, Jan. 1987, doi: 10.1021/ie00061a011.

[78] M. A. Mamani, J. M. del Valle, P. Aravena, and R. Canales, "An experimental methodology to validate the use of hydroethanolic mixtures as suspending medium / modifier for the supercritical CO2 extraction of suspensions," *J. Supercrit. Fluids*, vol. 216, p. 106423, Feb. 2025, doi: 10.1016/j.supflu.2024.106423.

[79] M. P. Ekart, K. L. Bennett, S. M. Ekart, G. S. Gurdial, C. L. Liotta, and C. A. Eckert, "Cosolvent Interactions in Supercritical Fluid Solutions," *AiChE Journal*, 1993.

[80] J. Wang and H. Jin, "Molecular Dynamics Simulation Investigation of the Solubility Parameter of Supercritical Carbon Dioxide-Cosolvent," in *2024 9th International Conference on Smart and Sustainable Technologies (SpliTech)*, IEEE, Jun. 2024, pp. 1–5. doi: 10.23919/SpliTech61897.2024.10612421.

[81] J. M. Dobbs and K. P. Johnston, "Selectivities in pure and mixed supercritical fluid solvents," *Ind. Eng. Chem. Res.*, vol. 26, no. 7, pp. 1476–1482, Jul. 1987, doi: 10.1021/ie00067a035.

[82] M. Ota, Y. Hashimoto, M. Sato, Y. Sato, R. L. Smith, and H. Inomata, "Solubility of flavone, 6-methoxyflavone and anthracene in supercritical CO2 with/without a co-solvent of ethanol correlated by using a newly proposed entropy-based solubility parameter," *Fluid Phase Equilib.*, vol. 425, pp. 65–71, Oct. 2016, doi: 10.1016/j.fluid.2016.05.009.

[83] M. Nakada, M. Imai, and I. Suzuki, "Impact of ethanol addition on the solubility of various soybean isoflavones in supercritical carbon dioxide and the effect of glycoside chain in isoflavones," *J. Food Eng.*, vol. 95, no. 4, pp. 564–571, Dec. 2009, doi: 10.1016/j.jfoodeng.2009.06.020.

[84] T.-H. Kao, J.-T. Chien, and B.-H. Chen, "Extraction yield of isoflavones from soybean cake as affected by solvent and supercritical carbon dioxide," *Food Chem.*, vol. 107, no. 4, pp. 1728–1736, Apr. 2008, doi: 10.1016/j.foodchem.2007.10.015.

[85] Y. B. Zuo, A. W. Zeng, X. G. Yuan, and K. T. Yu, "Extraction of soybean isoflavones from soybean meal with aqueous methanol modified supercritical carbon dioxide," *J. Food Eng.*, vol. 89, no. 4, pp. 384–389, Dec. 2008, doi: 10.1016/j.jfoodeng.2008.05.004.

[86] R. Dohrn, J. M. S. Fonseca, and S. Peper, "Experimental Methods for Phase Equilibria at High Pressures," *Annu. Rev. Chem. Biomol. Eng.*, vol. 3, no. 1, pp. 343–367, Jul. 2012, doi: 10.1146/annurev-chembioeng-062011-081008.

[87] A. L. Cabrera, A. R. Toledo, J. M. del Valle, and J. C. de la Fuente, "Measuring and validation for isothermal solubility data of solid 2-(3,4-Dimethoxyphenyl)-5,6,7,8-tetramethoxychromen-4-one (nobiletin) in supercritical carbon dioxide," *J. Chem. Thermodyn.*, vol. 91, pp. 378–383, Dec. 2015, doi: 10.1016/j.jct.2015.08.018.

[88] G. A. Naikoo, M. Saeedi Zadegan, M. Zamani Pedram, I. U. Hassan, W. Ahmed, and G. Yousefi Attar, "Solubility of vitamin A in supercritical CO2: experimental study and thermodynamic modeling," *Sci. Rep.*, vol. 11, no. 1, p. 15917, Aug. 2021, doi: 10.1038/s41598-021-92374-x.

[89] S. Peper and R. Dohrn, "Sampling from fluid mixtures under high pressure: Review, case study and evaluation," *J. Supercrit. Fluids*, vol. 66, pp. 2–15, Jun. 2012, doi: 10.1016/j.supflu.2011.09.021.

[90] P. Guilbot, A. Valtz, H. Legendre, and D. Richon, "Rapid on-line sampler-injector: a reliable tool for HT-HP sampling and on-line GC analysis," *Analusis*, vol. 28, no. 5, pp. 426–431, Jun. 2000, doi: 10.1051/analusis:2000128.

[91] O. Pfohl, J. Timm, R. Dohrn, and G. Brunner, "Measurement and correlation of vapor-liquid-liquid equilibria in the glucose + acetone + water + carbon dioxide system," *Fluid Phase Equilib.*, vol. 124, no. 1–2, pp. 221–233, Sep. 1996, doi: 10.1016/S0378-3812(96)03098-1.

[92] Q. Dong, R. D. Chirico, X. Yan, X. Hong, and M. Frenkel, "Uncertainty Reporting for Experimental Thermodynamic Properties," *J. Chem. Eng. Data*, vol. 50, no. 2, pp. 546–550, Mar. 2005, doi: 10.1021/je049673d.

[93] P. M. Clifford, "The international vocabulary of basic and general terms in metrology," *Measurement*, vol. 3, no. 2, pp. 72–76, Apr. 1985, doi: 10.1016/0263-2241(85)90006-5.

[94] R. D. Chirico, M. Frenkel, V. V. Diky, K. N. Marsh, and R. C. Wilhoit, "ThermoMLAn XML-Based Approach for Storage and Exchange of Experimental and Critically Evaluated Thermophysical and Thermochemical Property Data. 2. Uncertainties," *J. Chem. Eng. Data*, vol. 48, no. 5, pp. 1344–1359, Sep. 2003, doi: 10.1021/je034088i.

[95] S. Bell, "Measurement Good Practice Guide: A Beginner's Guide to Uncertainty of Measurement," 1999.

[96] E. W. Lemmon, I. H. Bell, M. L. Huber, and M. O. McLinden, "NIST Standard Reference Database 23: Reference Fluid Thermodynamic and Transport Properties-REFPROP, Version 10.0," 2018, *Gaithersburg*.

[97] J. O. Valderrama and J. Zavaleta, "Thermodynamic consistency test for high pressure gas–solid solubility data of binary mixtures using genetic algorithms," *J. Supercrit. Fluids*, vol. 39, no. 1, pp. 20–29, Nov. 2006, doi: 10.1016/j.supflu.2006.02.003.

[98] R. Chirico, M. Frenkel, V. Diky, K. Marsh, and R. Wilhoit, "ThermoML - An XML-Based Approach for Storage and Exchange of Experimental and Critically Evaluated Thermophysical and Thermochemical Property Data 2. Uncertainties," no. 48, May 2003.

[99] J. O. Valderrama, P. A. Robles, and J. C. de la Fuente, "Determining the Sublimation Pressure of Capsaicin Using High-Pressure Solubility Data of Capsaicin + CO2 Mixtures," *J. Chem. Eng. Data*, vol. 51, no. 5, pp. 1783–1787, Sep. 2006, doi: 10.1021/je060188n.

[100] M. Türk, M. Crone, and T. Kraska, "A comparison between models based on equations of state and density-based models for describing the solubility of solutes in CO2," *J. Supercrit. Fluids*, vol. 55, no. 2, pp. 462–471, Dec. 2010, doi: 10.1016/j.supflu.2010.08.011.

[101] J. Méndez-Santiago and A. S. Teja, "The solubility of solids in supercritical fluids," *Fluid Phase Equilib.*, vol. 158–160, pp. 501–510, Jun. 1999, doi: 10.1016/S0378-3812(99)00154-5.

[102] J. C. de la Fuente, B. Oyarzún, N. Quezada, and J. M. del Valle, "Solubility of carotenoid pigments (lycopene and astaxanthin) in supercritical carbon dioxide," *Fluid Phase Equilib.*, vol. 247, no. 1–2, pp. 90–95, Sep. 2006, doi: 10.1016/j.fluid.2006.05.031.

[103] A. Zeinolabedini Hezave and F. Esmaeilzadeh, "Solubility Measurement of Diclofenac Acid in the Supercritical CO2," *J. Chem. Eng. Data*, vol. 57, no. 6, pp. 1659–1664, Jun. 2012, doi: 10.1021/je200012x.

[104] J. S. Rowlinson and F. L. Swinton, *Liquids and Liquid Mixtures: Butterworths Monographs in Chemistry*, 3rd ed. Butterworth-Heinemann, 2013.

[105] M. A. McHugh, J. J. Watkins, B. T. Doyle, and V. J. Krukonis, "High-pressure naphthalene-xenon phase behavior," *Ind. Eng. Chem. Res.*, vol. 27, no. 6, pp. 1025–1033, Jun. 1988, doi: 10.1021/ie00078a023.

[106] J. O. Valderrama, P. A. Robles, and J. C. de la Fuente, "Determining the Sublimation Pressure of Capsaicin Using High-Pressure Solubility Data of Capsaicin + CO2 Mixtures," *J. Chem. Eng. Data*, vol. 51, no. 5, pp. 1783–1787, Sep. 2006, doi: 10.1021/je060188n.

[107] A. Gil-Villegas, A. Galindo, P. J. Whitehead, S. J. Mills, G. Jackson, and A. N. Burgess, "Statistical associating fluid theory for chain molecules with attractive potentials of variable range," *J. Chem. Phys.*, vol. 106, no. 10, pp. 4168–4186, Mar. 1997, doi: 10.1063/1.473101.

[108] W. G. Chapman, K. E. Gubbins, G. Jackson, and M. Radosz, "SAFT: Equation-of-state solution model for associating fluids," *Fluid Phase Equilib.*, vol. 52, pp. 31–38, Dec. 1989, doi: 10.1016/0378-3812(89)80308-5.

[109] S. H. Huang and M. Radosz, "Equation of state for small, large, polydisperse, and associating molecules," *Ind. Eng. Chem. Res.*, vol. 29, no. 11, pp. 2284–2294, Nov. 1990, doi: 10.1021/ie00107a014.

[110] S. H. Huang and M. Radosz, "Equation of state for small, large, polydisperse, and associating molecules: extension to fluid mixtures," *Ind. Eng. Chem. Res.*, vol. 30, no. 8, pp. 1994–2005, Aug. 1991, doi: 10.1021/ie00056a050.

[111] T. Lafitte *et al.*, "Accurate statistical associating fluid theory for chain molecules formed from Mie segments," *J. Chem. Phys.*, vol. 139, no. 15, Oct. 2013, doi: 10.1063/1.4819786.

[112] A. Mejía, C. Herdes, and E. A. Müller, "Force Fields for Coarse-Grained Molecular Simulations from a Corresponding States Correlation," *Ind. Eng. Chem. Res.*, vol. 53, no. 10, pp. 4131–4141, Mar. 2014, doi: 10.1021/ie404247e.

[113] L. Constantinou and R. Gani, "New Group Contribution Method for Estimating Properties of Pure Compounds," *AIChE Journal*, vol. 40, no. 10, 1994, doi: https://doi.org/10.1002/aic.690401011.

[114] K. G. Joback and R. C. Reid, "ESTIMATION OF PURE-COMPONENT PROPERTIES FROM GROUP-CONTRIBUTIONS," *Chem. Eng. Commun.*, vol. 57, no. 1–6, pp. 233–243, Jul. 1987, doi: 10.1080/00986448708960487.

[115] National Center for Biotechnology Information (NCBI), "PubChem Compound Summary for CID 5280373, Biochanin A." Accessed: Aug. 31, 2025. [Online]. Available: https://pubchem.ncbi.nlm.nih.gov/compound/Biochanin-A

[116] M. C. dos Ramos, J. D. Haley, J. R. Westwood, and C. McCabe, "Extending the GC-SAFT-VR approach to associating functional groups: Alcohols, aldehydes, amines and carboxylic acids," *Fluid Phase Equilib.*, vol. 306, no. 1, pp. 97–111, Jul. 2011, doi: 10.1016/j.fluid.2011.03.026.

[117] A. Immirzi and B. Perini, "Prediction of density in organic crystals," *Acta Crystallographica Section A*, vol. 33, no. 1, pp. 216–218, Jan. 1977, doi: 10.1107/S0567739477000448.

[118] M. L. Sage, G. W. Sage, R. S. Boethling, and D. Mackay, *Handbook of Property Estimation Methods for Chemicals*. CRC Press, 2000. doi: 10.1201/9781420026283.

[119] S. E. Stein and R. L. Brown, "Estimation of normal boiling points from group contributions," *J. Chem. Inf. Comput. Sci.*, vol. 34, no. 3, pp. 581–587, May 1994, doi: 10.1021/ci00019a016.

[120] P. J. Walker, H.-W. Yew, and A. Riedemann, "Clapeyron.jl: An Extensible, Open-Source Fluid Thermodynamics Toolkit," *Ind. Eng. Chem. Res.*, vol. 61, no. 20, pp. 7130–7153, May 2022, doi: 10.1021/acs.iecr.2c00326.

[121] Carl Roth GmbH + Co. KG, "Safety Data Sheet: Biochanin A ≥95 % (Article number: 2ECL)," Karlsruhe, Jul. 2025. Accessed: Jun. 08, 2026. [Online]. Available: https://www.carlroth.com/medias/SDB-2ECL-DE-EN.pdf?context=bWFzdGVyfHNlY3VyaXR5RGF0YXNoZWV0c3wyMzg0NTB8YXBwbGljYXRpb24vcGRmfGFEaGpMMmhrTUM4NU1qSTVNekExTkRjNU1UazRMMU5FUWw4eVJVTk1YMFJGWDBWT0xuQmtaZ3wxZDZkNmUwMDA5ZmU2ZTRiYzJjMzc0ZTIzMGNkYzRlMjhlNmQ4ODhkMDRkYjg1YzNlYzMxNjYxN2UyZjMzNDc0

[122] C. Morales-Díaz, A. L. Cabrera, J. C. de la Fuente, and A. Mejía, "Modelling of solubility of vitamin K3 derivatives in supercritical carbon dioxide using cubic and SAFT equations of state," *J. Supercrit. Fluids*, vol. 167, p. 105040, Jan. 2021, doi: 10.1016/j.supflu.2020.105040.

[123] A. C. Schulz, F. C. Zacconi, A. L. Cabrera, J. M. del Valle, L. Espinoza, and J. C. de la Fuente, "Solubility in supercritical carbon dioxide of two novel amine derivatives of 2,3-dichloronaphthalene-1,4-dione (dichlone)," *J. Supercrit. Fluids*, vol. 201, p. 106034, Oct. 2023, doi: 10.1016/j.supflu.2023.106034.

[124] R. Canales, "Evaluación del efecto de cosolventes lìpidos sobre la solubilidad de pigmentos carotenoides en CO2 supercrítico," UTFSM, 2012.

[125] J. Arias, J. Martínez, E. Stashenko, J. M. del Valle, and J. C. de la Fuente, "Supercritical CO2 extraction of pinocembrin from Lippia origanoides distillation residues. 1. Multicomponent solubility and equilibrium partition," *Journal of Supercritical Fluids*, vol. 180, Feb. 2022, doi: 10.1016/j.supflu.2021.105426.

[126] K. A. Araus, R. I. Canales, J. M. del Valle, and J. C. de la Fuente, "Solubility of β-carotene in ethanol- and triolein-modified CO2," *J. Chem. Thermodyn.*, vol. 43, no. 12, pp. 1991–2001, Dec. 2011, doi: 10.1016/j.jct.2011.07.013.

[127] P. Robert, N. Romero, J. Ortiz, L. Masson, and D. Barrera-Arellano, "Effect of rosa mosqueta (Rosa rubiginosa) extract on the performance of chilean hazelnut oil (Gevuina avellana Mol.) at high temperature," *J. Am. Oil Chem. Soc.*, vol. 83, no. 8, Aug. 2006, doi: 10.1007/s11746-006-5025-y.

[128] K. A. Araus, J. M. del Valle, P. S. Robert, and J. C. de la Fuente, "Effect of triolein addition on the solubility of capsanthin in supercritical carbon dioxide," *J. Chem. Thermodyn.*, vol. 51, pp. 190–194, Aug. 2012, doi: 10.1016/j.jct.2012.02.030.

[129] R. Span and W. Wagner, "A New Equation of State for Carbon Dioxide Covering the Fluid Region from the Triple-Point Temperature to 1100 K at Pressures up to 800 MPa," *J. Phys. Chem. Ref. Data*, vol. 25, no. 6, pp. 1509–1596, Nov. 1996, doi: 10.1063/1.555991.

[130] D. Ambrose and C. H. S. Sprake, "Thermodynamic properties of organic oxygen compounds XXVJ Vapour pressures and normal boiling temperatures of aliphatic alcohols," 1970.

[131] S. A. M. Smith, J. T. Cripwell, and C. E. Schwarz, "Application of Renormalization Corrections to SAFT-VR Mie," *Ind. Eng. Chem. Res.*, vol. 61, no. 34, pp. 12797–12812, Aug. 2022, doi: 10.1021/acs.iecr.2c02004.

[132] S. A. Febra, A. Aasen, C. S. Adjiman, G. Jackson, and A. Galindo, "Intramolecular bonding in a statistical associating fluid theory of ring aggregates," *Mol. Phys.*, vol. 117, no. 23–24, pp. 3884–3912, Dec. 2019, doi: 10.1080/00268976.2019.1671619.

[133] G. A. Krestov, "Enthalpies of Fusion, Sublimation and Vaporization of Some Hydrazones," 2017. [Online]. Available: www.tsijournals.com

[134] Z.-T. Zhang and Y.-C. Wang, "Hydrogen bonding and π–π stacking in 6-hydroxybiochanin A monohydrate," *Acta Crystallogr. C*, vol. 63, no. 1, pp. o51–o53, Dec. 2006.

[135] M. D. Hanwell, D. E. Curtis, D. C. Lonie, T. Vandermeersch, E. Zurek, and G. R. Hutchison, "Avogadro: an advanced semantic chemical editor, visualization, and analysis platform," *J. Cheminform.*, vol. 4, no. 1, p. 17, Dec. 2012, doi: 10.1186/1758-2946-4-17.

[136] E. F. Pettersen *et al.*, "UCSF ChimeraX: Structure visualization for researchers, educators, and developers," *Protein Science*, vol. 30, no. 1, pp. 70–82, Jan. 2021, doi: 10.1002/pro.3943.

[137] T. D. Goddard *et al.*, "UCSF ChimeraX: Meeting modern challenges in visualization and analysis," *Protein Science*, vol. 27, no. 1, pp. 14–25, Jan. 2018, doi: 10.1002/pro.3235.

Appendices

Appendix A: Julia Code for ethanol (3) and 2-Propanol (4) SAFT-VR Mie molecular parameter fit.

```julia
using Clapeyron
using Metaheuristics
using CSV, DataFrames
using Plots
using Statistics: mean
using Printf

ruta1 = raw"C:\Users\villa\OneDrive\Escritorio\pure.csv"
ruta2 = raw"C:\Users\villa\OneDrive\Escritorio\assoc.csv"
solventes = ["ethanol", "2propanol"]

# REF: https://doi.org/10.1016/0021-9614(70)90038-8
datos_exp = Dict(
    "ethanol" => (
        T = [292.772, 296.783, 298.872, 301.307, 306.484, 309.756, 312.387, 316.378, 320.499, 324.231,
            327.814, 332.023, 336.015, 339.728, 343.709, 348.130, 350.555, 351.139, 351.490, 351.647,
            352.338, 355.512, 358.986, 362.756, 366.631],
        P = [5726.0,   7269.0,   8205.0,   9430.0,  12566.0, 14981.0,  17200.0,  21109.0,  25914.0,  31047.0,
             36760.0,  44584.0,  53267.0,  62572.0,  74032.0, 88763.0,  97821.0, 100121.0, 101518.0, 102151.0,
             104983.0, 118719.0, 135519.0, 155824.0, 179321.0]
    ),
    "2propanol" => (
        T = [325.473, 329.929, 333.948, 337.241, 340.237, 342.854, 345.281, 347.522, 349.604, 351.581,
             353.310, 355.081, 356.108, 358.240, 359.700, 361.072, 362.411],
        P = [26540.0,  33044.0,  40017.0,  46612.0,  53371.0, 59931.0,  66601.0,  73286.0,  79997.0,  86822.0,
             93175.0, 100079.0, 104266.0, 113416.0, 120046.0, 126573.0, 133218.0]
    )
)

function actualizar_parametros_puros!(model, m, σ, ε, λr, εk_assoc, κ_assoc)
    model.params.segment.values[1]  = m
    model.params.sigma.values[1,1]  = σ
    model.params.epsilon.values[1,1]  = ε
    model.params.lambda_r.values[1,1] = λr

    ea = model.params.epsilon_assoc
    bv = model.params.bondvol

    for k in 1:length(ea.values.values)
        ea.values.values[k] = εk_assoc
        bv.values.values[k] = κ_assoc
    end
end

function crear_objetivo(model_base, T_exp, P_exp)
    eval_count = Ref(0)
    best_so_far = Ref(1e10)

    function objetivo(params::Vector{Float64})
        any(isnan, params) || any(isinf, params) && return 1e10

        m        = exp(params[1])
        σ        = exp(params[2])
        ε        = exp(params[3])
        λr       = exp(params[4])
        εk_assoc = exp(params[5])
        κ_assoc  = exp(params[6])
```

Figure A.1. Julia code for fitting molecular parameters of ethanol (3) and 2-Propanol (4) from vapor pressure data from Ambrose & Sprake [130].

```
        (m < 1.0 || m > 6.0) && return 1e10
        (σ < 2.5e-10 || σ > 5.5e-10) && return 1e10
        (ε < 150.0 || ε > 500.0) && return 1e10
        (λr < 8.0  || λr > 35.0) && return 1e10
        (εk_assoc < 1000.0 || εk_assoc > 4000.0) && return 1e10
        (κ_assoc < 1e-34 || κ_assoc > 1e-30) && return 1e10

        eval_count[] += 1

        actualizar_parametros_puros!(model_base, m, σ, ε, λr, εk_assoc, κ_assoc)

        sse_total = 0.0
        n_total = length(T_exp)

        try
            for (T, P_obs) in zip(T_exp, P_exp)
                res = Clapeyron.saturation_pressure(model_base, T)
                P_calc = res[1]

                if isnan(P_calc) || isinf(P_calc) || P_calc <= 0.0
                    return 1e10
                end

                sse_total += (log(P_calc) - log(P_obs))^2
            end
        catch
            return 1e10
        end

        val = sse_total / n_total

        if val < best_so_far[]
            best_so_far[] = val
            if eval_count[] % 50 == 0 || eval_count[] == 1
                @printf("  [Eval %5d] m=%.2f σ=%.2fÅ ε=%.1f λr=%.1f εk_a=%.1f κ_a=%.2e MSE=%.4e\n",
                        eval_count[], m, σ*1e10, ε, λr, εk_assoc, κ_assoc, val)
            end
        end
        return val
    end
    return objetivo
end

bounds = BoxConstrainedSpace(
    lb = [log(1.5), log(3.2e-10), log(140.0), log(6.0),  log(1500.0), log(1e-32)],
    ub = [log(3.0), log(3.8e-10), log(250.0), log(12.0), log(3500.0), log(1e-28)]
)

resultados_optimos = Dict()
filas_tabla = DataFrame(Solvente = String[], T_K = Float64[], P_exp_Pa = Float64[], P_calc_Pa = Float64[], Err_pct = Float64[]

for comp in solventes
    println("\n" * "="^70)
    println("  INICIANDO AJUSTE: $comp")
    println("="^70)

    model_base = SAFTVRMie([comp], userlocations=[ruta1, ruta2])

    datos = datos_exp[comp]
    objetivo_comp = crear_objetivo(model_base, datos.T, datos.P)

    resultado = Metaheuristics.optimize(
        objetivo_comp, bounds,
        DE(N = 60, F = 0.8, CR = 0.9, strategy = :rand1,
           options = Options(iterations = 300, f_tol = 1e-8, verbose = false))
    )
```

Figure A.2. Julia code for fitting molecular parameters of ethanol (3) and 2-Propanol (4) from vapor pressure data from Ambrose & Sprake [130] (cont.).

```
    p_opt = exp.(resultado.best_sol.x)
    resultados_optimos[comp] = p_opt

    actualizar_parametros_puros!(model_base, p_opt...)

    println("\n  --- Resultados para $comp ---")
    @printf("  m        = %10.4f\n", p_opt[1])
    @printf("  σ        = %10.4e m\n", p_opt[2])
    @printf("  ε/k      = %10.4f K\n", p_opt[3])
    @printf("  λ_r      = %10.4f\n", p_opt[4])
    @printf("  ε_assoc  = %10.4f K\n", p_opt[5])
    @printf("  κ_assoc  = %10.4e m³\n", p_opt[6])

    println("\n  T [K]      P_exp [Pa]      P_calc [Pa]      % Error")
    println("  " * "-"^55)

    for (i, T) in enumerate(datos.T)
        P_calc = Clapeyron.saturation_pressure(model_base, T)[1]
        P_exp = datos.P[i]
        err = (P_calc - P_exp) / P_exp * 100

        @printf("  %6.2f    %10.1f     %10.1f       %+6.2f %%\n", T, P_exp, P_calc, err)
        push!(filas_tabla, (comp, T, P_exp, P_calc, round(err, digits=2)))
    end
end
CSV.write("resultados_presion_vapor.csv", filas_tabla)
println("\n  Tabla comparativa guardada → resultados_presion_vapor.csv")

plt = plot(xlabel = "T [K]", ylabel = "log10(P_sat [Pa])",
           title = "Ajuste de Presión de Vapor - SAFT-VR Mie",
           legend = :bottomright, grid = true, framestyle = :box)

colores = [:steelblue, :darkorange]

for (i, comp) in enumerate(solventes)
    datos = datos_exp[comp]
    p_opt = resultados_optimos[comp]

    model_base = SAFTVRMie([comp], userlocations=[ruta1, ruta2])
    actualizar_parametros_puros!(model_base, p_opt...)

    T_range = range(minimum(datos.T), maximum(datos.T), length=50)
    P_line = [log10(Clapeyron.saturation_pressure(model_base, t)[1]) for t in T_range]

    plot!(plt, T_range, P_line, label="Calc. - $comp", color=colores[i], linewidth=2)
    scatter!(plt, datos.T, log10.(datos.P), label="Exp. - $comp", color=colores[i], markershape=:circle, msw=0
end

display(plt)
savefig(plt, "ajuste_psat.png")
println("  Gráfico guardado → ajuste_psat.png")
```

Figure A.3. Julia code for fitting molecular parameters of ethanol (3) and 2-Propanol (4) from vapor pressure data from Ambrose & Sprake [130] (cont.).

Appendix B: Comparison of Experimental Data and SAFT-VR Mie Calculations.

Table B.1. Experimental vapor pressures of ethanol (3) and corresponding values calculated using the SAFT-VR Mie equation of state. The relative percentage error is also reported.

T / K	p^{exp} (a) / Pa	p^{calc} / Pa	$\delta(p_i)$ (b) / %
292.8	5726	5529.30	3.44%
296.8	7269	7121.11	2.03%
298.9	8205	8093.54	1.36%
301.3	9430	9366.23	0.68%
306.5	12566	12637.81	0.57%
309.8	14981	15160.09	1.20%
312.4	17200	17479.18	1.62%
316.4	21109	21550.45	2.09%
320.5	25914	26539.83	2.42%
324.2	31047	31834.66	2.54%
327.8	36760	37692.75	2.54%
332.0	44584	45650.38	2.39%
336.0	53267	54385.84	2.10%
339.7	62572	63653.77	1.73%
343.7	74032	74928.34	1.21%
348.1	88763	89218.95	0.51%
350.6	97821	97909.01	0.09%
351.1	100121	100096.37	0.02%
351.5	101518	101429.07	0.09%
351.6	102151	102029.60	0.12%
352.3	104983	104705.35	0.26%
355.5	118719	117697.31	0.86%
359.0	135519	133296.95	1.64%
362.8	155824	151957.81	2.48%
366.6	179321	173134.77	3.45%

(a)[130]
(b) $\delta(P_i) = \left(P_i^{calc} - P_i\right)/P_i$

Table B.2. Experimental vapor pressures of 2-Propanol (4) and corresponding values calculated using the SAFT-VR Mie equation of state. The relative percentage error is also reported.

T / K	p^{exp} [a] / Pa	p^{calc} / Pa	$\delta(p_i)$ [b] / %
325.5	26540	26323.75	0.81%
329.9	33044	32945.27	0.30%
333.9	40017	40026.90	0.02%
337.2	46612	46706.05	0.20%
340.2	53371	53535.21	0.31%
342.9	59931	60133.32	0.34%
345.3	66601	66815.56	0.32%
347.5	73286	73495.22	0.29%
349.6	79997	80162.26	0.21%
351.6	86822	86923.72	0.12%
353.3	93175	93195.23	0.02%
355.1	100079	99978.88	0.10%
356.1	104266	104084.61	0.17%
358.2	113416	113023.96	0.35%
359.7	120046	119479.26	0.47%
361.1	126573	125800.32	0.61%
362.4	133218	132213.52	0.75%

[a] [130]
[b] $\delta(P_i) = \left(P_i^{calc} - P_i\right)/P_i$

Table B.3. Experimental solubilities of biochanin A (2) in ethanol (3) and corresponding values calculated using the SAFT-VR Mie equation of state.

T / K	x_2 / mol/mol	x_2^{calc} / mol/mol	$\delta(x_2)$ [a] / %
308.15	0.00246	0.00234	4.95%
313.15	0.00287	0.00287	-0.04%
318.15	0.00336	0.00352	-4.59%
323.15	0.00403	0.00430	-6.85%
328.15	0.00545	0.00525	3.56%
333.15	0.00653	0.00641	1.95%

[a] $\delta(x_i) = \left(x_i^{calc} - x_i\right)/x_i$

Table B.4. Experimental solubilities of biochanin A (2) in 2-Propanol (4) and corresponding values calculated using the SAFT-VR Mie equation of state.

T / K	x_2 / mol/mol	x_2^{calc} / mol/mol	$\delta(x_2)$ [a] / %
308.15	0.00250	0.00222	11.23%
313.15	0.00265	0.00269	-1.80%
318.15	0.00308	0.00327	-5.95%
323.15	0.00375	0.00396	-5.67%
328.15	0.00501	0.00480	4.09%
333.15	0.00605	0.00582	3.68%

[a] $\delta(x_i) = \left(x_i^{calc} - x_i\right)/x_i$

Appendix C: Julia Code for fitting SAFT-VR Mie molecular parameters of biochanin A (2) from solid-liquid equilibrium data in ethanol (3) and 2-propanol (4).

```julia
using Clapeyron
using Metaheuristics
using CSV, DataFrames
using Plots
using Statistics: mean
using Printf

ruta1 = raw"C:\Users\villa\OneDrive\Escritorio\pure.csv"
ruta2 = raw"C:\Users\villa\OneDrive\Escritorio\assoc.csv"
ruta3 = raw"C:\Users\villa\OneDrive\Escritorio\unlike.csv"

solventes = ["ethanol", "2propanol"]

datos_exp = [
    (T = [308.15, 313.15, 318.15, 323.15, 328.15, 333.15],
     x = [0.0024595, 0.0028687, 0.0033626, 0.0040265, 0.0054484, 0.0065328]),
    (T = [308.15, 313.15, 318.15, 323.15, 328.15, 333.15],
     x = [0.0025008, 0.0026453, 0.0030822, 0.0037475, 0.0050069, 0.0060450])
]

const Tm     = 486.15   # K
const ΔHfus  = 44729.0  # J/mol
const R_gas  = 8.31446  # J/(mol·K)

println("Cargando modelos termodinámicos desde CSV...")
modelos        = [SAFTVRMie([s, "BCA4C"], userlocations=[ruta1, ruta2, ruta3]) for s in solventes]
model_BCA_pura = SAFTVRMie(["BCA4C"], userlocations=[ruta1, ruta2, ruta3])
println("   OK — Modelos cargados.")


function _actualizar_assoc!(model_mezcla, model_puro, εk_assoc, κ_assoc)
    ea_m = model_mezcla.params.epsilon_assoc
    bv_m = model_mezcla.params.bondvol
    n_m  = length(ea_m.values.values)

    εk_solv, κ_solv = 0.0, 0.0
    for k in 1:n_m
        if ea_m.values.outer_indices[k] == (1, 1)
            εk_solv = ea_m.values.values[k]
            κ_solv  = bv_m.values.values[k]
            break
        end
    end

    εk_cross = sqrt(εk_solv * εk_assoc)
    κ_cross  = ((κ_solv^(1/3) + κ_assoc^(1/3)) / 2)^3

    for k in 1:n_m
        ij = ea_m.values.outer_indices[k]
        if ij == (2, 2)
            ea_m.values.values[k] = εk_assoc
            bv_m.values.values[k] = κ_assoc
        elseif ij == (1, 2) || ij == (2, 1)
            ea_m.values.values[k] = εk_cross
            bv_m.values.values[k] = κ_cross
        end
    end
```

Figure C.1. Julia code for ethanol (3) and 2-Propanol (4) molecular parameters fit. Used Clapeyron.jl package.

```
    ea_p = model_puro.params.epsilon_assoc
    bv_p = model_puro.params.bondvol
    for k in 1:length(ea_p.values.values)
        if ea_p.values.outer_indices[k] == (1, 1)
            ea_p.values.values[k] = εk_assoc
            bv_p.values.values[k] = κ_assoc
        end
    end
end

function actualizar_todo!(model_mezcla, model_puro,
                          m_BCA, σ_BCA, ε_BCA, λr_BCA, εk_assoc, κ_assoc)
    # --- A. Parámetros puros BCA ---
    model_mezcla.params.segment.values[2]    = m_BCA
    model_mezcla.params.sigma.values[2,2]    = σ_BCA
    model_mezcla.params.epsilon.values[2,2]  = ε_BCA
    model_mezcla.params.lambda_r.values[2,2] = λr_BCA
    model_puro.params.segment.values[1]      = m_BCA
    model_puro.params.sigma.values[1,1]      = σ_BCA
    model_puro.params.epsilon.values[1,1]    = ε_BCA
    model_puro.params.lambda_r.values[1,1]   = λr_BCA

    # --- B. Parámetros cruzados de dispersión (kij = 0) ---
    σ11   = model_mezcla.params.sigma.values[1,1]
    lam11 = model_mezcla.params.lambda_r.values[1,1]
    eps11 = model_mezcla.params.epsilon.values[1,1]

    σ12       = (σ11 + σ_BCA) / 2.0
    lam12     = 3.0 + sqrt((lam11 - 3.0) * (λr_BCA - 3.0))
    ratio_vol = sqrt((σ11^3) * (σ_BCA^3)) / (σ12^3)
    eps12     = ratio_vol * sqrt(eps11 * ε_BCA)

    model_mezcla.params.sigma.values[1,2]    = σ12
    model_mezcla.params.sigma.values[2,1]    = σ12
    model_mezcla.params.lambda_r.values[1,2] = lam12
    model_mezcla.params.lambda_r.values[2,1] = lam12
    model_mezcla.params.epsilon.values[1,2]  = eps12
    model_mezcla.params.epsilon.values[2,1]  = eps12

    _actualizar_assoc!(model_mezcla, model_puro, εk_assoc, κ_assoc)
end

fugacidad_solido(T::Float64) = exp((ΔHfus / R_gas) * (1/Tm - 1/T))

function coef_actividad_robusto(model_mezcla, T::Float64, x_solid::Float64)
    x2 = clamp(x_solid, 1e-10, 1-1e-10)
    z  = [1.0 - x2, x2]
    P  = 101325.0
    γ = try
        Clapeyron.activity_coefficient(model_mezcla, P, T, z)
    catch
        return NaN
    end
    return γ[2]
end
```

Figure C.2. Julia code for ethanol (3) and 2-Propanol (4) molecular parameters fit. Used Clapeyron.jl package (cont.).

```
function equilibrio_x(model_mezcla, T::Float64; tol=1e-8, maxiter=300)
    f_ratio = fugacidad_solido(T)
    f_ratio >= 1.0 && return 1.0
    x = clamp(f_ratio, 1e-6, 1.0)
    for _ in 1:maxiter
        γ = coef_actividad_robusto(model_mezcla, T, x)
        (isnan(γ) || γ <= 0.0) && return NaN
        x_new = clamp(f_ratio / γ, 1e-10, 0.9999)
        abs(x_new - x) < tol && return x_new
        x = 0.8x + 0.2x_new
    end
    return NaN
end

println("\n" * "="^70)
println("   INICIANDO AJUSTE GLOBAL: 6 parámetros usando Etanol y 2-Propanol")
println("="^70)

eval_count_global  = Ref(0)
best_so_far_global = Ref(1e10)

function objetivo_global(params::Vector{Float64})
    any(isnan, params) || any(isinf, params) && return 1e10

    m_BCA    = exp(params[1])   # ← nuevo parámetro
    σ_BCA    = exp(params[2])
    ε_BCA    = exp(params[3])
    λr_BCA   = exp(params[4])
    εk_assoc = exp(params[5])
    κ_assoc  = exp(params[6])

    (m_BCA    <  3.0    || m_BCA    > 20.0)    && return 1e10
    (σ_BCA    < 2.5e-10 || σ_BCA    > 6.5e-10) && return 1e10
    (ε_BCA    < 50.0    || ε_BCA    > 600.0)   && return 1e10
    (λr_BCA   < 8.0     || λr_BCA   > 35.0)    && return 1e10
    (εk_assoc < 2000.0  || εk_assoc > 4000.0)  && return 1e10
    (κ_assoc  < 1e-33   || κ_assoc  > 1e-28)   && return 1e10

    eval_count_global[] += 1

    sse_total, n_total = 0.0, 0

    try
        for (model_solv, datos) in zip(modelos, datos_exp)
            actualizar_todo!(model_solv, model_BCA_pura,
                             m_BCA, σ_BCA, ε_BCA, λr_BCA, εk_assoc, κ_assoc)

            for (T, x_obs) in zip(datos.T, datos.x)
                x_c = equilibrio_x(model_solv, T)
                if isnan(x_c) || isinf(x_c) || x_c <= 0.0
                    return 1e10
                end
                sse_total += (log(x_c) - log(x_obs))^2
                n_total   += 1
```

Figure C.3. Julia code for ethanol (3) and 2-Propanol (4) molecular parameters fit. Used Clapeyron.jl package (cont.).

```
            end
        end
    catch
        return 1e10
    end

    val = sse_total / n_total
    if val < best_so_far_global[]
        best_so_far_global[] = val
        @printf("  [MEJOR %6d]  m=%.3f  σ=%.2fÅ  ε=%.1f  λr=%.1f  εk_a=%.1f  κ_a=%.2e  MSE=%.4e ★\n",
                eval_count_global[], m_BCA, σ_BCA*1e10, ε_BCA, λr_BCA, εk_assoc, κ_assoc, val)
    end
    return val
end

bounds_global = BoxConstrainedSpace(
    lb = [log(3.0),    log(1.5e-10), log(50.0), log(8.0), log(2000.0), log(1e-33)],
    ub = [log(20.0),   log(6.5e-10), log(600.0), log(35.0), log(4000.0), log(1e-29)]
)

result_global = Metaheuristics.optimize(
    objetivo_global, bounds_global,
    DE(
        N = 120, F = 0.8, CR = 0.9, strategy = :rand1,
        options = Options(
            iterations    = 200,
            f_calls_limit = 250_000,
            f_tol         = 1e-8,
            x_tol         = 1e-8,
            verbose       = true,
        )
    )
)

p_opt    = result_global.best_sol.x
m_opt    = exp(p_opt[1])
σ_opt    = exp(p_opt[2])
ε_opt    = exp(p_opt[3])
λr_opt   = exp(p_opt[4])
εk_opt   = exp(p_opt[5])
κ_opt    = exp(p_opt[6])

# ============================================================
# REPORTE FINAL DE PARÁMETROS
# ============================================================
println("\n" * "="^65)
println("  PARÁMETROS FINALES — BCA (Ajuste Global Simúltaneo)")
println("="^65)
@printf("  m          = %10.4f\n",          m_opt)
@printf("  σ          = %10.4e  m\n",       σ_opt)
@printf("  ε/k        = %10.4f  K\n",       ε_opt)
@printf("  λ_r        = %10.4f\n",          λr_opt)
@printf("  ε_assoc/k  = %10.4f  K\n",       εk_opt)
@printf("  κ_assoc    = %10.4e  m³\n",      κ_opt)
@printf("\n  MSE Global log   = %.6e\n",  result_global.best_sol.f)

# ============================================================
# VALIDACIÓN — TABLA COMPARATIVA Y EXPORTACIÓN A CSV
# ============================================================
println()

for model in modelos
    actualizar_todo!(model, model_BCA_pura, m_opt, σ_opt, ε_opt, λr_opt, εk_opt, κ_opt)
end

aad_por_solv = Float64[]
```

Figure C.4. Julia code for ethanol (3) and 2-Propanol (4) molecular parameters fit. Used Clapeyron.jl package (cont.).

```
filas_tabla = DataFrame(
    Solvente = String[],
    T_K      = Float64[],
    x_exp    = Float64[],
    x_calc   = Float64[],
    err_pct  = Float64[]
)

for (i, (solv, model, datos)) in enumerate(zip(solventes, modelos, datos_exp))
    x_calc = [equilibrio_x(model, T) for T in datos.T]
    aad_s  = mean(abs.((x_calc .- datos.x) ./ datos.x)) * 100
    push!(aad_por_solv, aad_s)

    println("  ┌─ $solv  (AAD = $(@sprintf("%.2f", aad_s)) %)")
    println("  │  T [K]      x_exp          x_calc         %err")
    println("  │  ──────────────────────────────────────────────────")
    for j in eachindex(datos.T)
        err = (x_calc[j] - datos.x[j]) / datos.x[j] * 100
        @printf("  │  %6.2f   %.7f      %.7f      %+6.2f%%\n",
                datos.T[j], datos.x[j], x_calc[j], err)
        push!(filas_tabla, (solv, datos.T[j], datos.x[j], x_calc[j], round(err, digits=2)))
    end
    println("  └──────────────────────────────────────────────────")
end

@printf("\n  AAD Global = %.2f %%\n", mean(aad_por_solv))

@printf("\n  AAD Global = %.2f %%\n", mean(aad_por_solv))

nombre_archivo_csv = "BCA_params_fit_4C_Gamma.csv"
try
    CSV.write(nombre_archivo_csv, filas_tabla)
    println("\n  ★ Tabla comparativa guardada exitosamente en → ", abspath(nombre_archivo_csv))
catch e
    println("\n  ❌ Error al intentar escribir el archivo CSV: ", e)
end

# ============================================================
# GRÁFICO Y EXPORTACIÓN DE CURVAS DENSAS PARA PYTHON
# ============================================================
colores   = [:steelblue, :darkorange]
formas    = [:circle, :square]
etiquetas = ["Etanol", "2-Propanol"]

plt = plot(
    xlabel     = "T  [K]",
    ylabel     = "x_BCA  (fracción molar)",
    title      = "SLE – BCA Ajuste Parametros Simultáneo",
    legend     = :topleft,
    framestyle = :box,
    grid       = true,
    size       = (800, 550),
)

df_curvas = DataFrame(Solvente = String[], T_K = Float64[], x_calc = Float64[])

T_range = range(298.0, 338.0, length=120)

for (i, (solv, model, datos)) in enumerate(zip(solventes, modelos, datos_exp))
    x_line = [equilibrio_x(model, T) for T in T_range]

    for (T_val, x_val) in zip(T_range, x_line)
        push!(df_curvas, (solv, T_val, x_val))
    end

    plot!(plt,    T_range, x_line;  label="$(etiquetas[i]) – modelo",
          linewidth=2, color=colores[i])
    scatter!(plt, datos.T, datos.x; label="$(etiquetas[i]) – exp.",
             color=colores[i], markershape=formas[i], markersize=6, msw=0)
end

display(plt)
savefig(plt, "SLE_Fit_4C_Gamma.png")
println("  Gráfico de control guardado → SLE_Fit_4C_Gamma.png")

nombre_curvas_csv = "BCA_fit_curvas_4C_Gamma.csv"
try
    CSV.write(nombre_curvas_csv, df_curvas)
    println("\n  ★ Curvas del modelo guardadas para Python en → ", abspath(nombre_curvas_csv))
catch e
    println("\n  ❌ Error al intentar escribir el archivo de curvas: ", e)
end
```

Figure C.5. Julia code for ethanol (3) and 2-Propanol (4) molecular parameters fit. Used Clapeyron.jl package (cont.).

Appendix D: Julia Code for CO_2 (1) + biochanin A (2) binary interaction parameter function fit.

```julia
#4C SCHEME APPROACH - NEW PARAMETERS
using Clapeyron
using Metaheuristics
using CSV, DataFrames
using Plots
using Statistics: mean
using Printf
using Logging

disable_logging(Logging.Warn)

ruta1 = raw"C:\Users\villa\OneDrive\Escritorio\pure.csv"
ruta2 = raw"C:\Users\villa\OneDrive\Escritorio\assoc.csv"
ruta3 = raw"C:\Users\villa\OneDrive\Escritorio\unlike.csv"

# Datos Biochanin-A
const Tb2  = 698.46   # K
const Tc2  = 925.33   # K
const Pc2  = 1.963    # MPa
const vc2  = 835.6    # cm³/mol
const R    = 8.314    # J/(mol·K)

const v2sub_m3 = 0.0002002   # m³/mol

# Datos experimentales
data_exp = [
    (T      = 313.15, # K
     p2sub  = 2.3425e-6,   # Pa
     y2     = [3.604e-6, 3.775e-6, 4.099e-6, 3.172e-6, 3.017e-6, 2.597e-6], # mol/mol
     P      = [14.781e6, 18.054e6, 22.426e6, 26.069e6, 27.601e6, 31.417e6]), # Pa

    (T      = 323.15, # K
     p2sub  = 8.6678e-6,   # Pa
     y2     = [1.691e-6, 5.756e-6, 4.985e-6, 4.975e-6, 4.306e-6, 4.023e-6], # mol/mol
     P      = [10.202e6, 14.876e6, 17.846e6, 18.323e6, 22.553e6, 24.892e6]), # Pa

    (T      = 333.15, # K
     p2sub  = 4.0346e-5,   #Pa
     y2     = [6.643e-6, 5.335e-6, 4.000e-6, 3.628e-6], # mol/mol
     P      = [18.719e6, 23.062e6, 27.345e6, 29.884e6])  # Pa
]

model = SAFTVRMie(["CO2","BCA"], userlocations=[ruta1, ruta2, ruta3])

# Parámetros puros (sólo lectura)
eps11   = model.params.epsilon.values[1,1]
eps22   = model.params.epsilon.values[2,2]
sigma11 = model.params.sigma.values[1,1]
sigma22 = model.params.sigma.values[2,2]
sigma12 = model.params.sigma.values[1,2]

global iter_count = 0
```

Figure D.1. Julia code for CO_2 (1) + Biochanin A (2) binary interaction parameter (k_{12}) function parameter fit. Used Clapeyron.jl package.

```
function calcular_y2(model, P, T, psub, y2_init=1e-6; tol=1e-10, maxiter=1000)
    poynting_0 = exp((v2sub_m3 / (R * T)) * (P - psub))
    y2 = (psub * poynting_0) / P

    for iter in 1:maxiter
        y2 = clamp(y2, 1e-20, 1.0)
        z  = [1.0 - y2, y2]

        phi_sist = fugacity_coefficient(model, P, T, z)
        phi2     = phi_sist[2]

        if phi2 <= 0.0 || isnan(phi2) || isinf(phi2)
            return NaN
        end

        poynting = exp((v2sub_m3 / (R * T)) * (P - psub))
        y2_new   = (psub * poynting) / (P * phi2)

        if abs(y2_new - y2) / max(abs(y2), 1e-20) < tol
            return y2_new
        end

        alpha = iter < 20 ? 0.5 : 0.8
        y2 = alpha * y2_new + (1 - alpha) * y2
    end
    return NaN
end

function obj_kij(params)
    global iter_count
    A, B = params

    total_error  = 0.0
    total_points = 0
    first_calc   = Ref(0.0)
    rmse_log     = 0.0

    try
        for isotherm in data_exp
            T   = isotherm.T
            kij = A + B*(1/T - 1/313.15)

            if kij >= 1.0
                return 1e10
            end

            eps12_new = (1.0 - kij) * (sqrt(sigma11^3 * sigma22^3) / sigma12^3) * sqrt(eps11 * eps22)

            model.params.epsilon.values[1,2] = eps12_new
            model.params.epsilon.values[2,1] = eps12_new
            Clapeyron.recombine!(model)

            psub = isotherm.p2sub

            for i in eachindex(isotherm.P)
                P      = isotherm.P[i]
                y2_exp = isotherm.y2[i]

                y2_calc = calcular_y2(model, P, T, psub, 1e-6)
```

Figure D.2. Julia code for CO_2 (1) + biochanin A (2) binary interaction parameter (k_{12}) function parameter fit. Used Clapeyron.jl package (cont.).

```
                if isnan(y2_calc) || y2_calc <= 0.0
                    return 1e10
                end

                if total_points == 0
                    first_calc[] = y2_calc
                end

                total_error  += (log10(y2_exp) - log10(y2_calc))^2
                total_points += 1
            end
        end

        rmse_log = sqrt(total_error / total_points)

    catch e
        return 1e10
    end

    iter_count += 1

    if iter_count % 100 == 0 || iter_count == 1
        @printf("Eval %4d | A=%8.5f B=%9.5f | RMSE_log=%7.4f | y2_calc=%.3e vs %.3e\n",
                iter_count, A, B, rmse_log, first_calc[], data_exp[1].y2[1])
    end

    return rmse_log
end

println("\nIniciando optimización global con Differential Evolution (DE)...")
iter_count = 0

bounds = [-1.0   -300.0;
           1.5    1000.0]

options = Options(f_calls_limit=4000, f_tol=1e-4)
algorithm = DE(N=100, options=options)

res_meta = Metaheuristics.optimize(obj_kij, bounds, algorithm)

disable_logging(Logging.Debug)

A_opt, B_opt = Metaheuristics.minimizer(res_meta)
min_rmse     = Metaheuristics.minimum(res_meta)

println("\n╔═══════════════ AJUSTE FINAL ═══════════════╗")
@printf("║  A  (kij a 313.15 K)  = %10.6f        ║\n", A_opt)
@printf("║  B  (pendiente en T)  = %10.6f  K     ║\n", B_opt)
@printf("║  kij(313.15) = %.6f                ║\n", A_opt)
@printf("║  kij(323.15) = %.6f                ║\n", A_opt + B_opt*(1/323.15-1/313.15))
@printf("║  kij(333.15) = %.6f                ║\n", A_opt + B_opt*(1/333.15-1/313.15))
@printf("║  RMSE Log mínimo  = %.4f                ║\n", min_rmse)
println("╚═══════════════════════════════════════════╝")

println("\n" * "="^70)
println("  TABLA COMPARATIVA: MODELO VS EXPERIMENTAL (Solubilidad y2)")
println("="^70)

results_df = DataFrame(T_K=Float64[], P_MPa=Float64[], y2_exp=Float64[], y2_calc=Float64[], Error_Pct=Float64[])
```

Figure D.3. Julia code for CO_2 (1) + biochanin A (2) binary interaction parameter (k_{12}) function parameter fit. Used Clapeyron.jl package (cont.).

Appendix E: Julia Code for CO_2 (1)+ biochanin A (2) thermodynamic consistency test.

```julia
using Clapeyron
using Optim
using CSV, DataFrames
using Plots
using Statistics: mean
using Printf

ruta1 = raw"C:\Users\villa\OneDrive\Escritorio\pure.csv"
ruta2 = raw"C:\Users\villa\OneDrive\Escritorio\assoc.csv"
ruta3 = raw"C:\Users\villa\OneDrive\Escritorio\unlike.csv"

const v2sub_m3 = 0.0002002
const R = 8.314 # J/(mol K)

function calcular_y2(model, P, T, psub, y2_init; tol=1e-8, maxiter=200)
    y2 = y2_init
    for _ in 1:maxiter
        y2 = clamp(y2, 1e-9, 1e-2)
        z  = [1.0 - y2, y2]

        phi_sist = fugacity_coefficient(model, P, T, z)
        phi2     = phi_sist[2]
        poynting = exp((v2sub_m3 / (R * T)) * (P - psub))
        y2_new   = (psub * poynting) / (P * phi2)

        if abs(y2_new - y2) / max(abs(y2), 1e-20) < tol
            return y2_new
        end

        y2 = 0.3 * y2_new + 0.7 * y2
    end
    return y2
end

function actualizar_parametros!(model, T, A, B)
    kij = A + B * (1/T - 1/313.15)

    eps11 = model.params.epsilon.values[1, 1]
    eps22 = model.params.epsilon.values[2, 2]

    eps12 = (1.0 - kij) * sqrt(eps11 * eps22)

    model.params.epsilon.values[1, 2] = eps12
    model.params.epsilon.values[2, 1] = eps12

    Clapeyron.recombine!(model)

    return model
end

function propiedades_estado(model, P, T, yi)
    z_mole = [1.0 - yi, yi]

    v = volume(model, P, T, z_mole)
    z = compressibility_factor(model, P, T, z_mole)

    phi = fugacity_coefficient(model, P, T, z_mole, vol0=v)

    return z, phi[1], phi[2]
end
```

Figure E.1. Julia code for CO_2 (1) + biochanin A (2) system thermodynamic consistency test. Used Clapeyron.jl package.

```
function calcular_areas(idx0, idxf, P, y, z, phi1, phii)
    p0, pf = P[idx0], P[idxf]
    yi0, yif = y[idx0], y[idxf]
    z0, zf   = z[idx0], z[idxf]
    phi10, phi1f = phi1[idx0], phi1[idxf]
    phii0, phiif = phii[idx0], phii[idxf]

    Ap = (1.0 / (yif * pf) + 1.0 / (yi0 * p0)) * (pf - p0) / 2.0

    den_f = abs(zf - 1.0) < 1e-6 ? sign(zf - 1.0)*1e-6 : (zf - 1.0)
    den_0 = abs(z0 - 1.0) < 1e-6 ? sign(z0 - 1.0)*1e-6 : (z0 - 1.0)
    term_phi1 = (1.0 - yif) / (yif * den_f * phi1f) +
                (1.0 - yi0) / (yi0 * den_0 * phi10)
    delta_phi1 = (phi1f - phi10) / 2.0
    term_phii = 1.0 / (den_f * phiif) +
                1.0 / (den_0 * phii0)
    delta_phii = (phiif - phii0) / 2.0
    Aphi = (term_phi1 * delta_phi1) + (term_phii * delta_phii)
    return Ap, Aphi
end

function test_consistencia(model, T, P_exp, y_exp, A_param, B_param)
    actualizar_parametros!(model, T, A_param, B_param)
    N = length(P_exp)
    z_arr = Vector{Float64}(undef, N)
    phi1_arr = Vector{Float64}(undef, N)
    phii_arr = Vector{Float64}(undef, N)
    for j in 1:N
        z_arr[j], phi1_arr[j], phii_arr[j] = propiedades_estado(model, P_exp[j], T, y_exp[j])
    end
    DeltaA = Vector{Float64}(undef, N)

    for j in 1:N


        if j == 1
            Ap, Aphi = calcular_areas(1, 2, P_exp, y_exp, z_arr, phi1_arr, phii_arr)
            DeltaA[j] = abs((Ap - Aphi) / Ap)

        elseif j == N
            Ap, Aphi = calcular_areas(N-1, N, P_exp, y_exp, z_arr, phi1_arr, phii_arr)
            DeltaA[j] = abs((Ap - Aphi) / Ap)

        else
            Ap1, Aphi1 = calcular_areas(j-1, j, P_exp, y_exp, z_arr, phi1_arr, phii_arr)
            val1 = (Ap1 - Aphi1) / Ap1

            Ap2, Aphi2 = calcular_areas(j-1, j+1, P_exp, y_exp, z_arr, phi1_arr, phii_arr)
            val2 = (Ap2 - Aphi2) / Ap2

            Ap3, Aphi3 = calcular_areas(j, j+1, P_exp, y_exp, z_arr, phi1_arr, phii_arr)
            val3 = (Ap3 - Aphi3) / Ap3

            DeltaA[j] = (1.0 / 3.0) * abs(val1 + val2 + val3)
        end
    end

    es_consistente = DeltaA .<= 0.20

    return DeltaA, es_consistente
end
```

Figure E.2. Julia code for CO_2 (1) + biochanin A (2) system thermodynamic consistency test. Used Clapeyron.jl package (cont.).

```
model = SAFTVRMie(["CO2","BCA"], userlocations=[ruta1, ruta2, ruta3])

A_param = -0.136058
B_param = 96.670538

data_exp = [
    (T      = 313.15,
     p2sub  = 2.3425e-6,
     y2     = [3.604e-6, 3.775e-6, 4.099e-6, 3.172e-6, 3.017e-6, 2.597e-6],
     P      = [14.781e6, 18.054e6, 22.426e6, 26.069e6, 27.601e6, 31.417e6]),

    (T      = 323.15,
     p2sub  = 8.6678e-6,
     y2     = [1.691e-6, 5.756e-6, 4.985e-6, 4.975e-6, 4.306e-6, 4.023e-6],
     P      = [10.202e6, 14.876e6, 17.846e6, 18.323e6, 22.553e6, 24.892e6]),

    (T      = 333.15,
     p2sub  = 4.0346e-5,
     y2     = [0.430e-6, 7.893e-6, 6.643e-6, 5.335e-6, 4.000e-6, 3.628e-6],
     P      = [10.922e6, 13.702e6, 18.719e6, 23.062e6, 27.345e6, 29.884e6])
]

println("="^95)
println(" RESULTADOS: SOLUBILIDAD Y CONSISTENCIA TERMODINÁMICA")
println("="^95)

df_consistencia = DataFrame(
    T_K = Float64[],
    P_MPa = Float64[],
    y2_exp = Float64[],
    y2_calc = Float64[],
    Error_Pct = Float64[],
    DeltaA = Float64[],
    Consistente = String[]
)

for isoterma in data_exp
    T_actual = isoterma.T
    P_actual = isoterma.P
    y_actual = isoterma.y2
    psub_actual = isoterma.p2sub

    desviaciones, consistencia = test_consistencia(model, T_actual, P_actual, y_actual, A_param, B_param)

    actualizar_parametros!(model, T_actual, A_param, B_param)

    @printf("\n► Isoterma: %.2f K\n", T_actual)
    println("-"^95)
    @printf("%9s | %11s | %11s | %11s | %12s | %15s\n",
            "P [MPa]", "y2_exp", "y2_calc", "δ(yi) [%]", "|ΔA1i|", "¿Consistente?")
    println("-"^95)

    for i in 1:length(P_actual)
        y2_calc = NaN
        try
            y2_calc = calcular_y2(model, P_actual[i], T_actual, psub_actual, 1e-6)
        catch
            y2_calc = NaN
        end

        delta_y = isnan(y2_calc) ? NaN : ((y2_calc - y_actual[i]) / y_actual[i]) * 100.0
        estado = consistencia[i] ? "SÍ (<=20%)" : "NO (>20%)"

        @printf("%9.4f | %11.4e | %11.4e | %+10.2f%% | %12.4f | %15s\n",
                P_actual[i]/1e6, y_actual[i], y2_calc, delta_y, desviaciones[i], estado)

        push!(df_consistencia, (T_actual, P_actual[i]/1e6, y_actual[i], y2_calc, delta_y, desviaciones[i], estado))
    end
end
println("\n" * "="^95)

CSV.write("test_consistencia_todos.csv", df_consistencia)
println("✓ Tabla de consistencia guardada en 'test_consistencia_todos.csv'")
```

Figure E.3. Julia code for CO_2 (1) + biochanin A (2) system thermodynamic consistency test. Used Clapeyron.jl package (cont.).